Karlsruhe Institute of Technology

Tritium Laboratory Karlsruhe

Conceptual Design Study of a Time-of-Flight System for Temperature Determination of an Atomic Tritium Beam

Master's Thesis of

Sebastian Koch

at the Department of Physics
Institute for Astroparticle Physics
Tritium Laboratory Karlsruhe

Reviewer:	Prof. Dr. Kathrin Valerius
Second reviewer:	Prof. Dr. Ralph Engel
Advisors:	Dr. Robin Größle
	Dr. Marco Röllig

1 February 2023 – 31 January 2024

Ich versichere wahrheitsgemäß, die Arbeit selbstständig verfasst, alle benutzten Hilfsmittel vollständig und genau angegeben und alles kenntlich gemacht zu haben, was aus Arbeiten anderer unverändert oder mit Abänderungen entnommen wurde sowie die Satzung des KIT zur Sicherung guter wissenschaftlicher Praxis in der jeweils gültigen Fassung beachtet zu haben.

Karlsruhe, 31 January 2024

.....
(Sebastian Koch)

Accepted as examination copy

Karlsruhe, 31 January 2024

.....
(Prof. Dr. Kathrin Valerius)

Contents

List of Figures

1. Introduction

The neutrino was postulated by Pauli in 1930 as a “desperate remedy” to explain the continuous β-spectrum [Pau30]. He assumed its mass to be of the same order as that of an electron. In 1956, neutrinos have been detected [Cow+56]. It has long been assumed that neutrino mass is zero [Lan57]. Today, their mass is known to be at least five orders of magnitude lighter than any other fermion of the standard model [Ake+22]. Neutrino mass might therefore be created by a different mechanism as those of the other standard model particles [Pet13]. Evidence that neutrinos have a mass above zero was provided by the observation of neutrino oscillations [Sup+98; SNO+02].

Neutrino oscillations tell only about differences of the squares of neutrino mass eigenvalues. They only give a lower limit and there are two different ways of ordering mass eigenstates. Therefore, there are two possible realisations in nature: The mass of an electron neutrino is greater than $48\,\mathrm{meV/c^2}$ (95 % confidence level (CL)) in case of inverted ordering or greater than $8.5\,\mathrm{meV/c^2}$ (95 % CL) in case of normal ordering [Par+22].

Cosmological observations limit the sum of neutrino masses to below $120\,\mathrm{meV/c^2}$ (95 % CL) [Ala+21]. This follows from modelling the cosmic microwave background and from surveys of cosmic large-scale structures. This result therefore depends on the applied cosmological models [DP18]. Experiments searching for neutrinoless double-β decays require the existence of Majorana neutrinos to make statements about neutrino mass. Measurements at ^{136}Xe limit the effective Majorana neutrino mass to below $165\,\mathrm{meV/c^2}$ (90 % CL) [Kam+16].

The most direct way to determine the neutrino mass is from the single-β decay. This is model-independent as it requires none of the assumptions mentioned before. The currently best result using this method limits neutrino mass to below $800\,\mathrm{meV/c^2}$ (90 % CL) [Ake+22]. This result was achieved by the Karlsruhe Tritium Neutrino (KATRIN) experiment which aims to improve the upper limit to $200\,\mathrm{meV/c^2}$ (90 % CL) [AAB05]. Determining the neutrino mass by such an experiment would serve as an input for the models mentioned before, allowing to draw conclusions on cosmic structures, the mass nature of the neutrino and the origin of particle masses.

Decaying tritium produces β-electrons. The KATRIN experiment measures their spectrum near the endpoint which is distorted depending on neutrino mass. According to the predictions from neutrino oscillations, KATRIN’s sensitivity is likely not sufficient for measuring the neutrino mass. Therefore, an upgrade of the experiment will be needed. A limiting factor is the systematic uncertainty related to molecular excitations that comes with the currently used molecular tritium source. An atomic tritium source would avoid these uncertainties. It produces an atomic beam which is shaped and guided through the system to avoid recombination into molecules. For a sufficiently strong beam, it needs to be cooled to mK-temperatures. A crucial requirement

for the design of an effective beam cooling system is the development of a beam temperature analytics system.

A viable technique to measure beam temperature are time-of-flight (ToF) measurements. In this work, it is investigated how ToF is applied to atomic hydrogen and how the geometry of a ToF system is designed to achieve best accuracy. To this end, the propagation of particles in a temperature measurement system is calculated, ToF data is generated and beam temperature is extracted. This is supported by conducting and analysing simulations.

In chapter 2 of this work, the current state of the KATRIN experiment and its potential upgrade to an atomic tritium source are described. Chapter 3 tells about properties of particles in vacuum systems, software used to simulate them and about the subsystems that make up a temperature measurement system. These subsystems are investigated in detail in chapter 4. The shape of an atomic beam is described following its path through the system, from generation in a hot capillary (section 4.1) and shaping in a skimmer setup (section 4.2) to its measurement in a ToF setup (section 4.3). A ToF distribution of the beam is extracted, resembling measurement data of the simulated setup. In chapter 5, the beam temperature is determined from this ToF distribution (section 5.1). The accuracy of this procedure is estimated in dependence of system geometry (section 5.2).

2. Upgrade of KATRIN for operation with atomic tritium

KATRIN is currently the most accurate experiment for direct neutrino mass measurement, its aim is to reach a sensitivity of $0.2\,\mathrm{eV/c^2}$ (90 % CL) [AAB05]. This will likely not be sufficient to measure neutrino mass [Col+22]. A physical limitation in the current setup is the uncertainty due to the rotational-vibrational excitation of tritium molecules, described by the so-called final-state distribution (FSD). A cold atomic tritium source would avoid the contribution from molecular FSD and result in a simple atomic, almost monoenergetic, distribution. Such an upgrade of KATRIN requires an atomic beam source and an efficient cooling system with high throughput but minimal losses and minimal molecular background. For the construction of the beam cooling system, suitable diagnostics of beam temperature is essential. Thus, a temperature measurement system is investigated in this work.

2.1. The Karlsruhe Tritium Neutrino (KATRIN) experiment

The single-β decay of tritium T, or ^{3}H, is shown in Reaction 2.1, with an electron-anti-neutrino $\bar{\nu}_e$ and a surplus energy $Q \approx 18.6\,\mathrm{keV}$. Here, the decay of T_2 is considered. The released energy $Q(T_2)$ is distributed between recoil energy of the daughter nucleus ^{3}HeT, kinetic energy of the electron and total energy of the neutrino. The shape of the β-spectrum, shown in Figure 2.1a, stems from the electron receiving different shares of the released energy Q. For electron energy E near zero, the neutrino, which is not detected, receives almost all of the released energy. Recoil energy is small in comparison, its maximum is $1.72\,\mathrm{eV}$ for T_2 at the endpoint, which is the high energy end of the β-spectrum. There, the electron receives almost all of the released energy Q and the neutrino the lowest amount possible. This is, no kinetic energy but only the energy $m_\nu c^2$ required for creation of the neutrino. So this is how neutrino mass shows in the β-spectrum: Maximum observed energy of the electron, which is the position of the endpoint, and the shape of the β-spectrum near the endpoint depend on neutrino mass. Figure 2.1b demonstrates the effect on the β-spectra for two different hypothetical neutrino masses m_ν. [Kle+19]

$$\begin{aligned} \mathrm{T} &\longrightarrow {}^3\mathrm{He}^+ + \mathrm{e}^- + \bar{\nu}_\mathrm{e} + Q(\mathrm{T}) \\ \mathrm{T_2} &\longrightarrow {}^3\mathrm{HeT}^+ + \mathrm{e}^- + \bar{\nu}_\mathrm{e} + Q(\mathrm{T_2}) \qquad \text{from [Kle+19]} \end{aligned} \tag{2.1}$$

Initially, there are several isotopes that could potentially be used as β-emitters. For the KATRIN experiment, tritium was chosen. A major requirement is to produce a sufficient number of

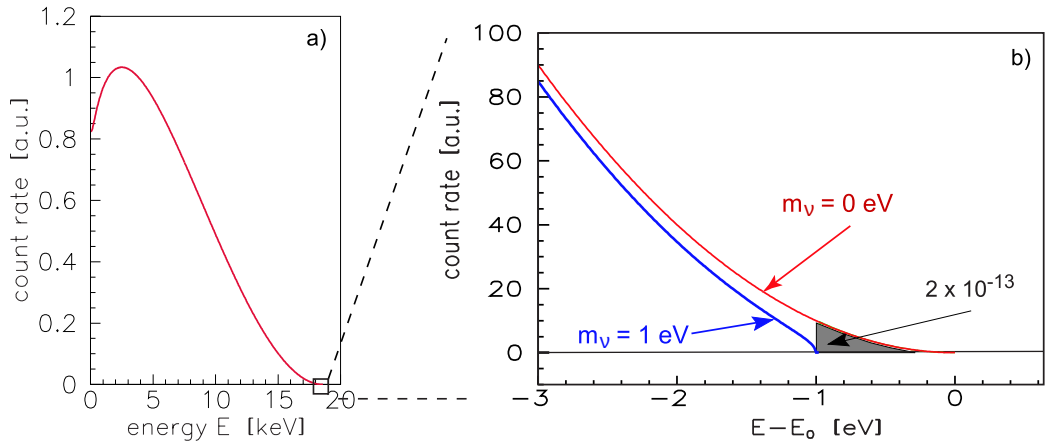

Figure 2.1.: **Tritium β-spectrum** The number of emitted electrons is plotted over their energy for the β-decay of tritium. In the left, the complete spectrum is shown. In the right, a narrow region near endpoint E_0 is shown for hypothetical neutrino masses of 0 and 1 eV. From all β-electrons, a share of about $2 \cdot 10^{-13}$ has an energy within 1 eV of the endpoint. Figure from [AAB05].

electrons with energy near the endpoint of the β-spectrum. The number of decays in a fixed range changes with $\sim 1/E_0^3$ and tritium has the second lowest endpoint energy E_0 of all β-unstable isotopes, with $E_0 \approx 18.6\,\mathrm{keV}$ [AAB05]. Also, its half-life of about $12.3\,\mathrm{a}$ is relatively low which results in high activity. Eventually, tritium produces the highest number of decays in the last eV of the β-spectrum when comparing same masses of different isotopes in the source [FGR21]. Moreover, the structures of T_2 and the resulting daughter molecule ^{3}HeT are simpler as those of much heavier molecules which allows quantitative calculation of the FSD [OW08], see details in section 2.2.

An overview of the KATRIN experimental setup is shown in Figure 2.2. Rear system and monitor spectrometer are used for calibration and monitoring but are not part of the main measurement process. A short description of the other subsystems is given here, following the downstream propagation of β-electrons. For a detailed description of the setup see [col+21].

The source system consists of a tube of $10\,\mathrm{m}$ in length and $9\,\mathrm{cm}$ in diameter. It is continuously filled with molecular tritium gas from the middle. The gas diffuses to both ends where it is pumped. Temperature is kept below $100\,\mathrm{K}$ to reduce conductance of the tube and increase gas density. Regarding infrastructure, the whole tritium cycle is closed so the tritium is purified and used again and again. Inside the source, the tritium decays and produces up to 10^{11} β-electrons$/s$. They are transported towards the spectrometers by magnetic fields without changing electron energy. Additionally, the transport system reduces tritium flow to less than 10^{-12} in order to prevent tritium from contaminating the spectrometer system. This subsystem consists of two large spectrometers. A retarding potential is applied to them, which is slightly smaller than the voltage corresponding to the endpoint E_0 of the β-spectrum. This way, all β-electrons are rejected except those close to the endpoint. The exact value of the retarding potential is adjusted stepwise to vary the minimal kinetic electron energy required to pass. Passing β-electrons are counted by the detector system. This way, an integral β-spectrum is measured. [col+21]

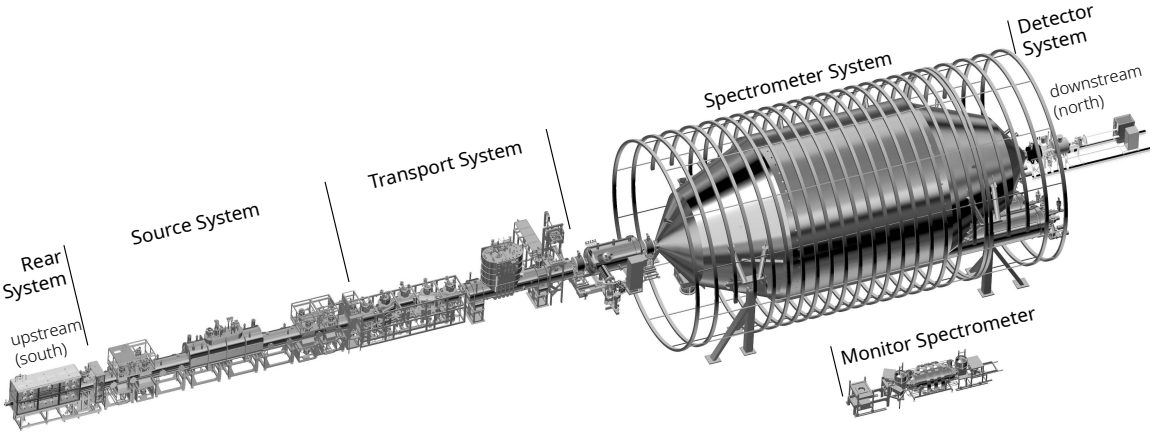

Figure 2.2.: **Experimental setup of KATRIN** β-electrons are generated in the source system and propagate downstream. Figure from [col+21].

2.2. Atomic tritium beam for electron production in KATRIN

Measurements of neutrino oscillations yield two possibilities of ordering the masses of the three neutrino mass eigenstates ν_1, ν_2 and ν_3, called normal and inverted ordering. In case of normal ordering, the masses are ordered like $m_1 < m_2 < m_3$, this results in a minimum electron neutrino mass of $8.5\,\mathrm{meV/c^2}$ (95 % CL). Inverted ordering assumes $m_3 < m_1 < m_2$, minimum electron neutrino mass is $48\,\mathrm{meV/c^2}$ (95 % CL) [DP18; Par+22]. Thus, a guaranteed neutrino mass detection requires sensitivity on the same scale as normal ordering. This sensitivity is not achievable with the current setup of KATRIN. If the detector system was upgraded for differential measurement, sensitivity was limited by the uncertainty introduced by using a source of molecular tritium T_2, see details in the master's thesis of Svenja Heyns [1].

When T_2 decays, the nuclear recoil excites the daughter molecule ^{3}HeT. All rotational, vibrational and electronic states are excited with a specific probability and excitation energy, this is described by the final-state distribution (FSD). For each state, the endpoint E_0 is reduced by the respective excitation energy. As all excitation energies are slightly different, electronic states are surrounded by rotational-vibrational excitations and, thus, effectively broadened. The ro-vibrational excitations of the electronic ground state are a small variance of the full FSD and only this needs to be determined theoretically. Still, it needs to be known to a precision of $2\,\%$ to achieve KATRIN's goal of a sensitivity of neutrino mass of $0.2\,\mathrm{eV/c^2}$. [FGR21]

A way to overcome this limitation is to replace the current molecular tritium source by an atomic tritium source. This prevents rotational and vibrational excitations as they require a binding between at least two atoms. Therefore, the FSD is not ro-vibrationally broadened and described by analytical functions [FGR21]. Doppler broadening is small at the aimed mK-beam temperature. β-electrons in excited states are not observed in the spectrum near the endpoint, this reduces statistics to the atoms in the ground state, those are about $70\,\%$ [FGR21]. Eventually, uncertainty

[1] Svenja Marie Heyns. "Neutrino Mass Sensitivity Studies Towards Potential Enhancements of the KATRIN Experiment with a High-Resolution Detector and an Atomic Tritium Source". Master's thesis. Karlsruhe: KIT, July 31, 2023.

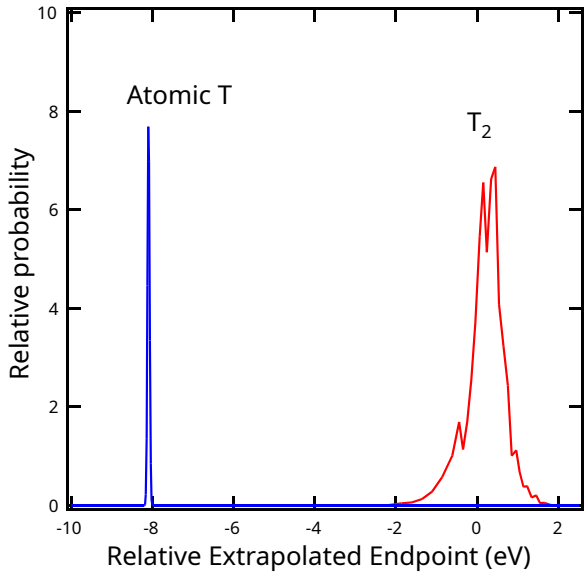

Figure 2.3.: **Final-state distributions of atomic and molecular tritium** Only ground states are shown here, the first electronically excited state of atomic tritium is at $-49\,\mathrm{eV}$. Doppler broadening of the atomic tritium line assumes a temperature of $1\,\mathrm{K}$. Figure from [FGR21].

introduced by an atomic tritium source is small enough to meet the demands of a guaranteed neutrino mass detection. The benefit of atomic tritium is already significant at the level of inverted ordering, at $48\,\mathrm{meV/c^2}$. Reduction of the width of the FSD is visualised in Figure 2.3.

Total energy given to nuclear motion is on average the same for atomic and molecular tritium. This is due to a balancing of two effects: Atomic tritium receives double the recoil energy as a molecule but the average endpoint of the molecular tritium β-spectrum is lowered by an additional $\approx 1.7\,\mathrm{eV}$ due to ro-vibrational excitations of ^{3}HeT. Thus, endpoint energy of atomic tritium T is about $8\,\mathrm{eV}$ lower than for molecular tritium T_2. This is about the same as $Q(\mathrm{T}) - Q(\mathrm{T_2})$, which is the difference in energy released by the nuclear reactions [OW08; FGR21], see Reaction 2.1. This difference in endpoint energy makes the atomic tritium spectrum very susceptible to contamination by molecular tritium, molecular background needs to be kept lower than 10^{-4} [Col+22]. Therefore, recombination of atoms into molecules needs to be suppressed during beam cooling and transport.

2.3. Measuring beam temperature with a time-of-flight system

An atomic tritium source is very different from the windowless gaseous tritium source currently used for molecular tritium. Atoms are produced in the form of a beam, for instance by thermal dissociation of molecules in a capillary heated to more than $2000\,\mathrm{K}$ (details in section 3.4). This beam is guided towards the spectrometers. This way, collisions of atoms with walls are avoided which would lead to recombination into molecules. To achieve high activity, the beam needs

to be slowed down by cooling it to mK-temperatures. This also lowers Doppler broadening to negligible values.

When generating an atomic beam by thermal dissociation, its temperature after creation is over $2000\,\mathrm{K}$. Cooling to mK-temperatures is performed in multiple stages. In the first stage, temperature is reduced to room temperature or below by a cold accommodator tube. When atoms of the tritium beam scatter on its surface, they exchange energy and cool down. To minimise the risk of recombination, temperature is chosen such that recombination probability per bounce is minimal. For aluminium, this is about $160\,\mathrm{K}$ [FGR21]. Also, atoms should not bounce more often than necessary for cooling.

Developing the accommodator, an optimal trade-off between cooling and suppression of molecular background is to be found. To gauge cooling efficiency, a test instrument is essential which measures beam temperature. A potential technique for this diagnosis are time-of-flight (ToF) measurements. The velocity of atoms is determined from measuring the time it takes them to cross a known distance. In this work, the velocity distribution of atoms in the beam is assumed to be represented by a beam temperature and to follow Maxwell-Boltzmann distribution, see details in subsection 4.3.1. This makes discussions clearer. In the future, it will be mandatory to understand the velocity distribution in more detail.

2.4. Goals of this work

Upgrading KATRIN to a cold atomic tritium beam source requires a beam cooling and a beam temperature measurement system. They are developed in experimental setups independently from KATRIN. In early phases, these setups are not tested with tritium T_2 to avoid contamination but mainly with protium H_2. This work prepares the construction of a ToF setup for temperature measurement. Therefore, calculations and supporting simulations in this work assume protium.

The analysis of ToF data is only straightforward in an ideal system of atoms flying in parallel. Deviations are expected from scattering atoms which spend more time in the ToF setup. Also, hot or cold atoms that interact with the system walls at room temperature are thermalised and change their velocity.

A framework needs to be developed, containing a setup for beam temperature measurement, the propagation of an atomic beam and the analysis of ToF data. It needs to fulfil the following goals in order to confirm the suitability of ToF and facilitate designing and optimising a proper prototype.

- A ToF distribution is generated from a simulated temperature measurement system. This consists of
  - beam formation in a capillary,
  - beam shaping in a skimmer setup and
  - a ToF measurement in a ToF setup.

- An algorithm extracts the beam temperature from the generated ToF distribution. The algorithm
  - considers systematic effects from scattering, thermalisation and pulsing of the rotary shutter,
  - is applicable to a range of beam temperatures between $100\,\mathrm{K}$ and $2500\,\mathrm{K}$ and
  - achieves an accuracy of the temperature determination better than at least $10\,\%$.
- The impact of design parameters, such as the geometries of the skimmer and the ToF tube, on accuracy are understood.

3. Particle propagation in vacuum systems

At low pressure, particles barely interact with each other but mainly with surfaces (section 3.1). Thus, particle propagation is determined from system geometry, temperature, material and surface roughness but not from gas density. Microscopically, this translates into particles scattering specularly or diffusely, the degree of their energy exchange with surfaces and their sticking time (section 3.2). With these parameters, programs like Molflow calculate the propagation of Monte Carlo simulated particles to yield pressure distribution in a system (section 3.3). Molflow is used in this work to simulate parts of a ToF system for temperature measurement. The setup of such a system is described in section 3.4.

3.1. Molecular flow regime

This section is based on [Sou86; Jou18]. Gases in vacuum are described by the ideal gas law, shown in Equation 3.1. In fact, this law is more correct at low pressure as it neglects interactions between gas molecules. A gas of low pressure is more diluted, so these assumptions are more correct. The distance that a molecule travels before it hits another molecule is the mean free path λ. Its product with pressure p depends on temperature T and particle diameter d, as shown in Equation 3.2. As a specific example, $\lambda p \approx 1.3 \cdot 10^{-4}\,\mathrm{m\,mbar}$ for hydrogen molecules at $300\,\mathrm{K}$, so in high-vacuum at $p = 10^{-3}\,\mathrm{mbar}$, mean free path is $\lambda = 13\,\mathrm{cm}$.

$$pV = NkT \tag{3.1}$$

$$\lambda p = \frac{k_\mathrm{B} T}{\sqrt{2}\pi d^2} \tag{3.2}$$

$$\tag{3.3}$$

Assume this vacuum to be in a chamber of size D, for instance a pipe. Its diameter L is much smaller than the exemplary mean free path of $13\,\mathrm{cm}$. Therefore, gas particles rarely scatter with each other but mainly at walls of the system. Particles move in straight lines and independently from each other. This type of flow is called molecular flow. It is separated from other regimes of flow by the condition of a Knudsen number $Kn > 0.5$. The Knudsen number is a measure of mean free path as compared to the size of the system, see Equation 3.4. A system is in viscous flow for $Kn < 0.01$ and in transition flow for $0.5 > Kn > 0.01$.

$$Kn = \frac{\lambda}{D} \tag{3.4}$$

3.2. Particle–wall interactions

Particles scatter at surfaces specularly or diffusely. In case of specular scattering, a particle leaves a surface on the opposite side of the surface normal as it was ingoing, but at the same angle. In case of diffuse scattering, the direction of an outgoing particle is independent of its incident direction [FY04]. The number of outgoing particles n per solid angle $\mathrm{d}\omega$ and a polar angle θ is given by Knudsen's cosine law, as shown in Equation 3.5. Following this distribution, an desorbing area $\mathrm{d}A$ emits the same number of particles per apparent area $\cos(\theta)\mathrm{d}A$ into any direction.

Both types of reflection occur for hydrogen. Molecules can scatter at surfaces specularly without exchange of energy if the surface is atomically smooth. Diffuse scattering occurs for higher surface roughness or when chemisorbed molecules in thermal equilibrium with the surface are desorbed [Chr88; QWW23].

$$\mathrm{d}n = \frac{1}{\pi}\, n \cos(\theta)\mathrm{d}\omega \qquad \text{from [Knu16]} \tag{3.5}$$

Particles exchange energy with surfaces when they scatter. In case of full accommodation, temperature of an outgoing beam T_{Out} is that of the wall T_{Wall}, independent from temperature of ingoing beam T_{In}. For partial accommodation, Equation 3.6 holds. Note that also other definitions exist, such as describing the change in velocity [KY11]. It might be supposed that diffusely scattered particles are fully accommodated as the adsorption also allows a completely changed direction. However, this is not always given, a combination of diffuse scattering and partial accommodation is observed for instance for atomically rough surfaces [Aue+77].

$$A_{\mathrm{Acc}} = \frac{T_{\mathrm{Out}} - T_{\mathrm{In}}}{T_{\mathrm{Wall}} - T_{\mathrm{In}}} \qquad \text{from [Aue+77; Sou86]} \tag{3.6}$$

When a particle is adsorbed at a surface, it stays there for a short time before being desorbed again. This sojourn time τ is given by Equation 3.7, so its value is determined from binding energy on the surface E, temperature T and vibration frequency ν_0 of the particle, which is typically $\nu_0 \sim 10^{-13}\,\mathrm{s}$. This equation is valid for first-order desorption, such as desorption of physisorbed molecules [Bag07] or atomic hydrogen [ELW98]. It is not valid for dissociatively chemisorbed molecular hydrogen. Physisorbed molecules have short times of about $\mathcal{O}(1\,\mathrm{ps})$ at room temperature. At temperatures below about $65\,\mathrm{K}$, this increases to the order of hours which is utilised for cryopumps [Bag07]. For chemisorption, hour-long sojourn times and up to virtually infinity occur already at room temperature, this is why vacuum system are heated to remove adsorbed molecules.

$$\tau = \frac{1}{\nu_0}\, \mathrm{e}^{E/RT} \qquad \text{based on [Bag07]} \tag{3.7}$$

3.3. Simulating particles in molecular flow regime with Molflow

Molflow[1] is a software that calculates properties such as pressure on the walls of a CAD model in molecular flow regime [KA19]. To do this, Monte Carlo simulations are conducted, so trajectories of test particles are calculated and quantities derived from their collisions with walls. Geometry consists of flat polygons, called facets, whose properties such as temperature or opacity is defined by the user. The linearity of a system in molecular flow regime is exploited so that test particles are independently simulated and one after another. This allows good performance and parallelisation as well as low memory usage. Statistical fluctuation shrinks with longer run time and higher number of simulated particles.

This section explains how Molflow models and calculates the trajectory of a particle from creation via propagation in the system to absorption. It also tells about information that can be extracted from the simulations. A most helpful source of information about functionality of Molflow is the documentation of its algorithm [2]. This is also the main source of this section.

At first, a model is needed in which particles should be simulated. Molflow provides tools to create simple geometries from scratch, such as creating polygons and connecting them. Complex geometries assembled in an external CAD program can be imported using for instance the file format STL.

Particles are generated at desorbing facets, their number is set as outgassing in $\mathrm{mbar\,L/s}$ or outgassing per area in $\mathrm{mbarL/s/cm^2}$, both quantities are automatically converted into each other. Velocities of desorbed particles follow Maxwell-Boltzmann distribution and correspond to the temperature of the respective facet. Angular distribution of emitted particles is also assigned for each facet and corresponds by default to the cosine distribution according to Knudsen, see section 3.2. Alternatively, a custom angular distribution can be assigned by providing a csv file. It lists the number of particles that should be emitted in each interval of polar and azimuthal angle.

Molflow is event-driven and does not require discrete time steps. Location of the respective next collision of a particle is determined by ray tracing from position and direction of movement, assuming the trajectory to be a straight line. Afterwards, the associated time of hit is determined from velocity.

Whenever a particle hits a facet, so when it scatters at walls, new angle and velocity are chosen for the further path. By default, the particle is re-emitted diffusely, so with a cosine distribution, but it is also possible to assign a combination of diffuse and specular scattering. The degree of thermalisation can be adjusted arbitrarily for each facet by accomodation coefficient A_{Acc}. By default, full thermalisation $A_{\mathrm{Acc}} = 1$ is assumed, so that the particle is re-emitted at a velocity corresponding to the temperature of the wall, which means independently of the impact velocity.

[1] Roberto Kersevan and Marton Ady. *MolFlow+*. Version 2.8.12. May 23, 2023. Available at: `https://molflow.web.cern.ch/`.

[2] Marton Ady. *Molflow 2.6 algorithm*. Mar. 3, 2016. Available at: `https://molflow.web.cern.ch/sites/default/files/molflow_docu.pdf`.

Without thermalisation, $A_{\mathrm{Acc}} = 0$, kinetic energy and velocity of the particle is maintained. For values in-between, accomodation coefficient describes the ratio of kinetic energies change. Velocity v_{New} of outgoing particle is given by Equation 3.8, with v_{Wall} a velocity of Maxwell-Boltzmann distribution according to temperature assigned to the wall. This equation is equivalent to Equation 3.6.

$$v_{\mathrm{New}}^2 = v_{\mathrm{Old}}^2 + A_{\mathrm{Acc}}(v_{\mathrm{Wall}}^2 - v_{\mathrm{Old}}^2) \tag{3.8}$$

After hitting a facet, particles are emitted instantaneously by default but a sticking time τ can be assigned for each facet. Distribution of sojourn time is determined according to the Frenkel equation by the parameters oscillation frequency ν_0 of the particle and absorption energy E, as explained in section 3.2.

Particles can be removed from the system when they hit a facet with a sticking factor s or pumping speed S unequal to zero. The two sizes are readily converted into one another automatically according to Equation 3.9, with v_{Avg} the average particle speed and A the surface area of the facet. Sticking factor s is between 0 and 1. All impinging particle are absorbed at $s = 1$, this represents an ideal pump.

$$S = s\,\frac{1}{4} v_{\mathrm{Avg}} A \tag{3.9}$$

For each facet, there are three counters stored which are updated at each hit of a particle. Firstly, the counter for the number of hits is incremented by 1. Secondly, total orthogonal momentum change $\sum I_\perp$ is increased by the momentum of incoming and outgoing particle, pressure is calculated from this value. Thirdly, sum of the reciprocals of orthogonal velocity components $\sum 1/v_\perp$ is stored. This last value is needed to calculate particle density near the facet as Molflow is event-driven and knows nothing that happens in volume. Still, number of particles in a volume near surface scales with the time that particles spend inside this volume, and this time is inverse to perpendicular velocity.

Molflow offers multiple ways to extract simulated quantities. Using textures, the number of hits per time, particle density, pressure, an estimation of average velocity and direction vectors can be displayed for a facet with selectable resolution and exported by the *texture plotter*. With profiles, pressure along an axis, incident angles of particles, velocity distribution or orthogonal or tangential velocity component can be recorded for a facet and displayed in the *profile plotter*. The *particle logger* stores properties of a limited number of particles that hit the selected facet, namely position, direction, velocity and time of each hit. The *histogram plotter* displays histograms of number of bounces, flight distance and flight time of particles before they were absorbed by the selected facet. Lastly, the same interface as used to provide custom angular distribution for desorption also allows to record and export angular distribution of incident particles.

Time-dependent simulations are also supported and require to define the times of interest and associated time windows beforehand. Simulation results for the defined time steps can be viewed individually. Viewing result for constant flow means the steady-state solution where all particles are tracked until absorption. Time-dependent parameters can be defined, their names

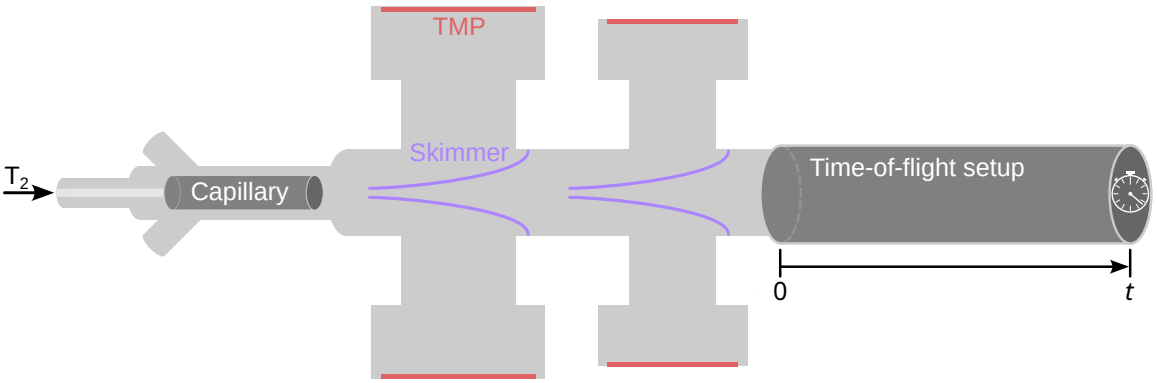

Figure 3.1.: **Sketch of a temperature measurement system** Tritium molecules T_2 are fed into a capillary which produces an atomic tritium beam. This beam is transported and focussed in a skimmer setup and finally enters a time-of-flight setup where its temperature is measured.

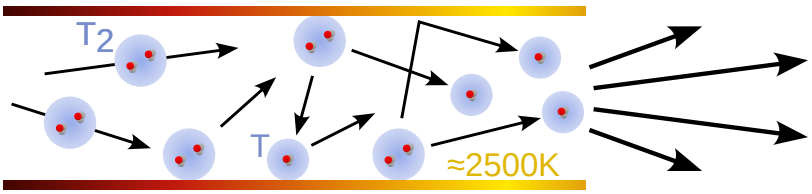

Figure 3.2.: **Atomic beam production by thermal dissociation** Tritium molecules T_2 enter a hot capillary in the left, are thermally cracked into atoms T and leave the capillary in the right.

are then entered as property of a facet instead of numerical values, this can be done for instance for outgassing, sticking factor or opacity. As an example, this way, behaviour of a system when opening a valve can be simulated by assigning falling opacity to an initially impermeable facet.

3.4. Setup of a time-of-flight experiment

An experimental setup is presented that measures the flight time of tritium atoms in order to determine their temperature. It consists of a particle source, a beam shaping section and a ToF setup. The system is described in the following and an overview is shown in Figure 3.1. A beam cooling system would be placed between particle source and beam shaping section but is not considered here.

Atomic beam formation in a capillary

The beam forming part of the particle source is a hot tungsten capillary of length L and diameter D. Capillaries used in literature have dimensions such as $L = 64\,\mathrm{mm}$, $D = 1\,\mathrm{mm}$ [TB98] or $L = 45\,\mathrm{mm}$, $D = 0.6\,\mathrm{mm}$ [BB93][ELW98]. The capillary is heated by electron bombardment up to

temperatures of $2600\,\mathrm{K}$, the electrons are emitted from a heated tungsten filament coiled around the capillary [TB98]. Alternatively, it can be heated more simply and reliably by thermal radiation up to about $2200\,\mathrm{K}$ [TFS08]. Only the section near exit is heated, so there is a temperature gradient along the axis.

The capillary is fed by tritium which naturally occurs in the form of molecules T_2. Inside the capillary, the molecules scatter at walls and are thermally dissociated into atoms T. The degree of dissociation rises significantly with temperature and is close to $100\,\%$ at $2600\,\mathrm{K}$ and at low pressure of $0.014\,\mathrm{mbar}$, as measured in [Tsc00]. Also, the particles are collimated as they pass through the capillary. This beam formation is a generally occurring process for diffusely scattered particles passing a tube [Day58]. Thus, a hot beam consisting of tritium atoms and molecules leaves the capillary. See a sketch of the process in Figure 3.2.

Transport and shaping of the atomic beam in a skimmer setup

The capillary is attached to the main compartment of vacuum chambers. The emitted beam is transported through these chambers and further focussed. To do this, one or multiple skimmers are attached in the system along beam flight path. The simplest skimmer is a pinhole disc, that can only be passed by particles near beam centre. A more effective skimmer is elongated along flight direction. It has a sharp circular edge which cuts off all particles that are too far away from beam centre. These particles hit the skimmer's outer side while the inner main part of the beam passes through the hole towards the ToF system.

All particles deflected by the skimmer or diverging from central beam should be removed from the system. Therefore, turbomolecular pumps (TMPs) are attached at the sides of the system, these are vacuum pumps specialised for high vacuum conditions. Whenever a particle hits a pump, there is a chance that the particle is pumped out. Otherwise it continues to scatter in the system until it is either pumped or passes the skimmer by chance. In the latter case, it contributes to the background of unwanted scattering atoms outside the beam.

Measurements in a time-of-flight setup

In a time-of-flight (ToF) setup, velocity of atoms is determined from measuring the time it takes them to cross a known distance. At the end of the flight distance is a mass spectrometer which measures the number of arriving atoms per time. Good time resolution is achieved by a quadrupole mass spectrometer that is mass-locked to the respective atomic mass, $m = 3\,\mathrm{u}$ in case of tritum [Coo+20]. However, the setup thus far would not work for a continuous atomic beam as measured intensity was constant. Therefore, the beam needs to be pulsed.

The beam is pulsed by a rotary shutter. This is a spinning disc with one or multiple openings. Its axis is placed outside the beam, so that it blocks the path of atoms most of the time but opens it periodically. As the beam should run along the central axis of the ToF tube, a widened compartment is needed to place the shutter in. The point of time when the beam path just opens needs to be synchronised well with the time-resolved measurement of the mass spectrometer.

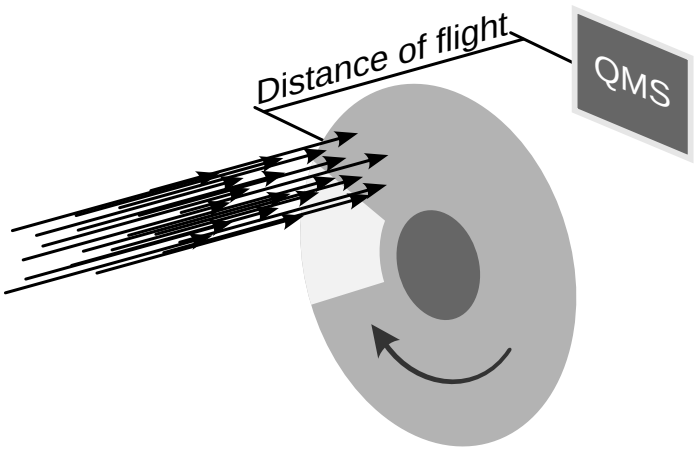

Figure 3.3.: **Sketch of a ToF setup** A rotary shutter opens periodically so atoms can pass. After a specific distance, they are detected by a quadrupole mass spectrometer (QMS).

4. Generating time-of-flight data from a simulated setup

A time-of-flight (ToF) system for temperature measurement of an atomic hydrogen beam is simulated. The system is split into three subsystems, all of which are simulated separately. The particle source is a hot capillary, discussed in section 4.1. It generates the atomic beam and defines its shape. The calculated beam shape is used as input of the second subsystem which is a skimmer setup. It transports and shapes the hydrogen beam, it is covered in section 4.2. The output of the skimmer setup is used as input of the last subsystem, a ToF setup. This consists of a rotary shutter and a mass spectrometer in a tube, it measures flight time of the hydrogen atoms and is discussed in section 4.3. An overview of the three subsystems is given in Figure 4.1.

Beam shape depends on the geometry of each subsystem as the three subsystems build upon each other. And the beam shape in turn determines the flight time measured in the ToF setup. The influence of geometry on beam shape and ToF distributions is discussed, based on simulation results and analytical models.

4.1. Atomic beam shape from formation in a capillary

An atomic hydrogen beam is produced by thermal dissociation of molecules in a capillary heated to more than $2000\,\mathrm{K}$ (details in section 3.4). This section deals with the beam shape at the exit of the capillary. In subsection 4.1.1, an analytical calculation of the beam's angular distribution is presented, as conducted by Tschersich [TB98; TFS08]. In subsection 4.1.2, the angular distribution is determined a second time but then not by analytical calculations but by Monte Carlo simulated particles. This still follows Tschersich's model and is performed by implementing it in Molflow. In contrast to the analytical calculation, the simulated version describes beam shape spatially resolved. This spatial dependence is discussed in subsection 4.1.3 and a beam source is modelled in Molflow which recreates the simulated output. In subsection 4.1.4, the differently implemented beam sources are compared.

4.1.1. Analytical calculation of the angular distribution

An analytical description of an atomic beam, emanated from a hot capillary, is given by Tschersich [TB98; TFS08]. In the following, the focus is put on the beam shaping model. Other aspects, such as the efficiency of molecular cracking into atoms, are not taken into consideration.

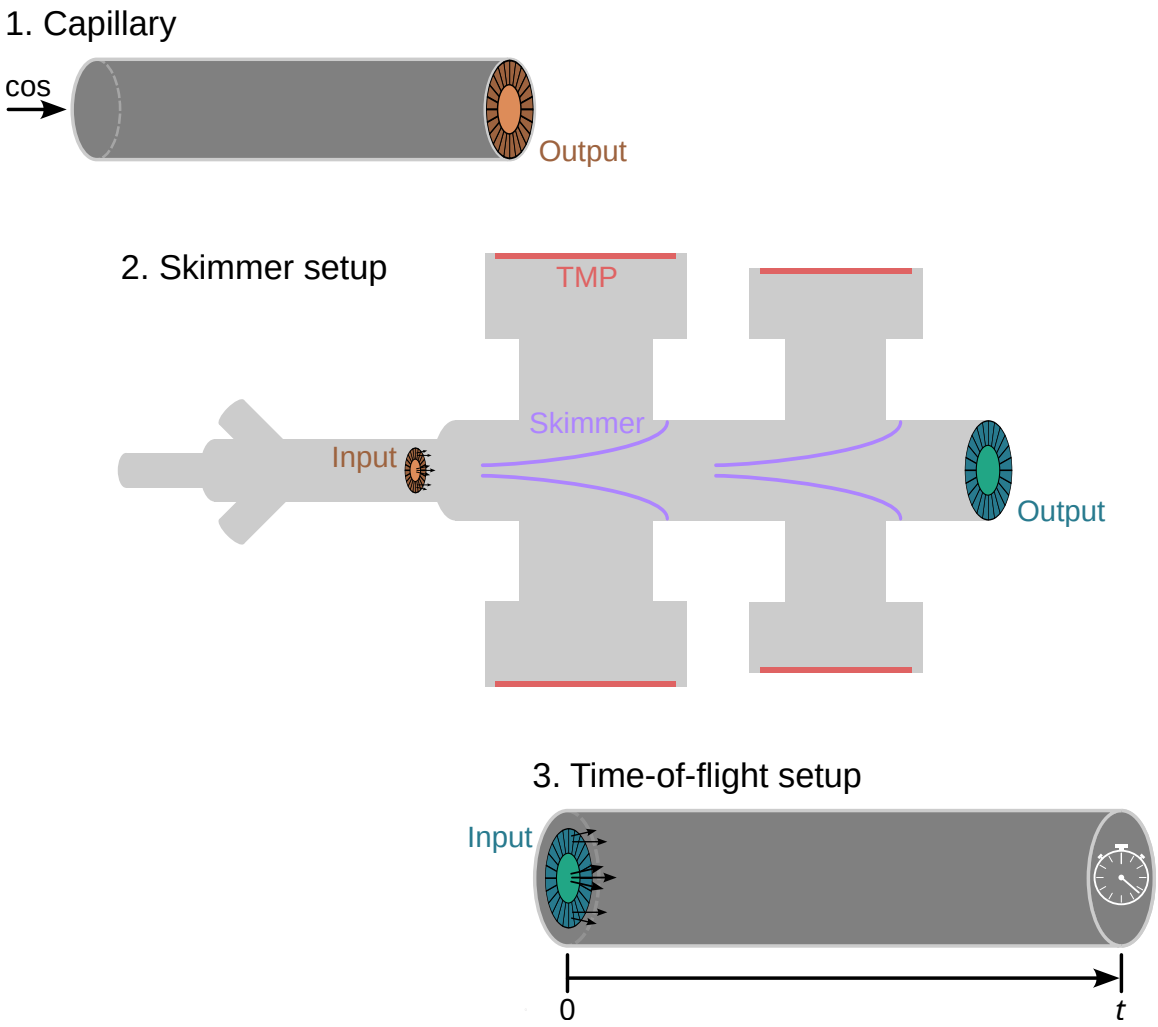

Figure 4.1.: **Subsystems of a temperature measurement system** The setup is separated into three subsystem which are simulated individually. Particles propagate from the inlet of the capillary to the detector of the ToF setup. The output of a subsystem is used as input of the subsequent subsystem.

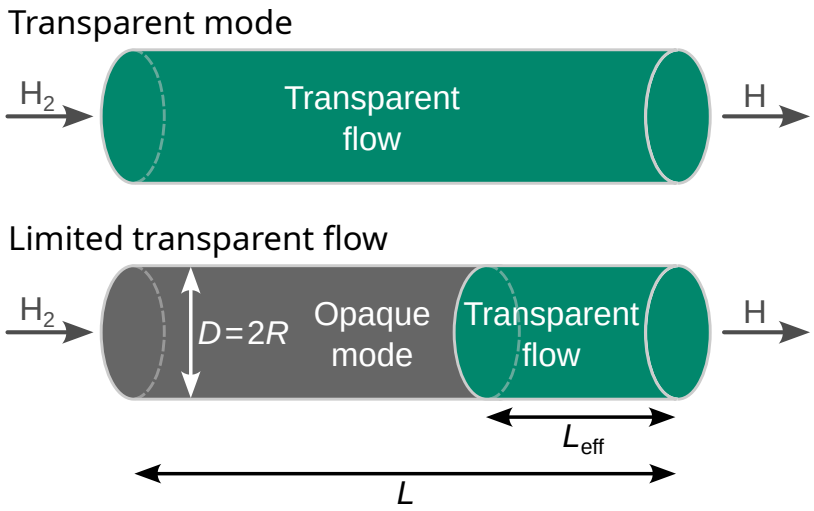

Figure 4.2.: **Atomic hydrogen source capillary according to the Tschersich model** A flow of hydrogen molecules H_2 enters a tube of diameter D, radius R and length L and leaves as atomic flow H. Two cases are shown: At low initial pressure (upper capillary), the whole tube is in transparent mode. For higher initial pressure (lower capillary), the tube is transitional flow or opaque mode near the entrance (marked in grey). Transparent flow is limited to a final section of length L_{eff} (marked in green).

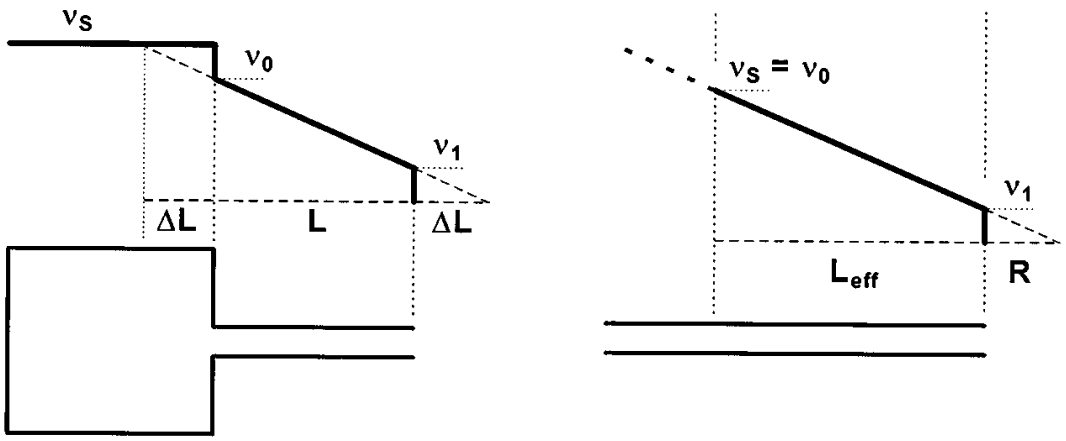

(a) Transparent mode.

(b) Limited transparent flow.

Figure 4.3.: **Wall flux density profile $\nu(x)$ according to the Tschersich model** These two figures refer to the same two cases as illustrated in Figure 4.2, with flux density ν_S in the source chamber at thermal equilibrium, ν_0 at the entrance and ν_1 at the outlet. Figure from [TB98], subfigures rearranged horizontally.

In the model of Tschersich, the capillary is a tube of diameter D, radius R and length L. It will later be characterised by the reduced length $l = L/D$. A flow of hydrogen molecules H_2 leaves a source chamber with a cosine distribution, enters the tube, scatters diffusely at the tube walls and leaves as atomic flow H. Two cases are treated in the following which differ in the pressure in the source chamber. To start with the simpler case, pressure is assumed so low that mean free path $\lambda > 10L$. This corresponds to flow in transparent mode in the whole capillary, as shown in the upper capillary of Figure 4.2.

To calculate the angular distribution of particles leaving the capillary, the profile of the wall flux density $\nu(x)$ at position x along the tube needs to be known. $\nu(x)$ is the rate at which molecules are scattered at and reemitted from surface elements of the tube, with the flux density ν_S in the source chamber at thermal equilibrium, ν_0 at the entrance and ν_1 at the outlet. The profile of $\nu(x)$ is calculated by [Cla30; Day58; OK70]. An approximate solution by Clausing [Cla32] yields a linear decrease over x along the capillary, as shown in Figure 4.3a. There are density steps at the tube entrance and at the exit, they have equal height of $\nu_1 = \nu_S - \nu_0$. These density steps depend only on reduced length $l = L/D$ and require numerical calculations to be determined exactly, lists of expressions from various theories are given in [OK70; AM86]. However, $\nu(x)$ can be extrapolated before tube entrance and behind outlet by a virtual extension ΔL so that flux densities there are $\nu(-\Delta L) = \nu_S$ and $\nu(L + \Delta L) = 0$, respectively, see Figure 4.3a. This yields the simple relation $\Delta L = R$ and Equation 4.1 [Hel67]. The angular distribution $j(\theta)$ is yielded when inserting this reduced density step ν_1/ν_S into Equation 4.2 which is based on [OK70]. Tschersich states that the deviation between this $j(\theta)$ and numerical results increases with l but is below $0.8\,\%$ up to $l = 10$. Note that angular distribution $j(\theta)$ would reduce to a cosine distribution if there was no gradient in flux density $\nu(x)$.

$$\frac{\nu_1}{\nu_S} = \frac{1}{2l + 2} \qquad \text{from [TB98]} \tag{4.1}$$

$$\begin{aligned} j(\theta) &= \frac{4}{3\pi}\left(\frac{\nu_0}{\nu_S} - \frac{\nu_1}{\nu_S}\right)\frac{1}{l}\frac{\cos^2(\theta)}{\sin(\theta)}\left(1 - V(\beta)\right) + \frac{\nu_1}{\nu_S}\cos(\theta)\left(1 - U(\beta)\right) + \cos(\theta)U(\theta) \\ \text{with}\quad & \begin{cases} U(\beta) = (2\beta - \sin(2\beta))/\pi\,,\ V(\beta) = \sin^3(\beta)\,, & \text{for } \theta < \arctan(1/l) \\ U(\beta) = V(\beta) = 0\,, & \text{for } \theta \geq \arctan(1/l) \end{cases} \\ \text{and}\quad & \beta = \beta(\theta) \text{ with } \cos(\beta) = l\tan(\theta) \qquad \text{from [TB98]} \end{aligned} \tag{4.2}$$

Another case is now considered. The pressure in the source chamber is increased such that the tube is in opaque mode, which holds for $10L > \lambda > 2R$, or in transition flow near the entrance. In this regime, molecule–molecule interactions occur. Flux density $\nu(x)$ decreases along the tube until it is again in transparent flow with $\lambda > 10L$ in the final section of effective length L_{eff}. Tschersich calls this limited transparent flow, see the lower capillary in Figure 4.2 and Figure 4.3b. Hanes [Han60] assumes in a similar model that transparent flow starts at the position where mean free path λ is equal to the remaining length of tube. This assumption is not applicable here as flow in the capillary is complicated due to more intense heating closer to the outlet. Instead,

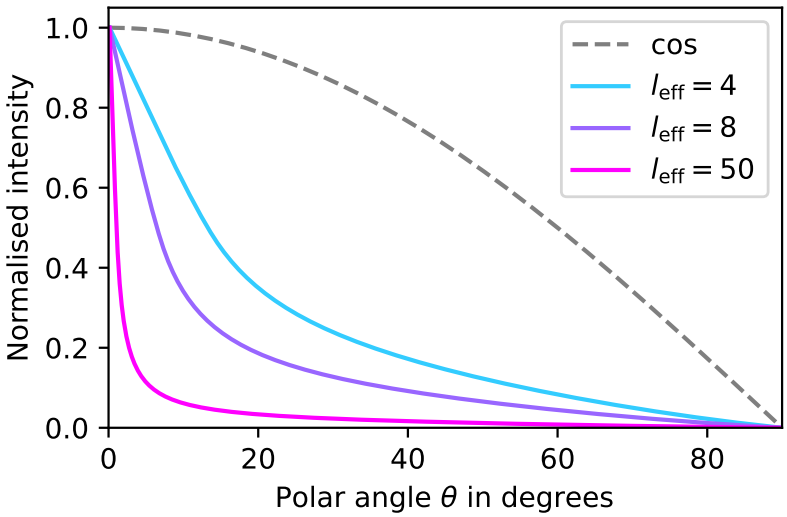

Figure 4.4.: **Angular distribution according to the Tschersich model** Angular distribution $j(\theta)$ of an atomic beam formed by a tube with limited transparent flow as described by Tschersich [TB98]. The distribution is shown for different effective reduced lengths $l_{\mathrm{eff}} = L_{\mathrm{eff}}/D$. For comparison, the grey dashed line shows a cosine distribution.

reduced effective length $l_{\mathrm{eff}} = L_{\mathrm{eff}}/D$ is used as a free fit parameter. The larger l_{eff}, the more focussed the beam.

For limited transparent flow, particles no longer enter the section of transparent flow from the source chamber. Still, it is assumed that they have a cosine angular distribution when entering. This can be imagined to be imposed by a virtual membrane at L_{eff} before the outlet. As transparent flow section begins somewhere along the tube, it does not make sense to assume a flux density step at this position of the tube, so $v_0 = v_{\mathrm{S}}$ as shown in Figure 4.3b. Thus, the relation describing the reduced density step v_1/v_{S} at the outlet using virtual tube extension ΔL changes slightly and it now depends on effective reduced length l_{eff} instead of reduced length l of the capillary. This results in Equation 4.3 replacing Equation 4.1. Also, l_{eff} replaces l in Equation 4.2, so reduced length l of the capillary is irrelevant for the angular distribution.

$$\frac{v_1}{v_{\mathrm{S}}} = \frac{1}{2l_{\mathrm{eff}} + 1} \qquad \text{from [TB98]} \tag{4.3}$$

To expand on this model, it is pointed out that beam forming might already start in opaque section. There are particles without intermolecular collisions which contribute to beam forming and also colliding particles which counteract. As flux density $v(x)$ decreases continuously, a position exists where beam collimation and broadening are almost balanced. At this point, cosine angular distribution is assumed and beam forming section begins.

Angular distribution yielded by this model is shown for exemplary reduced effective lengths l_{eff} in Figure 4.4. In comparison to cosine distribution fed into capillary, emitted particles are strongly

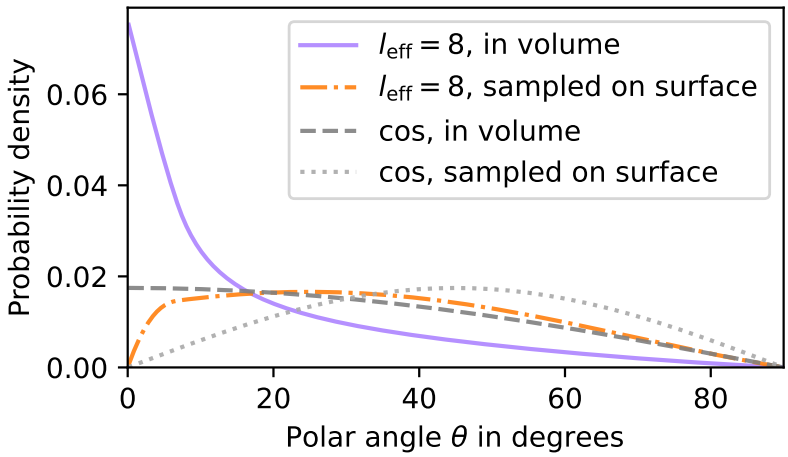

Figure 4.5.: **Volume correction of angular distribution** The solid purple line is the same as in Figure 4.4. It describes the angular distribution in volume for a capillary of effective reduced length $l_{\mathrm{eff}} = 8$ while the dash-dotted orange line shows angular distribution as sampled on a surface. Correction to volume is done by division with $\sin(\theta)$. For comparison, the grey dashed and dotted lines show a cosine distribution.

focussed, so the majority of particles is emitted under small polar angles θ. Higher l_{eff} leads to stronger focussing.

4.1.2. Monte Carlo simulation of the angular distribution

The model by Tschersich of limited transparent flow, presented in subsection 4.1.1, is implemented in Molflow. Only the final section of limited transparent flow needs to be modelled but in the same way as Tschersich describes it. Thus, the geometry of the Molflow simulation is a cylinder of length L_{eff} and diameter D. Its inlet surface is assigned to emit particles with a cosine distribution. Outgassing rate, temperature and particle mass are arbitrary as neither flight time nor absolute pressure are of interest here. Particles are set to scatter diffusely at walls. This also holds for all other simulations in this work unless noted differently since surfaces of the experimental setup are assumed to be atomically rough. The outlet surface records the angular distribution of incident particles. This is stored as the number of particles detected in each interval of the polar angle spectrum. The resolution is chosen arbitrarily by setting the number of intervals.

This simulation is not an attempt of simulating the entire capillary as realistic as possible. Modelling the processes inside the capillary would require to know the temperature along the capillary and to take particle–particle collisions into account. Instead, this is a Monte Carlo version of Tschersich's model without analytical calculations. This avoids the approximations of linear flux density $\nu(x)$ and the expression of the reduced density step ν_1/ν_{S}. Further, assumptions of the model can be modified without redoing analytical calculations, gaining insight into their significance and robustness of the model. This provides deeper understanding which is a step

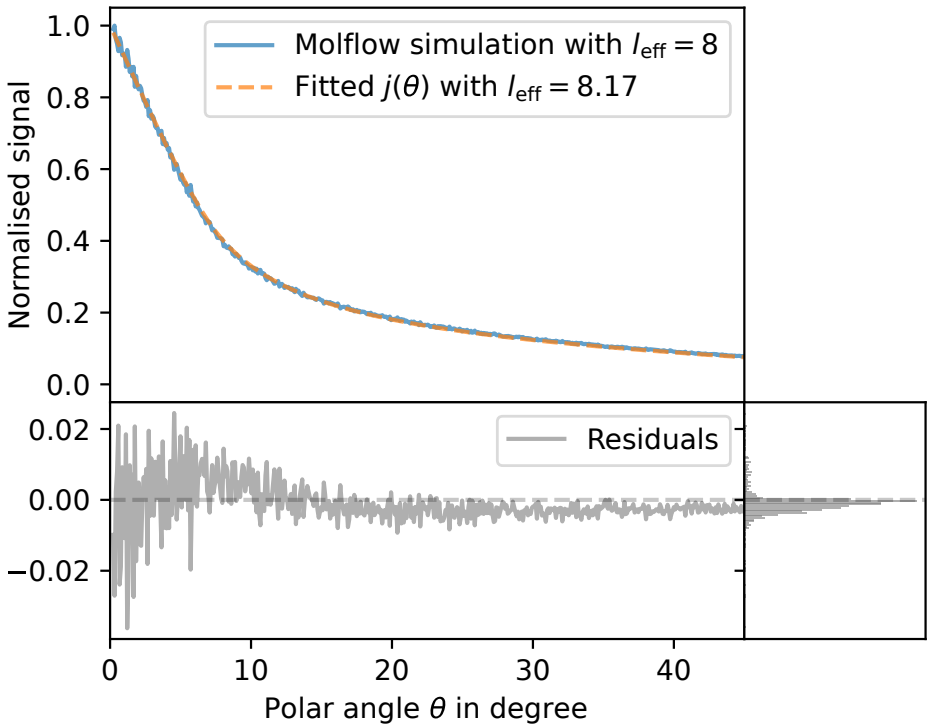

Figure 4.6.: **Angular distribution by Molflow simulation** A volume corrected angular distribution recorded by Molflow is shown in blue for a capillary of effective reduced length $l_{\text{eff}} = 8$. Analytical angular distribution $j(\theta)$ by Tschersich is fit to this data with the free parameters l_{eff} and scaling in y-direction. Best agreement is achieved for $l_{\text{eff}} = 8.17$.

on the way to a full simulation of the capillary, including particle–particle interactions and non-homogeneous temperature at walls, so with non-linear flux density $v(x)$. Another benefit drawn from the simulation is spatially resolved data about angular distribution and density on the outlet surface. Even though this is outside the scope of Tschersich's model, its assumptions are general enough to consider this spatial data meaningful. Best possible results in the consecutive simulation are expected to be achieved if spatial data is considered instead of dismissed.

This is different from the number of hits for each polar angle θ onto same areas, which would be referred to as angular distribution in volume. The difference is due to larger target area for larger polar angles. For example, the area of a hemisphere under a polar angle θ from $80°$ to $90°$, so near equator, is more than ten times larger than the area from $0°$ to $10°$, near the pole. Solid angle ω is calculated in spherical coordinates as $\mathrm{d}\omega(\theta, \phi) = \sin(\theta)\, \mathrm{d}\theta\, \mathrm{d}\phi$ with azimuth angle ϕ, so the correction for different areas is a division by $\sin(\theta)$, followed by normalisation. The effect of this correction is shown in Figure 4.5. The division by small values of $\sin(\theta)$ for small polar angles θ already hints at high noise after correction due to low statistics when sampled on surface. The correction needs to be applied to all angular distributions obtained from Molflow, except those from the *particle plotter* feature if the implemented surface-to-volume conversion is already used.

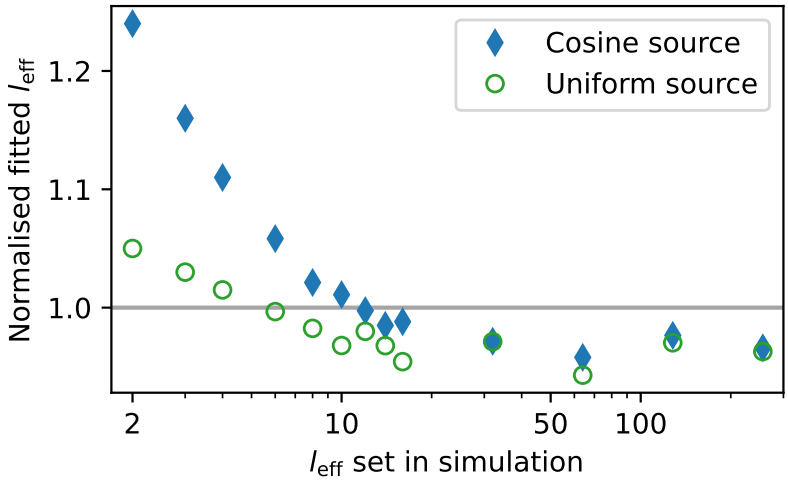

Figure 4.7.: **Analytical angular distribution fit to Molflow simulations** The analytical angular distribution $j(\theta)$ by Tschersich is fit to the distributions yielded by simulations in Molflow with the free parameters l_{eff} and scaling in y-direction. For different cylinder lengths l_{eff} in Molflow, relative deviation of fitted l_{eff} is shown. This is shown for the original assumption of particles entering beam forming section with a cosine distribution and also for entering with an uniform distribution.

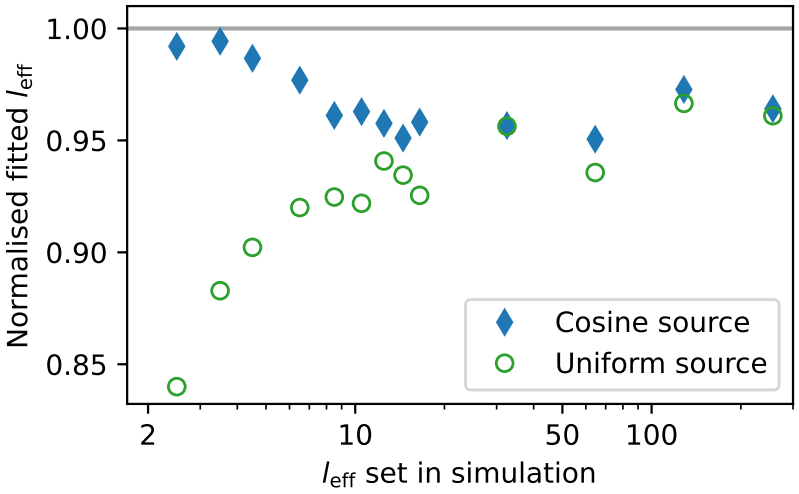

Figure 4.8.: **Analytical angular distribution fit to Molflow simulations with corrected virtual extension** Like Figure 4.7 but simulated l_{eff} is scaled to no longer include virtual backward extension $\Delta L = R$ of the tube in order to compensate for missing entering density step.

An angular distribution determined from a Molflow simulation is shown in Figure 4.6. Its shape looks very similar to those by Tschersich shown in Figure 4.5 but in direct comparison some deviations show up, especially for short capillaries. However, much better agreement is observed when l_{eff} of the Tschersich distribution $j(\theta)$ is allowed to be different from cylinder length used in Molflow simulation. In Figure 4.6, best agreement for $l_{\mathrm{eff}} = 8$ in Molflow is found for $j(\theta)$ for $l_{\mathrm{eff}} = 8.17$. Deviations are then below $1\,\%$ when not taking into account noise at small polar angles θ due to surface-to-volume correction.

In case of effective reduced length $l_{\mathrm{eff}} = 8$, the difference to fitted l_{eff} is small but this depends on the simulated value of l_{eff}. In Figure 4.7, relative deviation is shown in blue. Apparently, the offset is largest for short tubes, so they produce a beam in Molflow which is shaped as if the simulated cylinder was longer. The discrepancy is too large to be attributed to deviations by approximations in the derivation by Tschersich. For longer effective length, fitted l_{eff} seems to converge to a value close to 1, this difference might be due to approximations.

Remembering the derivation by Tschersich for transparent flow, a virtual backward extension $\Delta L = R$ of the tube is assumed in order to describe the step in flux density $\nu(x)$ at the particle source by extrapolating it to chamber density using $\nu(-\Delta L) = \nu_{\mathrm{S}}$. For limited transparent flow, the extrapolation for this entering density step is omitted since $\nu_0 = \nu_{\mathrm{S}}$. This difference in the definition of l_{eff} is not resembled in the simulation in Molflow. It is assumed but not clear that outgassing facets in Molflow behave like a virtual source chamber. Under this assumption, for limited transparent flow, angular distribution $j(\theta)$ by Tschersich needs to be compared to slightly longer l_{eff} than modelled reduced length. As seen from Figure 4 in [TB98], modelled length L_{eff} needs to be multiplied by $(L_{\mathrm{eff}} + \Delta L)/L_{\mathrm{eff}} = (l_{\mathrm{eff}} + 0.5)/l_{\mathrm{eff}}$ in order to cover the same range of flux density.

Applying the correction of the virtual extension to l_{eff} yields the blue data in Figure 4.8. Effective lengths l_{eff} of best fits of Tschersich's distribution to simulated angular distributions then deviate by a maximum of $5\,\%$ and only into the direction of greater simulated lengths. Statistical uncertainty of fit results shown in the plot has not been estimated and might not explain the structure still seen in the curve shape. Still, the good agreement shown in this plot demonstrates the viability of this method.

To further test understanding of how the Tschersich model behaves, one of its assumptions is changed. The initial angular distribution of particles entering beam forming section of the capillary, which is imposed by the virtual membrane, is changed from a cosine distribution to an uniform one. In Molflow, this is realised by changing the outgassing behaviour of this one facet. Simulations yield the green data in Figure 4.7 and Figure 4.8. Effective lengths from fit that describe the simulated angular distributions best are always smaller than in the case of initial cosine distribution. This is expected since beam focussing happens steadily over the length of the capillary and a cosine distribution is already more collimated than an uniform distribution. Therefore, a specific share of the tube is imagined to be accounted for the focussing of an uniform distribution to the level of collimation of a cosine distribution, thus leaving less length for further focussing. Also, since this requires a specific absolute distance, the difference diminishes for larger capillary lengths. It is intuitively clear that for a very long tube, the initial distribution should barely make any difference when considering the output.

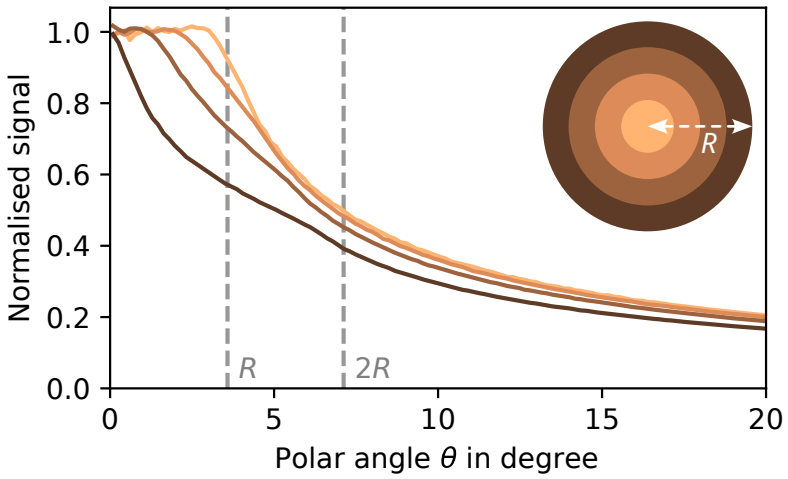

Figure 4.9.: **Radial dependence of angular distribution** Volume corrected angular distributions on the capillary outlet for reduced length $l_{\text{eff}} = 8$. Distributions are recorded by Molflow at concentric rings of different radius as shown in the inset. Signal intensities are divided by the different ring areas but are otherwise all normalised by the same factor which sets total angular distribution at $\theta = 0°$ to 1. Vertical dashed lines mark the angles under which a radial distance of R and $2R$ is crossed over the whole capillary length.

The coherent explainability of results from Molflow simulations and good agreement with angular distribution derived analytically by Tschersich, which itself is known to be slightly impaired by approximations, gives confidence in not only putting trust in the angular distributions determined by simulation but also to extract further information not described by Tschersich. The model seems sufficiently general to not be strictly constrained to a description of angular distribution.

4.1.3. Spatial dependence on the outlet of a capillary

The inhomogeneity of particle emission on the outlet surface is investigated. Figure 4.9 shows angular distributions on rings with different radii on the outlet, apparently they depend on radial position. A plateau is seen for the central beam part for small polar angles θ. It stems mostly from particles that hit the outlet directly. As particles can spawn on the capillary inlet with a maximal radial distance of about one radius R, the corresponding polar angle $\theta = \arctan(R/L_{\text{eff}}) = \arctan(0.5/8) \approx 3.6°$ is the cut-off of the plateau. For more outward rings, the maximum angle of the plateau is smaller, accordingly to the distance from edge to ring.

A second kink is seen most clearly for the outermost ring near $\theta = \arctan(2R/L_{\text{eff}}) \approx 7.1°$. It is produced from particles that cross the whole diameter $2R$, so this is the cut-off of direct hits on the outlet. For more inward rings, this happens at accordingly smaller angles and is less visible. Both kinks are washed out by the finite width of rings and the presence of scattered particles. Possibly, the relation between angular distribution and position could be harnessed to yield a more collimated beam but this is not considered here.

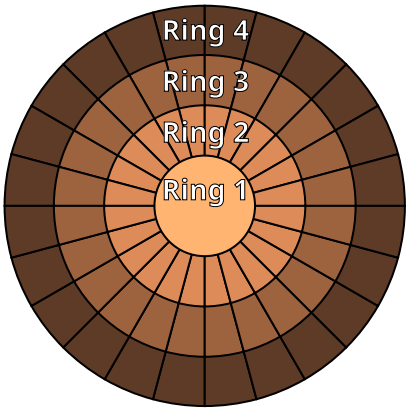

Figure 4.10.: **Segmented capillary surface** Sketch of the capillary outlet described by a number of facets, arranged into rings. Only the innermost ring is a single facet while all other rings consist of multiple facets, in the simulations 90 facets.

Knowledge about beam shape gained previously is necessary to find out about particle trajectory in further parts of the atomic hydrogen source setup, at first in the skimmer setup which will be described in section 4.2. That is a computationally intensive simulation and implementing the capillary explicitly in the same run would further increase cost. For reduced length $l_{\mathrm{eff}} = 8$, each particle fed into the capillary hits tube walls on average about a hundred times before reaching the outlet, and this increases greatly for larger l_{eff}, so this is in general not feasible. Therefore, a surface needs to be implemented which emits particles without further calculation and mimics the capillary as closely as possible.

A potential replacement of capillary in Molflow is a facet that emits particles with an angular distribution as calculated in the previous subsection. However, this comes with several flaws compared to the beam produced by an explicitly simulated capillary.

Firstly, a single homogeneous facet does not respect that angular distribution depends on radial position on the outlet surface, as was shown in Figure 4.9. Particles emitted near the edge of the outlet are more focussed while more central parts of the beam tend to stray into larger polar angles.

Secondly, particle density is not homogeneous on the outlet surface, as can also be seen from different integrals of the curves in Figure 4.9. In the centre of outlet, density is about $20\,\%$ higher than near the edge, independently from reduced effective length l_{eff}.

Lastly, as mentioned in section 3.3, particles are created by Molflow by default with random azimuthal angle φ. As the procedure described until now provides Molflow only a custom angular distribution for polar angle θ, the default applies for azimuth. Thus, it is not respected that particles tend to travel outwards but here they have the same chance when spawning on one side of the outlet facet to be emitted into the opposite direction.

To address these limitations, capillary outlet is implemented as an arrangement of multiple facets. As shown in Figure 4.10, the surface is split into rings which themselves consist of several segments. This way, variations in polar angle distribution and in density are considered per ring.

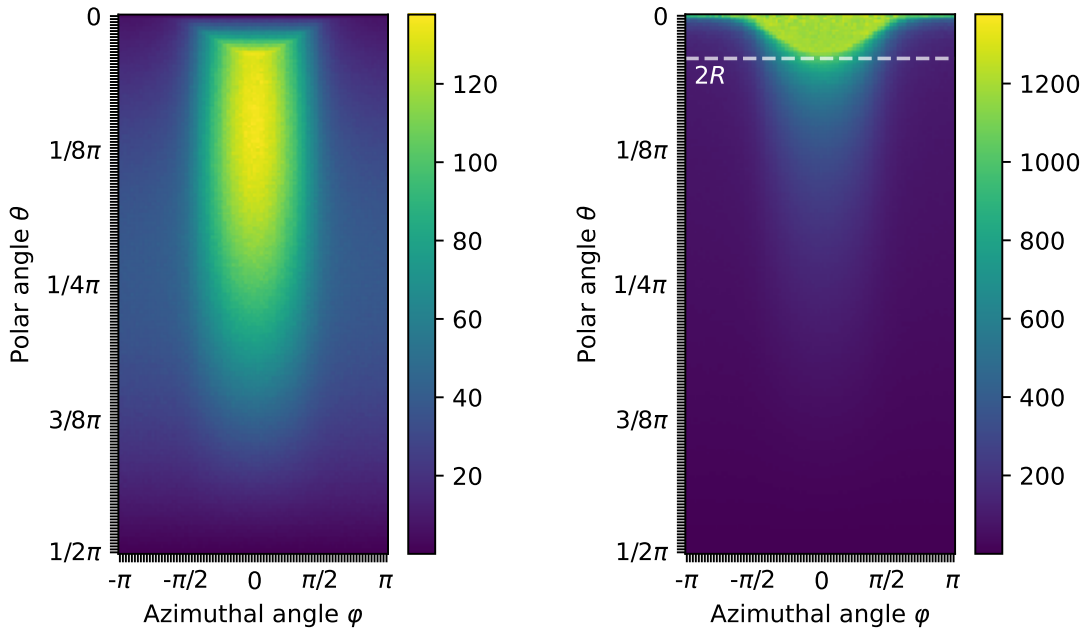

(a) Colour shows raw number of hits.

(b) Colour shows volume-corrected hits in arbitrary units.

Figure 4.11.: **Angular distribution on a segmented capillary surface** Simulated polar and azimuthal angular distribution for a capillary of reduced length $l_{\text{eff}} = 8$ on the outermost of ten rings on its outlet. The distribution is averaged over all facets of the ring, so the same is used on the inlet of the skimmer setup simulation in section 4.2. Horizontal dashed line in Figure 4.11b marks the angle θ under which the whole diameter $2R$ is crossed over the whole capillary length.

Azimuthal angle distribution is even resolved with the number of facets. The process of efficiently yielding such segmented outlet surface is described in the following.

After geometry of the segmented surface is created in Molflow in the capillary simulation, it is placed at the position of the former outlet facet. The simulation is run, so particles are emitted by the inlet with a cosine distribution, they travel through the tube, scatter diffusely at walls and finally, each facet records particle hits and incident angles separately. Angles θ and φ are measured relative to reference axes for each segment. As these axes and the segments are aligned cylindrically symmetric to the centre of surface, angular distributions look the same for all facets, apart from statistical fluctuations. Therefore, angular distributions of all segments of the same ring are averaged in order to improve statistics, yielding a distribution like Figure 4.11. Outgassing rate of a facet is the average number of particle hits on segments of the corresponding ring.

A high number of 90 facets per ring is chosen as this reduces blurring of azimuth information while not degrading statistics. In contrast, more rings require in total more simulated particles to keep noise low and it also means a higher manual effort to process angular distributions as this needs to be done for all rings individually. Depending on statistics of the result after averaging, angular distribution is smoothed to effectively imitate more ideal data, avoid outliers and potential artefacts. Smoothing is performed by bivariate spline approximations on a sphere, most often over a rectangular mesh [1]. In the case of Figure 4.11, no further smoothing is necessary.

An angular distribution is calculated as described for each ring of the segmented capillary surface separately. It is then assigned to each facet of this ring. This way, high resolution is achieved while at the same time statistics is preserved. No surface-to-volume correction by dividing with $\sin(\theta)$, explained in Figure 4.5, is applied as the output files would need to be converted back to surface anyway. Also, conversion is only exactly correct for infinitely many bins of θ so this would introduce errors when interpolating in volume view. For plotting, angular distribution can be converted at any time, see Figure 4.11b.

Close to the edge of capillary, atomic beam is focussed in outward direction as seen in Figure 4.11 from the higher intensity for small azimuth angles φ, with $\varphi = 0$ pointing exactly outwards and $\varphi = \pi$ inwards. Closer to the centre of capillary surface, intensity is more constant over azimuth angle, this is not shown here. This observation is expected from cylinder symmetry near centre. Also, there is only little chance for a particle to be emitted to inward direction near the edge since this requires hitting the wall close to the outlet and being desorbed almost parallel to the wall.

Figure 4.11b is similar to an azimuthally resolved version of the outermost curve in Figure 4.9. For outward direction, so near $\varphi = 0$, it shows a plateau up to the polar angle $\theta \approx 7.1^\circ$ of crossing the whole diameter $2R$. This was seen as a kink in Figure 4.9 and was attributed to direct hits, which is consistent with the plateau. For other φ, majority of particles is more focussed into normal direction, so averaging with these components causes the increase in intensity for smaller polar angles θ seen in Figure 4.9.

[1] Information about the used implementations in *scipy* (used version: 1.10.0) at: `https://docs.scipy.org/doc/scipy/reference/generated/scipy.interpolate.RectSphereBivariateSpline.html` and `https://docs.scipy.org/doc/scipy/reference/generated/scipy.interpolate.SmoothSphereBivariateSpline.html`.

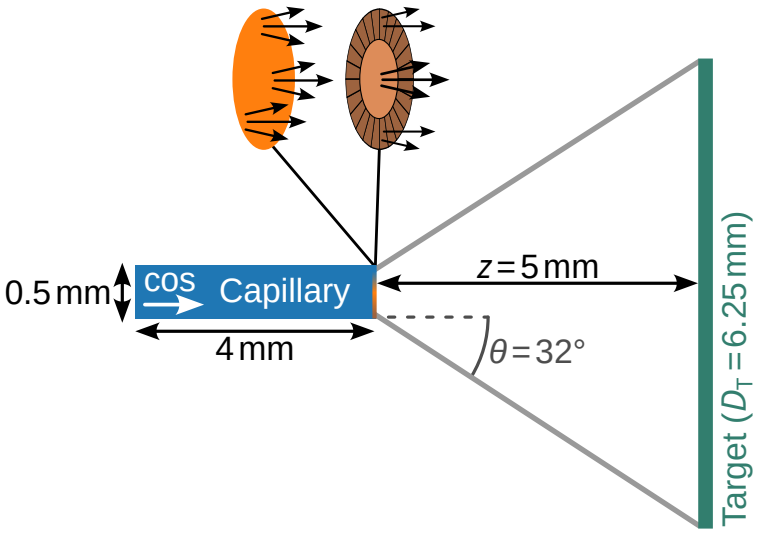

Figure 4.12.: **Setup of measuring beam shape on a target** Particles are emitted by a source in the left of the sketch, for instance by the model of a capillary or by a desorbing surface. In a distance z, they reach a plane with a target which counts number of impinging particles.

This investigation has found significant inhomogeneity and structure in particle emission of the capillary. This needs to be respected in further simulations in order to achieve best possible results. A way to efficiently utilise knowledge about spatial resolution of beam shape production was shown.

4.1.4. Benchmarking differently modelled beam sources

The method of imitating a capillary efficiently by a segmented surface as presented in subsection 4.1.3 is benchmarked. To this end, a way of measuring beam shape from different sources is shown and results are compared. To take into account both angular distribution and its spatial dependence on the source, beam profile is measured on a plane in some distance from the source. This is a clear measure to estimate the evolution of beam shape for different travelled distances.

As sketched in Figure 4.12, a separate simulation is set up with the particle source that is about to be benchmarked. Additionally, a target is placed centred with the source's main emission direction, for instance in extension of the capillary axis. The target is a large circular facet with sticking factor 1 that detects majority of particles. A perfectly sticking transition between target and source should be added to the Molflow simulation since the program expects all particles to be absorbed at some facet.

Information about distribution of hits is gained by exporting a profile of the target surface using Molflow's *profile plotter* feature. A profile describes total number of particles hitting the target along an axis through its center. This needs to be differentiated from a cross section, see Figure 4.13 for comparison. In the context of this work, profiles without normalisation are usually

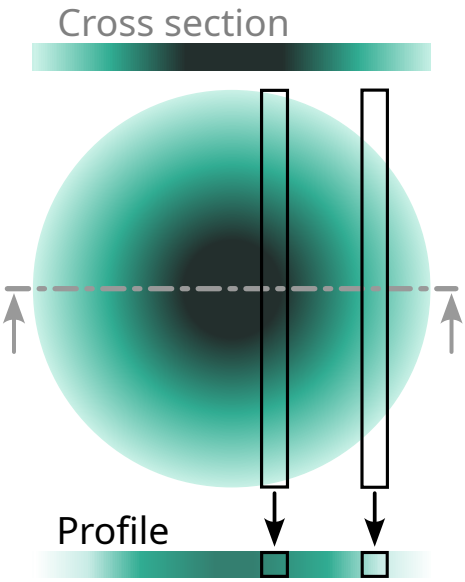

Figure 4.13.: **Profile of a surface** Assuming a cylindrically symmetric density distribution on a surface, a cross section describes density when slicing through the center of the surface. In contrast, a profile as calculated by Molflow describes at each position the sum of all particles along a perpendicular axis.

best suited since this is the raw number of simulated particles hitting the facet. In contrast, other normalisations offered by Molflow take into account only the normal component in case of pressure or multiply by reciprocal particle velocity in case of gas density. The number of desorbed particles might need to be noted and used to manually normalise hit counts in order to compare results with other simulations.

The size of target facet is a trade-off between covering a large angular range and good resolution since profiles in Molflow always consist of exactly 100 bins. If higher resolution is needed near centre, an additional smaller and transparent facet can be placed just in front of the main target. Alternatively, a texture counting absorption can be enabled on the target with arbitrary resolution. Using the *texture plotter*, it is possible to approximately extract a cross section from central rows of cells. However, this is statistically inferior as only part of simulated data is used. A profile can also be calculated from texture.

To compare different implementations of the capillary, benchmarks with geometry as in Figure 4.12 are set up. In total, four separate simulations are run: Twice, segmented surfaces as described in subsection 4.1.3 are used, so they emit particles with angular distributions that have previously been recorded in simulations of only the capillary itself. The difference between these two simulations is resolution since one surface consists of four concentric rings with 90 facets each, sketched in Figure 4.10, while the other has ten rings. The third simulation follows an analogue scheme but with only a single facet so it has also recorded Monte Carlo data but ignores spatial dependence. Fourth simulation is the explicitly modelled capillary, used as reference.

Results of these simulations are shown in Figure 4.14. Profile on the target impinged by the finer segmented surface agrees very well with the result for the explicitly simulated capillary,

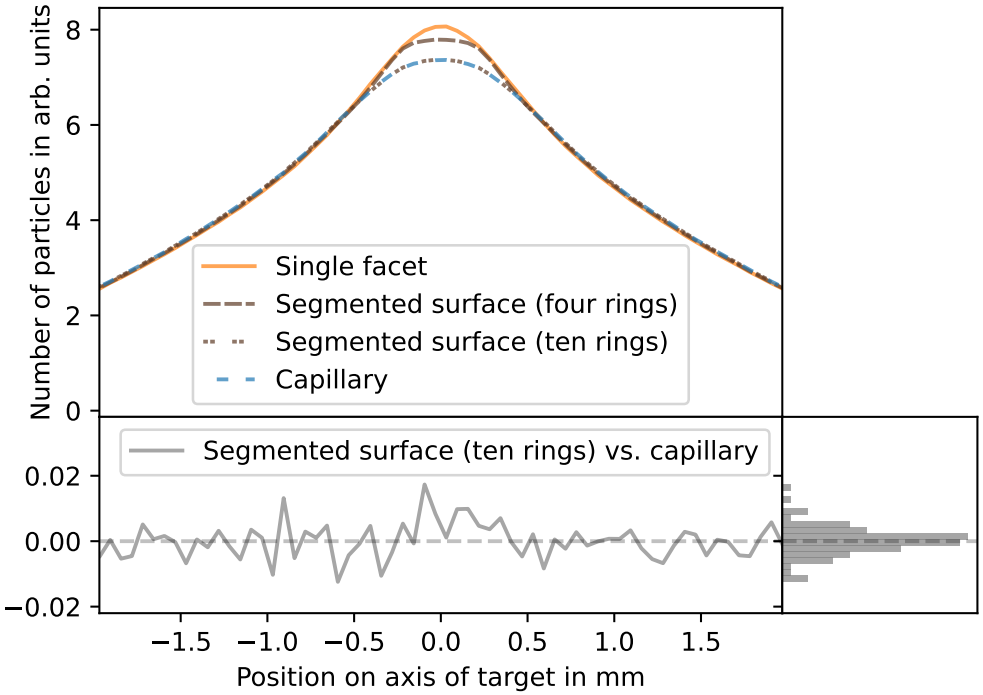

Figure 4.14.: **Beam shape for different implementations of a capillary** Profiles of particle hits on a target surface are shown. They are impinged by same number of particles from a distance of $z = 5\,\mathrm{mm}$ by differently implemented capillaries with a reduced effective length of $l_{\mathrm{eff}} = 8$ and a diameter of $D = 0.5\,\mathrm{mm}$, so setup is as shown in Figure 4.12. Residuals show the difference between a segmented surface imitating capillary as described in subsection 4.1.3 and an explicitly simulated capillary.

deviation is dominated by statistical fluctuations and is less than $0.1\,\%$, residuals are shown in the plot. For a single homogeneous facet as particle source, there is a significant discrepancy from the capillary of about $10\,\%$, rate at the centre is higher. As expected, hit count for the coarser segmented surface with four rings lies in-between single facet and finely resolved segmented surface, deviation is about $6\,\%$.

All tested capillary surfaces overestimate number of hits near target centre even though they do not respect sufficiently that more particles are emitted from centre of capillary outlet. Apparently, the dominating reason is angular distribution near the edge being more steep and focussed in outward direction, as was seen in Figure 4.9 and Figure 4.11b. In case of a single facet as source, as many particles are emitted from the edge towards centre than outwards, resulting in overestimated intensity there.

Deviation between implementations is seen to be mostly constrained to about the size of capillary outlet since this is the scale on which spatial variations of emission behaviour matters. In Figure 4.14, target was placed in a distance of $z = 10D = 5\,\mathrm{mm}$. At larger distances, beam shape depends less and less on structure of the outlet as its size vanishes in comparison. Thus, results converge further away from capillary, deviation is less than $1\,\%$ at $z = 10\,\mathrm{cm}$.

In this section, an analytical model by Tschersich is implemented in Molflow. Polar and azimuthal angular distribution and the density on the outlet are sampled spatially resolved for varying effective lengths of the beam forming section, with particles entering it with a cosine or uniform angular distribution. The produced data enables an investigation of beam forming in the capillary which reveals a gradual collimation along the capillary and that the beam is more focussed into outward direction the closer to the edge of the outlet it is emitted. This analysis could be a starting point of expanding to a full simulation of a capillary over its total length, including particle–particle interactions and a temperature gradient along its surface.

From comparison with the Molflow simulation, the angular distribution by Tschersich was found to only hold in the far-field. There, good agreement is observed. A way was presented to mimic the emittance behaviour of a capillary in Molflow without repeatedly simulating it explicitly. This is required to simulate the further propagation of atoms through the experimental setup accurately and efficiently. The presented methods of using segmented surfaces and benchmarking them will reappear in the following section as well.

4.2. Transport and shaping of the atomic beam in a skimmer setup

The atomic beam leaves the capillary with a specific spatially resolved density and angular distribution, as described in section 4.1. Both have an impact on the further progression of the beam so it is mandatory to take advantage of the full beam profile properties when describing its propagation through the subsequent part of the system which is a beam shaping section. This subsystem prepares the beam for entering the ToF setup as the beam was found to be significantly divergent. Without additional beam collimation, this would result in excessive scattering. The

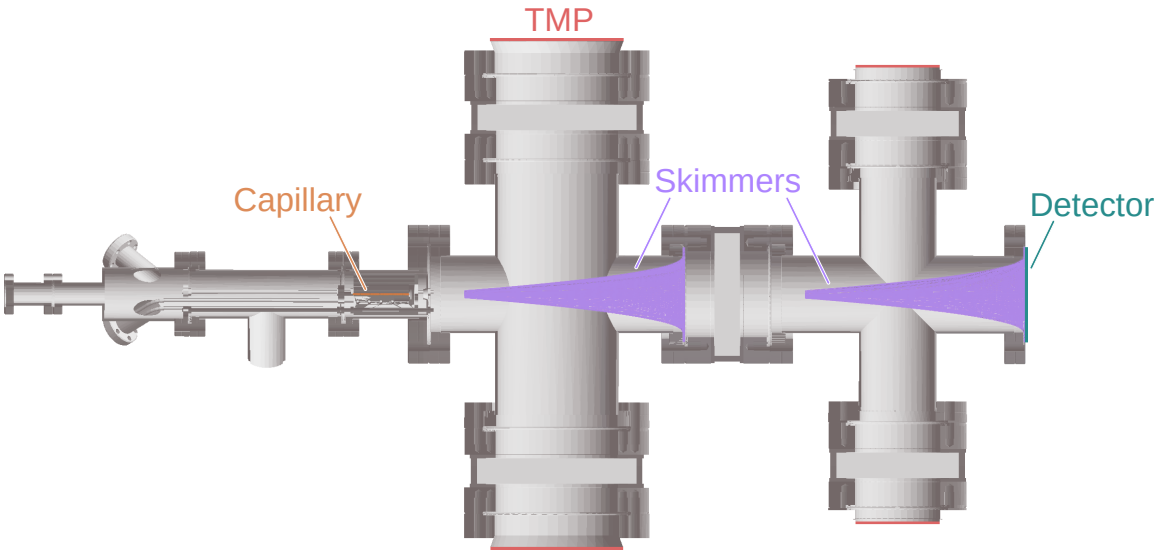

Figure 4.15.: **CAD model of AHS 1.5** Cross section through the central plane of the experimental setup of AHS 1.5. Particle trajectories are simulated with Molflow from the capillary in the left to the outlet on the right, called detector here. The beam is focussed by skimmers, particles hitting turbomolecular pumps (TMPs) have a specific chance of being pumped.

necessary focussing is achieved by cutting too strongly diverging particles by skimmers and pumping them out. In this section, a modified version of an existing atomic hydrogen source (AHS) at the Tritium Laboratory Karlsruhe is used as a specific example for beam shaping.

4.2.1. Simulation of particles in the experimental setup of AHS 1.5

The considered system is similar to the experiment AHS 1.5, built in 2023 at the Tritium Laboratory Karlsruhe at KIT, see a CAD model in Figure 4.15. In this version, its central part consists of two 4-way crosses. The particle source is attached at one end so that the emitted beam crosses the entire setup. On the opposite end, it reaches the transition to the ToF setup which will be covered in section 4.3. Within this section, the virtual surface separating skimmer setup and ToF setup is referred to as a detector surface. On each cross, two turbomolecular pumps (TMPs) specialised for light gases are attached, namely two Pfeiffer HiPace 350 pumps with a pumping speed of $300\,\mathrm{L\,s^{-1}}$ for H_2 at the first cross with CF 100 flange and two Pfeiffer HiPace 80 pumps with a pumping speed of $48\,\mathrm{L\,s^{-1}}$ for H_2 at the second cross with CF 63 flange.

Skimmers are attached at copper gaskets at the crosses along main flight direction of the atomic beam, as indicated in purple in Figure 4.15. The specific skimmer design used in this simulation was devised by Johannes Wörner in his bachelor's thesis [2]. He found that while a single simple pinhole skimmer already improves the ratio of atoms to molecules considerably, a combination of two parabolic skimmers is clearly superior. The parabolic outer shape is assumed to effectively

[2] Johannes Wörner. "Entwicklung eines Skimmers zur Strahlformung einer atomaren Wasserstoffquelle". Bachelor's thesis. Karlsruhe: KIT, Aug. 30, 2023.

deflect particles towards the TMPs, slightly better than a cone-shaped skimmer. Height of both skimmers is to be chosen as high as possible. A diameter of the first skimmer's opening of $5.5\,\mathrm{mm}$ yields an optimal combination of high throughput and atomic fraction. The diameter of the second skimmer D_S is suggested to be chosen according to the requirements of the respective experiment, with smaller diameters resulting in a more narrow beam and higher atomic fraction but at the expense of lower throughput. In this work, diameters of $4\,\mathrm{mm}$, $6\,\mathrm{mm}$ and $8\,\mathrm{mm}$ are investigated.

The Molflow simulation is already prepared by Wörner. An existing CAD model of the AHS 1.5 is edited in an external program. The leak test grooves are closed to prevent leaks and all parts without contact to the interior are removed. CAD models of differently sized skimmers are created with an external program. The experimental setup and a skimmer are imported to the Molflow simulation. TMPs are modelled as absorbing surfaces, a capillary is added as a desorbing facet and a detector is added as an absorbing facet recording impinging particles. Pressure is assumed sufficiently small for this and all further systems in this work to be in molecular flow regime, so using software like Molflow is justified.

The simulation prepared by Wörner is refined in two respects. Firstly, TMPs have previously been assumed ideal with a sticking factor of 1, which means they were modelled to absorb all particles hitting the pumping surfaces. This was equivalent to a pumping speed of about $8200\,\mathrm{L\,s^{-1}}$ at CF 100 and $3300\,\mathrm{L\,s^{-1}}$ at CF 63 for particles with an atomic mass of $2\,\mathrm{u}$, representing H_2, see section 3.4 and section 3.3. This is adjusted to the pumping speeds given before in this section, which results in sticking factors of $3.6\,\%$ and $1.5\,\%$. These shares are assumed to be more realistic since the effectively pumped area of a TMP is smaller than flange diameter suggests as the hub in the centre can not pump. Also, not all particles hitting the first layer of rotors will be pumped out. Pumping speed is adapted for molecular hydrogen even though it is different for atomic hydrogen. However, atoms have a high chance to recombine when they any surface, so most particles reaching a pump will be molecules.

Secondly, both the capillary and the detector are modelled as segmented surfaces instead of homogeneous. The method is described in subsection 4.1.3 for the capillary which gathers angular distribution and number of impinging particles separately on 90 facets on each of its ten rings, except the innermost ring which consists of only one facet. The identical CAD model is used in this simulation, the recorded information about beam shape is processed as also described in subsection 4.1.3. Analogous to that, the method is also used to record particles reaching the detector surface. Due to much lower available statistics, the surface is split into only 47 segments on four rings each, again except the innermost one. A quickly available profile of hits on the detector is used to estimate sensible ring diameters which allows these rings to properly resemble gradients in beam intensity.

For the setup of $D_\mathrm{S} = 6\,\mathrm{mm}$, $2.7 \cdot 10^7\,\mathrm{particles}$ have been simulated. About $0.39\,\%$ of these were absorbed at the detector, so data of about $1.1 \cdot 10^5\,\mathrm{particles}$ was collected. The remaining particles were pumped out. The share of particles arriving at the detector depends strongly on skimmer diameter, see also subsection 4.2.2. All particles together hit walls about $3.3 \cdot 10^{10}\,\mathrm{times}$. Running on ten cores, about $1.8 \cdot 10^5\,\mathrm{hits/s}$ are calculated, which resulted in a calculation time of about two days. As slightly reduced statistics is supposed to suffice, calculation time is between one and two days for any considered skimmer diameter.

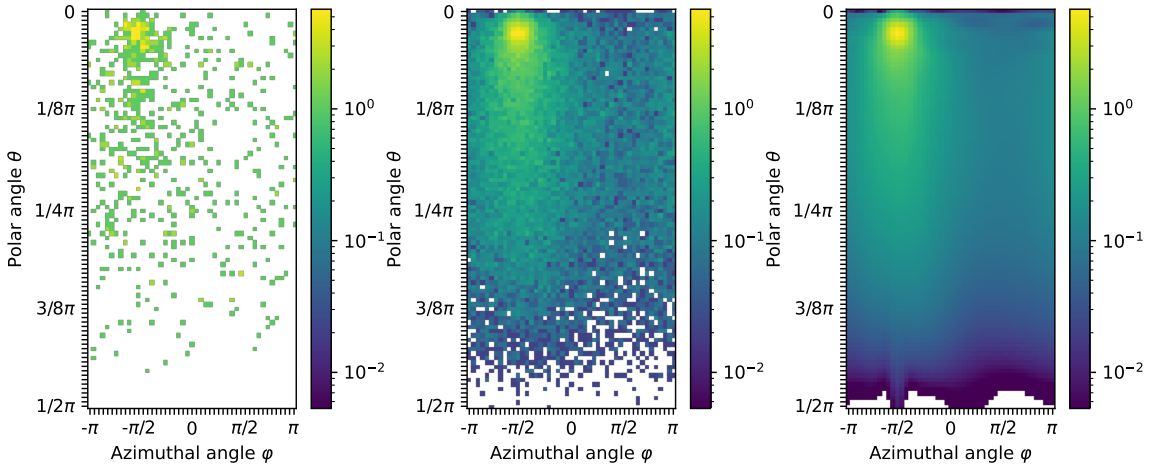

(a) Single segment.

(b) All segments of ring 3 averaged.

(c) Smoothed average.

Figure 4.16.: **Processing of the angular distribution on a segmented detector surface** Polar and azimuthal angular distribution, processed from raw simulated data to being usable as inlet in the simulation of the ToF setup. Colour indicates the number of particles with respective angles θ and φ, so these distributions are not corrected for volume. The figures show the angular distribution for a skimmer diameter $D_\mathrm{S} = 6\,\mathrm{mm}$ on the third of four rings. Maximum intensity is shifted to $\varphi = -\pi/2$ since reference axis is rotated by $90°$ relative to Figure 4.11.

4.2.2. Shape and profile of the atomic beam after focussing

The significance of simulations up to the detector surface at the transition to ToF setup is mainly to record beam profile and shape. Profiles are shown in Figure 4.17a, they are one-dimensional and directly extracted by Molflow's *profile plotter* feature. In contrast, angular distributions such as in Figure 4.16 are described by polar angle θ and azimuthal angle φ and they are different at each ring of the segmented surface. For the purpose of visualisation of the produced beam, a separate simulation is run in which a copy of the modelled detector surface emits particles onto a target. The profile on this target surface is shown in Figure 4.17b. This is the same method as used in subsection 4.1.4 for benchmarking different implementations of capillaries.

Total number of particles arriving at the detector increases for growing skimmer opening area $\pi D_\mathrm{S}^2/4$ but less than linearly since the beam is already slightly focussed when it arrives at the second skimmer. The ratios are $0.19\,\%$, $0.39\,\%$ and $0.65\,\%$ for skimmer diameters D_S of $4\,\mathrm{mm}$, $6\,\mathrm{mm}$ and $8\,\mathrm{mm}$ respectively. The profiles consist of a central narrowly focussed part and a broader background of scattered particles. The widths of these focussed parts are about $7\,\mathrm{mm}$, $10\,\mathrm{mm}$ and $13\,\mathrm{mm}$. For comparison, without skimmers $47\,\%$ of atoms arrive at the detector and the intensity over its surface is roughly constant.

When all curves in Figure 4.17a are normalised to the same number of arriving particles (not shown here), centre intensity for smaller skimmer diameters surpasses that for larger openings. In contrast, scattered background is identical for all skimmer diameters considered here.

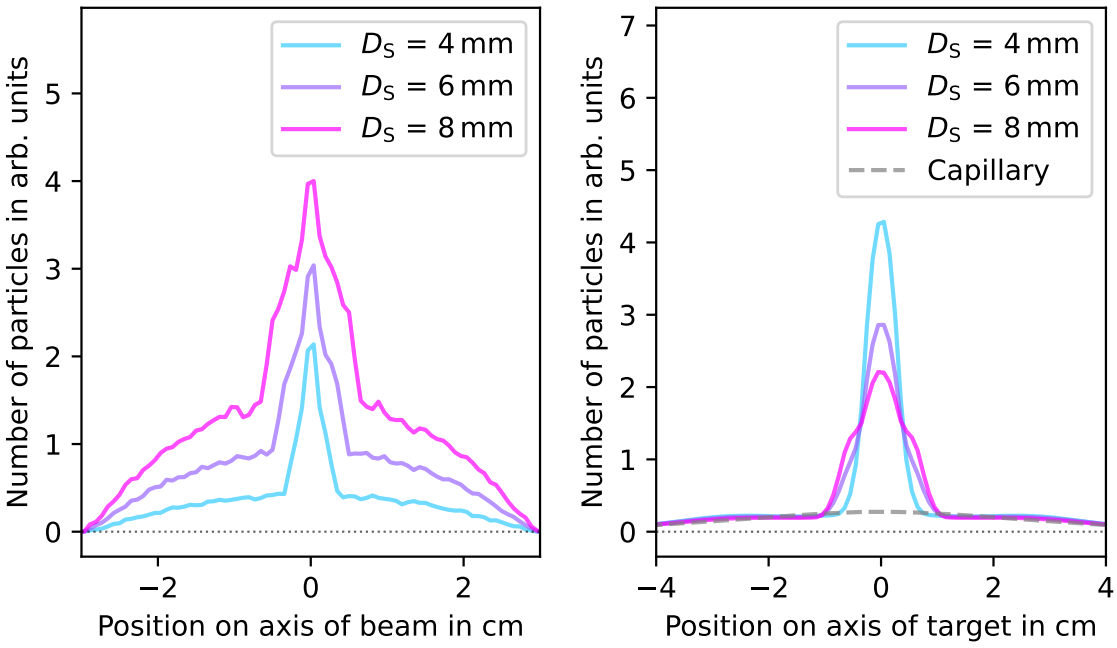

(a) Beam profiles on detector.

(b) Impingement profiles on target by beam.

Figure 4.17.: **Beam shape for different skimmer diameters** The left plot shows the profile of the atomic beam at the detector surface for different diameters D_S of the second skimmer's opening. The curves are shown for same number of particles emitted from the capillary into the skimmer setup. The right plot shows the central part of a profile on a target surface. It is impinged from a distance of $z = 20\,\mathrm{cm}$ by particles emitted from a segmented surface resembling closely the detector. Same number of particles is emitted for each curve. For comparison, the profile created from particles emitted by a capillary with a reduced length of $l_{\mathrm{eff}} = 8$ and inner diameter of $D = 0.5\,\mathrm{mm}$ is shown.

This is also seen from the benchmarking simulation in Figure 4.17b where recorded angular distribution of the beam is considered in addition to density gradient. All those particles will contribute to scattering in the ToF setup which hit the target outside the centre by more than a specific distance which depends on ToF tube length L and diameter D. As density profiles outside the central part do not depend significantly on skimmer diameter D_{S}, this means that a large opening can be chosen without increasing unfavourable scattering, harnessing higher statistics, as long as no parts of the central beam hit the walls. However, a more focussed beam might still be desirable in an experiment as the mass spectrometer will not cover the entire cross section of the tube.

In conclusion, skimmers effectively filter divergent particles of the atomic beam and prevent them from reaching the detector surface at the transition to the ToF setup. The smaller the skimmer diameter D_{S}, the more narrow is the atomic beam but at the cost of reduced intensity, also near beam centre. The remaining atoms with large polar angles θ scatter in the next subsystem. Compared to a setup without skimmers or to a capillary attached directly to a ToF tube, scattering in the ToF setup is reduced drastically. This is essential for accurate ToF measurements.

4.3. Measurements in a time-of-flight setup

When a parallel atomic beam crosses a tube of known length, its ToF distribution is readily calculated from known temperature or velocity distribution. However, it was found in section 4.2 that a realistic beam includes a significant number of divergent atoms which scatter on the surface of the ToF tube. The resulting distortion of the ToF distribution is illustrated by analytical models in subsection 4.3.1. To employ the more realistic assumptions of diffuse scattering and thermalisation, a simulation is conducted in subsection 4.3.2 using Molflow. The simulation yields the individual ToF distribution of atoms. This is convoluted with the transfer function of a rotary shutter, determined in subsection 4.3.3, to calculate in subsection 4.3.4 the ToF distribution as measured in an experiment.

4.3.1. Time-of-flight distribution from analytical models

It requires only an arbitrary velocity distribution, such as a Maxwell-Boltzmann distribution, to calculate the ToF distribution of particles travelling a certain distance in parallel. For specular scattering, the calculation requires in addition the angular distribution of the entering beam. Further, a model for qualitative discussion of the effects of diffuse scattering is offered.

Analytical description of particles flying in parallel

All particles parallel to the axis of the ToF tube travel the exact same distance until being detected, namely the length L of the tube. For a known velocity distribution $P_v(v)$, the corresponding ToF distribution $P_t(t)$ can be directly calculated by Equation 4.4.

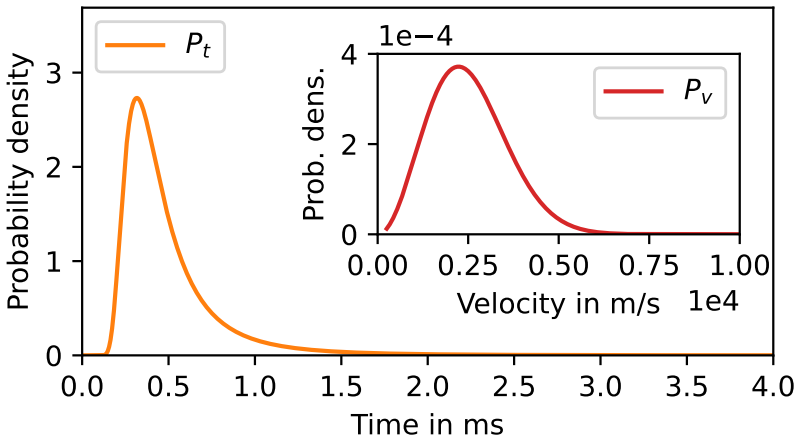

Figure 4.18.: **Time-of-flight distribution of a parallel particle beam** The inset shows the Maxwell-Boltzmann distribution of particles with a temperature of $300\,\mathrm{K}$ and an atomic mass of $1\,\mathrm{u}$. From this, the shown ToF distribution is calculated for a parallel beam travelling $1\,\mathrm{m}$.

$$P_t(t) = P_v(L/t)\,L/t^2 \qquad \text{from [Coo+20]} \tag{4.4}$$

$$P_v^{\mathrm{MB},\,T}(v) = \sqrt{\frac{2}{\pi}}\frac{1}{a^3}\,v^2 \exp\left(-\frac{v^2}{2a^2}\right) \quad \text{with } a = \sqrt{k_\mathrm{B}T/m} \qquad \text{from [TM19]} \tag{4.5}$$

$$P_v^{\mathrm{MB},\,(T_1,u_2,T_2,\dots)}(v) = \left(P_v^{\mathrm{MB},\,T_1}(v) + u_2 \cdot P_v^{\mathrm{MB},\,T_2}(v) + \cdots\right) / \left(1 + u_2 + \cdots\right) \tag{4.6}$$

In the simplest case, velocity distribution is a Maxwell-Boltzmann distribution which takes temperature T as the only parameter apart from known atomic mass m, see Equation 4.5 and Figure 4.18. This is readily extended to a superposition of Maxwell-Boltzmann distributions, see Equation 4.6. However, this introduces two additional parameters for each additional distribution, namely temperature T_i and a factor for relative weight u_i. Retrieving an arbitrary velocity distribution would require a different approach than currently implemented. In this work, it is assumed that the velocity distribution of atoms in the beam is always given by a single Maxwell-Boltzmann distribution.

Analytical description of specularly scattered particles

In case of a non-parallel beam, particles will hit walls of the ToF tube and scatter. In this subsection, specular scattering is assumed. Neither velocity v nor polar angle θ between particle trajectory and tube axis change at reflection, so total path length $L(\theta)$ of a particle in the tube increases by $1/\cos(\theta)$, see Equation 4.7. ToF distribution $P_t(t,\theta)$ of all particles inclined to the axis by angle θ is then given by Equation 4.8 which is the same as Equation 4.4 but with modified length. Equivalently, length L could be kept fixed and the velocity component $v_z = v\,\cos(\theta)$ considered.

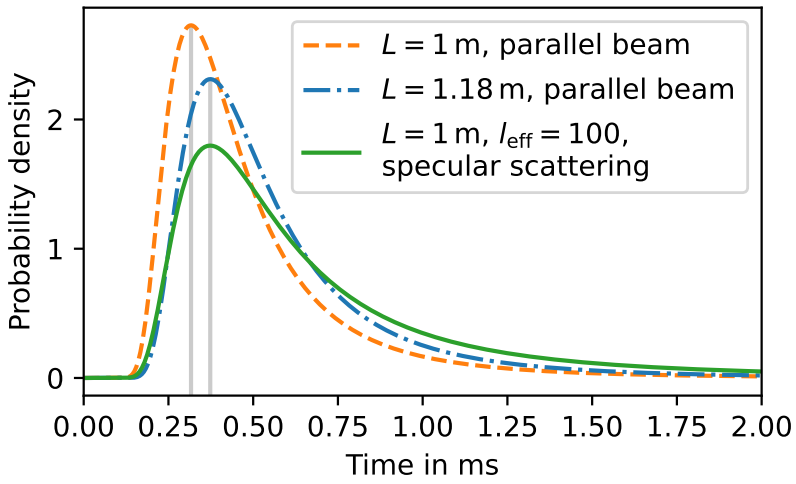

Figure 4.19.: **Time-of-flight distribution of a specularly scattered particle beam** The orange dashed curve is the same as in Figure 4.18. A divergent beam as emitted from a capillary with effective length $l_{\text{eff}} = 100$ results in the green solid curve when assuming specular scattering. Its maximum occurs at the same time as ToF distribution of a parallel beam in a longer tube with approximately $L = 1.2\,\text{m}$, see blue dash-dotted curve.

To yield total ToF distribution $P_t(t)$, contributions of $P_t(t, \theta)$ from all angles θ are summed up. They are weighted by known angular distribution $j(\theta)$ from Tschersich, which gives the share of particles emitted for each angle θ, see subsection 4.1.1. So here the assumption is applied to this model that the ToF setup is directly connected to the capillary. Distribution $j(\theta)$ in volume needs to be corrected to total number of emitted particles by multiplying with $\sin(\theta)$, see subsection 4.1.2. Eventually, $P_t(t)$ is given by Equation 4.9.

$$L(\theta) = L/\cos(\theta) \tag{4.7}$$

$$P_t(t, \theta) = P_v(L(\theta)/t)\, L(\theta)/t^2 \tag{4.8}$$

$$P_t(t) = \int_0^{\pi/2} j(\theta)\, \sin(\theta)\, P_t(t, \theta)\ \mathrm{d}\theta \tag{4.9}$$

As compared to the ToF distribution of a parallel beam travelling through the same tube, the maximum occurs at a later time, see Figure 4.19. This is expected from longer flight distance. However, the late arrival of particles with large inclination θ causes a long tail which is not observed for parallel beams. Thus, a share of specularly scattered particles is expected to show up in measurements as a slightly broadened distribution as compared to particles flying in parallel.

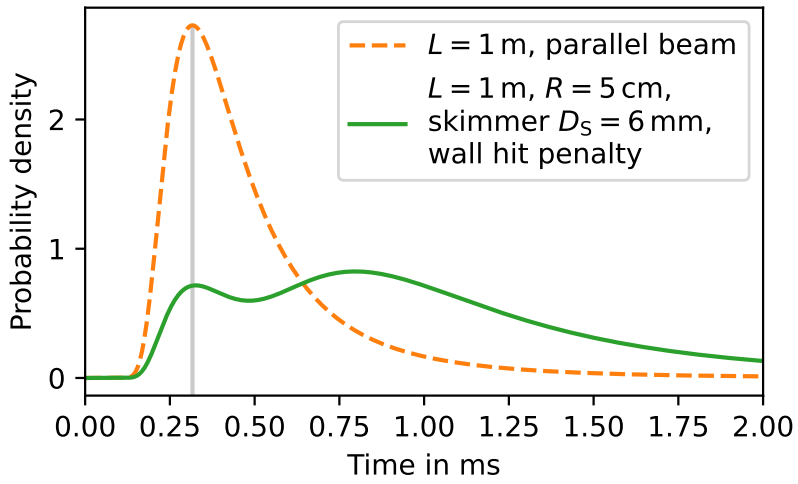

Figure 4.20.: **Model of the time-of-flight distribution of a diffusely scattered particle beam** Orange dashed curve is the same as in Figure 4.18. Green solid curve results from a model of increased path length of a particle after it first hits a wall. It is calculated with the angular distribution recorded at the detector surface for a second skimmer diameter of $D_\mathrm{S} = 6\,\mathrm{mm}$. Diameter of the tube is $D = 10\,\mathrm{cm}$.

Analytical description of diffusely scattered particles

As mentioned in section 3.2, particles are supposed to scatter mainly diffusely, which means with a cosine-distribution. Such behaviour is very complicated to calculate analytically, so a much simplified model is considered here before doing more realistically in subsection 4.3.2. A particle hits the wall for the first time after a distance of L_x when the inlet is assumed to be point-shaped, see Equation 4.10 with R the radius of the tube. The particle then scatters back and forth until it reaches the end of pipe at position L. The main assumption of this model is that effective path length of the particle travelling from L_x to L is by a factor k longer than direct distance $L - L_\mathrm{x}$, see Equation 4.11. This scaling is chosen constant for simplicity and a factor $k = 3$ is chosen arbitrarily.

$$L_\mathrm{x}(\theta) = \begin{cases} R/\tan(\theta)\,, & \text{if } (R/\tan(\theta)) \leq L \\ L\,, & \text{otherwise} \end{cases} \tag{4.10}$$

$$L(\theta) = L_\mathrm{x}(\theta) + k \cdot (L - L_\mathrm{x}(\theta)) \tag{4.11}$$

Figure 4.20 shows this model applied to the angular distribution calculated in subsection 4.2.2. The resulting green solid ToF distribution is seen to consist of two parts. Firstly, particles almost parallel to tube axis arrive at the same time as a purely parallel beam which is again shown as orange dashed curve. Secondly, scattered particles are delayed and produce another maximum in the distribution that afterwards falls off slowly. These observations will later be utilised in

subsection 5.1.2 when ToF distributions obtained from simulations are described phenomenologically.

4.3.2. Time-of-flight distribution from Monte Carlo simulations

In order to stay closer to physically motivated assumptions that can not be respected by simple models, MC simulations are performed. This section describes how these simulations are set up in Molflow and how ToF distributions are extracted after running them.

Modelling particle propagation in Molflow

The propagation of particles in a ToF setup is simulated using Molflow. The ToF tube is modelled as a cylinder of variable length L and diameter D. In this work, these design parameters are often chosen as $L = 1\,\mathrm{m}$ and $D = 10\,\mathrm{cm}$. The walls of the tube are fixed at a temperature of $T = 300\,\mathrm{K}$. The particle source is a segmented surface identical to the detector of the skimmer setup simulation from subsection 4.2.1, so the outlet of that prior simulation is used as inlet of this simulation, see Figure 4.1. When arriving at the opposite side of the tube, particles are detected on the outlet surface which spans over the entire cross section. Extensive information about these impingements is collected by Molflow's *particle logger* feature.

Particle mass is adjustable and chosen as $1\,\mathrm{u}$, representing hydrogen atoms, as the share of molecules in the atomic beam is small after having passed the skimmers [3]. Recombination of atoms at surfaces is not considered. The source emits particles with adjustable beam temperature and the beam shape determined in subsection 4.2.2. For testing and benchmarking reasons, the angular distribution can also be set to a function of easily adjustable divergence, such as $\cos^n$ or the distribution of Tschersich introduced in subsection 4.1.1 with varying effective capillary length l_{eff}.

This is the first simulation in this work in which flight time of particles is measured. Therefore, realistic values need to be assigned for accommodation coefficient A_{Acc} and sojourn time τ. Both quantities are discussed in section 3.2. Accommodation coefficient which describes the degree of thermalisation at walls is set to $A_{\mathrm{Acc}} = 0.09$ [Ler+97]. This value is measured by chemical vapour deposition for hydrogen molecules on stainless steel. It might not be applicable for hydrogen atoms and the conditions inside the ToF tube regarding temperature and pressure.

Assuming physisorption, the sticking time τ of hydrogen atoms on steel at $300\,\mathrm{K}$ follows from Equation 3.7. Assuming a typical binding energy like that for hydrogen molecules of $65\,\mathrm{meV}$, sojourn time is $\mathcal{O}(1\,\mathrm{ps})$ [Ben99; Bag07] while ToF measurements typically take place at least at $\mathcal{O}(100\,\mu\mathrm{s})$. Since the number of hits in the tube usually only rarely exceeds about 1000, this adds up to a total sojourn time of $\mathcal{O}(1\,\mathrm{ns})$ which is several orders of magnitude lower than flight time. Thus, sticking time of particles by physisorption is negligible and not considered in the Molflow simulation. Below temperatures of about $77\,\mathrm{K}$, sticking time starts to be relevant with

[3] Johannes Wörner. "Entwicklung eines Skimmers zur Strahlformung einer atomaren Wasserstoffquelle". Bachelor's thesis. Karlsruhe: KIT, Aug. 30, 2023.

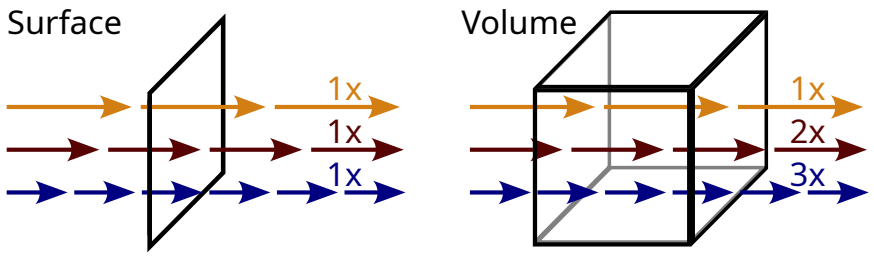

Figure 4.21.: **Measuring quantities on a surface and in volume** Particles of different velocities are emitted at constant time intervals. Measurements on a surface at the same frequency will each time detect one of each particles. In contrast, in volume a higher number of slow particles (blue) is detected than fast ones (orange).

total sojourn times of $O(1\,\mu s)$. However, walls of the ToF setup will always be close to room temperature, so this is not relevant for the experiment as currently planned.

Hydrogen atoms H tend to be chemisorbed on surfaces [Chr88]. With a binding energy of $270\,\mathrm{kJ\,mol^{-1}}$ on iron, this results at room temperature in virtually unlimited sticking time. Adsorbed hydrogen layers in the ToF setup might cause an increased background of detected particles. Such background will exist anyway due to thermal transpiration. However, including very long sticking times in the Molflow simulation would not provide any benefit.

Extracting a time-of-flight distribution from simulated particles

From logged data of particles having crossed the tube, relevant for this analysis are time of arrival t and corresponding velocity v_{QMS} at the outlet surface for each particle. Most often in this work, 10^6 particles are logged which takes a few seconds of calculation time and about $110\,\mathrm{MiB}$ of disk space.

Velocity information is required to extract a ToF distribution in volume. This is different from measuring on a surface since slow particles stay in a specific volume for a longer time and are therefore weighted more strongly. This effect is visualised in Figure 4.21.

Creating a histogram from logged arrival times t represents ToF distribution on a surface P_t^{Surf} since particle data was also logged when arriving on the outlet surface. In contrast, a distribution in volume P_t^{Vol} is yielded by scaling with stay time t_{QMS} in the detection volume. So when creating the histogram, arrival time t of each particle is separately weighted with its corresponding reciprocal velocity v_{QMS}, see Equation 4.12. An example of a ToF distribution retrieved this way is seen in the first plot of Figure 4.24.

$$t_{\mathrm{QMS}} \sim 1/v_{\mathrm{QMS}} \tag{4.12}$$

Conversion after creating surface histogram P_t^{Surf} and without separate knowledge of velocity v_{QMS} is only possible for a parallel beam. That is because it takes all particles in the same bin of the histogram the same time t to arrive at the outlet and they all travel the same distance,

namely the length L of the ToF tube. Therefore, they have the same velocity $v = L/t$ which is also constant as no scattering at walls of the tube occurs, see Equation 4.13. So velocity v_{QMS} near detector is directly known from arrival time t, therefore Equation 4.14 holds. Integral in the denominator is for normalisation.

$$v_{\mathrm{QMS}} = v\,, \text{ so } t_{\mathrm{QMS}} \sim t \qquad \text{for a parallel beam} \tag{4.13}$$

$$P_t^{\mathrm{Vol}}(t) = \frac{P_t^{\mathrm{Surf}}(t) \cdot t}{\int \left(P_t^{\mathrm{Surf}}(t') \cdot t'\right) \mathrm{d}t'} \qquad \text{for a parallel beam} \tag{4.14}$$

Unless stated differently, P_t will always refer to P_t^{Vol} in the following.

The yielded ToF distribution is interpolated since applying a convolution later in subsection 4.3.4 requires a smooth curve. This is often not fulfilled at steep slopes or would require a very large number of bins, causing high fluctuations due to limited amount of data. For interpolation, the *Piecewise Cubic Hermite Interpolating Polynomial* (PCHIP) algorithm[4] is chosen. This kind of piecewise cubic interpolation is shape-preserving so no artefacts by overshooting occur which is especially critical near $t = 0$ where the distribution is zero until it starts to rise steeply.

4.3.3. Modelling the transfer function of a rotary shutter

A rotary shutter is required near the entrance of the ToF setup, as described in section 3.4. Its impact on the measured ToF distribution will be calculated in the following subsection 4.3.4. First, a quantity called the transfer function needs to be determined. It describes the share of beam particles which can pass the rotary shutter at a specific moment in time. Thus, it describes a transmissibility and its value is always between 0 and 1, see as an example the orange solid curve in Figure 4.23.

An analytical description of the rotary shutter by calculating the transfer function and considering its impact on the ToF distribution is chosen to be preferred over including an explicit model of the shutter in the Molflow simulation. This way, its geometry can be changed directly in the Python script without rerunning any Molflow simulations, making changes of design parameters much faster and applicable in batches.

If desired, the shutter could later still be included explicitly. However, this is not easy since Molflow does not support moving elements. It could approximately be implemented by running a time-dependant simulation, splitting the shutter radially into many slices and use a script to assign a time-dependent opacity to these slices such that a transparent section of desired width rotates at desired frequency. As anticipated for experimental implementation, the shutter would be placed in a widened compartment such that its opening was aligned with the beam which propagates along the central axis of the ToF tube.

[4] Information about the used implementation in *scipy* (used version: 1.10.0) as well as references at: `https://docs.scipy.org/doc/scipy/reference/generated/scipy.interpolate.PchipInterpolator.html`.

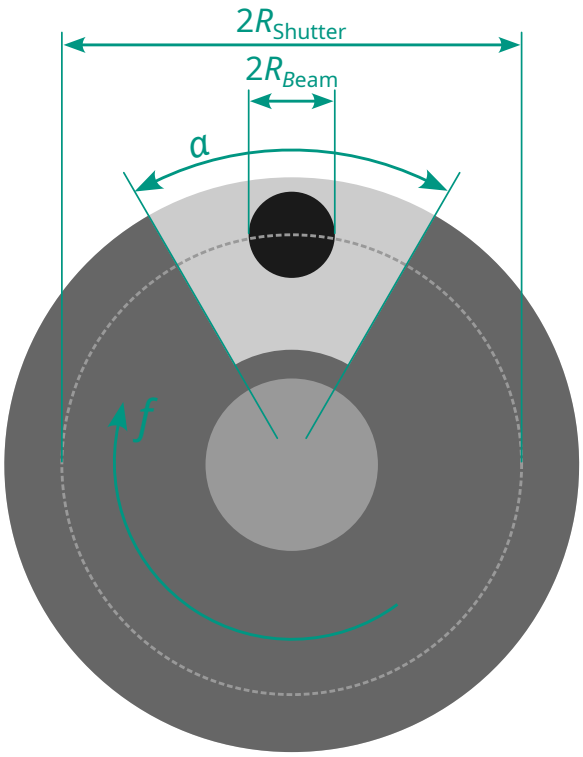

Figure 4.22.: **Geometry of a rotary shutter** A rotary shutter is described by the marked design parameters shutter radius R_{Shutter}, opening angle α and rotation frequency f. Additionally, it can have multiple openings. To determine the shutter's transfer function, the potentially inhomogeneous profile of the passing atomic beam needs to be known. In the simplest case, it is assumed homogeneous with beam radius R_{Beam}.

The calculation of the transfer function $h(t)$ consists of calculating the window function $w(t)$ and then considering its distortion by the profile of the atomic beam $b_x(x)$.

Calculating the window function of a rotary shutter from geometry

For neglectable size of the atomic beam, window function $w(t)$ is equal to transfer function $h(t)$, see Equation 4.15, with $\delta(x)$ the Dirac delta function. Its shape is determined from the geometry of a rotary shutter, see a sketch in Figure 4.22. Assume the beam to be fixed in its uppermost position while the shutter rotates. Transmissibility is 1 while the beam passes through the opening and 0 otherwise. Time of opened shutter is derived directly from time for one rotation T_0 and ratio of opening angle α and full circumference. This repeats periodically, see Equation 4.16. An example for $f = 500\,\text{Hz}$ and $\alpha = 42°$ is the blue dash-dotted curve in Figure 4.23.

$$h(t) = w(t) \qquad \text{for } b_x(x) = \delta(x) \tag{4.15}$$

$$w(t) = \begin{cases} 1\,, & \text{if } (t \% T_0) < \alpha/360° \cdot T_0 \\ 0\,, & \text{otherwise} \end{cases} \qquad \text{with } T_0 = 1/f \tag{4.16}$$

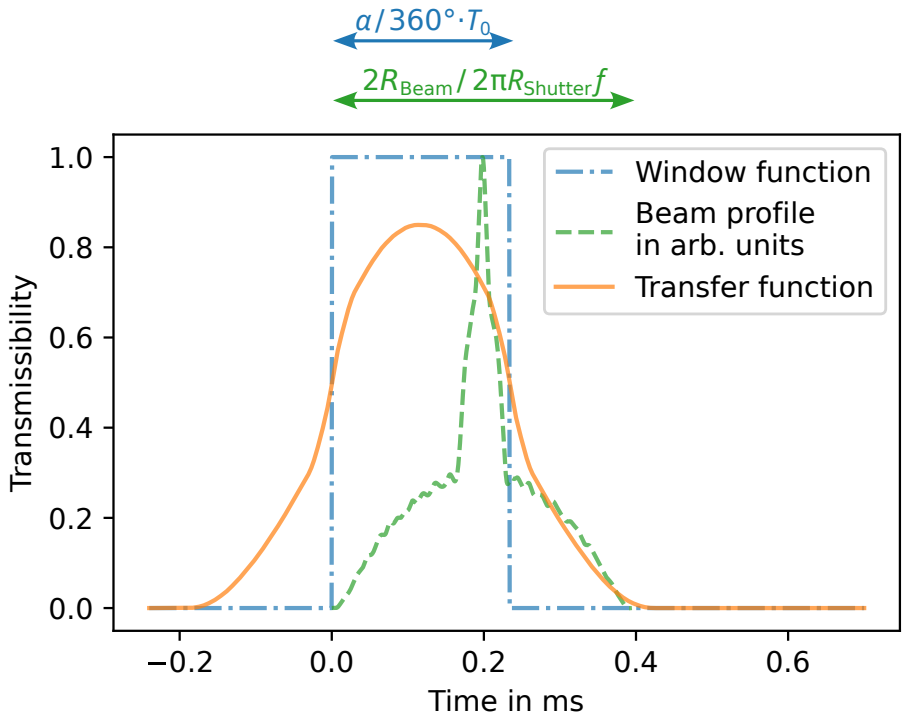

Figure 4.23.: **Distortion of a transfer function by beam profile** The profile of an atomic beam $b_t(t)$ is shown in time-domain in normalised number of hits. It is recorded behind the second skimmer of AHS 1.5 with diameter $D_S = 6\,\mathrm{mm}$, so it is the same as in Figure 4.17a. Window function $w(t)$ and transfer function $h(t)$ describe a transmissibility of particles. The transfer function is calculated as convolution of window function and beam profile, its integral is kept equal to that of the window function.

In case of multiple evenly spaced openings, they can be considered without adapting the implemented functions but by renormalising the other parameters. To this end, the parameters rotation frequency f, shutter radius R_{Shutter} and beam radius R_{Beam} are multiplied with the number n of openings.

Distortion of a transfer function by beam profile

Unless the beam is neglectably narrow, its profile $b_x(x)$ needs to be considered in describing the transfer function of the rotary shutter. As a simple and analytical approximation, the beam can be considered homogeneous, in which case its profile is given by double the value of a semi-circle function, as shown in Equation 4.17.

However, the beam profile is known from a simulation of the vacuum setup by Molflow using its *profile plotter* feature, see subsection 4.2.2. It describes the total number of particles hitting the detector surface along an axis through its center, see subsection 4.1.4 for more details. A profile $b_x(x)$ is converted to time-domain $b_t(t)$ by linear scaling with the known reciprocal path

velocity $2\pi R_{\text{Shutter}} f$, see Equation 4.18. This way, it effectively describes the detected number of particles over time when scanning the beam using a rotary shutter with a very narrow opening.

$$b_x^{\text{Circle}}(x) = \begin{cases} 2\sqrt{1 - \left(\frac{x - R_{\text{Beam}}}{R_{\text{Beam}}}\right)^2}, & \text{if } x = 0 \dots 2R_{\text{Beam}} \\ 0, & \text{otherwise} \end{cases} \tag{4.17}$$

$$b_t(t) \sim b_x(2\pi R_{\text{Shutter}} \cdot t/T_0) \tag{4.18}$$

As a specific example see the beam profile in Figure 4.23. Profiles returned by Molflow always consist of 100 data points, labelled 0 to 99. Spatially, this profile $b_x(x)$ describes the detector in a range from $-3.9\,\text{cm}$ to $3.9\,\text{cm}$. In time-domain $b_t(t)$, this turns into $0\,\text{ms}$ to $0.39\,\text{ms}$ for a shutter radius of $R_{\text{Shutter}} = 10\,\text{cm}$ and a rotation frequency of $f = 500\,\text{Hz}$. The alignment with $t = 0$ was chosen arbitrarily here, for details see subsection 4.3.4.

The profile $b_t(t)$ is shown here with a maximum value of 1. However, this is not relevant for the calculation of the transfer function $h(t)$ which is a convolution of window function $w(t)$ and beam profile $b_t(t)$ in time-domain, see Equation 4.19. The transfer function is afterwards normalised to the same integral as the window function since beam shape must not change the total number of passing particles. See Figure 4.23 for an example of such calculation. There, the beam is wider than the shutter's opening so that full transmissibility in $h(t)$ never occurs.

$$h(t) = w(t) * b_t(t) \tag{4.19}$$

This method effectively uncoils the rotary shutter and describes it as a long strip of infinite width, with periodically repeating openings. Therefore, it is not considered that for large beams $b_x(x)$, parts of it might pass outside of the shutter or, in case of multiple openings, through an opening on the opposite side of it.

4.3.4. Distortion of a time-of-flight distribution by a rotary shutter

The ToF distribution $P_t(t)$ from subsection 4.3.2 describes flight time t of each particle in its own reference frame. Thus, it is called an individual ToF distribution. It is not directly obtainable as there is no way to gain knowledge about when each particle enters the ToF tube. To actually measure flight time in an experiment, a starting time needs to be set so that the measured signal $S(t)$ can be referred to this. Therefore, pulsing of the beam is required. Otherwise, a constant signal would be observed at the mass spectrometer.

The ToF distribution changes its shape when taking into account the transfer function described by the rotary shutter. This is done by a periodic convolution of the particles' individual ToF distribution $P_t(t)$ from subsection 4.3.2 and transfer function $h(t)$ from subsection 4.3.3. This yields the measured ToF distribution $S(t)$, as shown in Equation 4.20. If the transfer function was a very short pulse as yielded from a very narrow opening in the shutter, the ToF distribution would

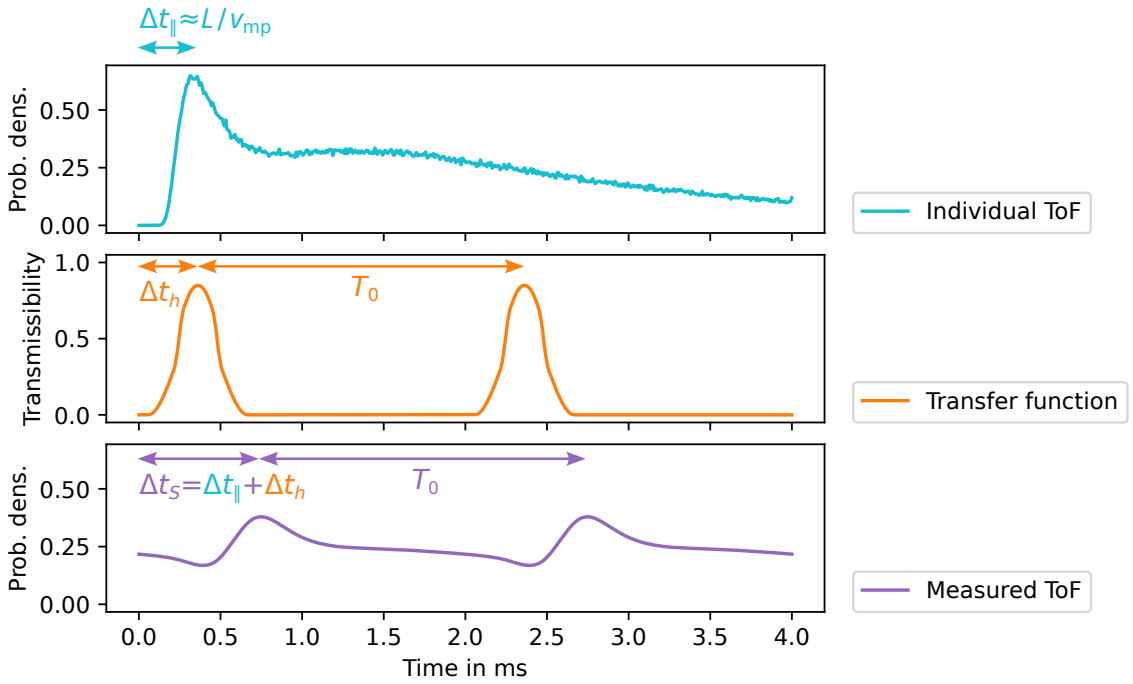

Figure 4.24.: **Distortion of a time-of-flight distribution by a transfer function** A divergent beam crosses the ToF tube and scatters at its walls. The beam profile is the same as in Figure 4.23 while angular distribution is that of a capillary with effective length $l_{\text{eff}} = 100$ to make scattering more visible here. The first plot shows the ToF distribution $P_t(t)$ of each particle in its own reference frame, so that all particles start travelling exactly at the same time $t = 0$. Transfer function $h(t)$ in the second plot is also the same as in Figure 4.23, time shift Δt_h is chosen arbitrarily. The third plot shows measured ToF distribution $S(t)$ of particles arriving at the detector.

barely change as this would correspond to a precisely known starting point. All particles would start travelling through the tube at the same moment, effectively resembling Equation 4.15. For longer opening times, the resulting distribution $S(t)$ looks broadened and more smeared, see an exemplary calculation in Figure 4.24. The measured ToF distribution has the same periodicity as the transfer function.

$$S(t) = h(t) * P_t(t) \qquad \text{from [Coo+20]} \tag{4.20}$$

The peak in the first plot of Figure 4.24 is caused by the bulk of non-scattering particles arriving at the detector after a time $\Delta t_{\parallel}$. As this part of the ToF distribution is skewed due to the background by scattering particles, it is not exactly given by L/v_{mp}, with v_{mp} the most probably velocity of the Maxwell-Boltzmann distribution, see subsection 5.1.3 for details. Still, $\Delta t_{\parallel}$ is closely linked to the beam temperature and is therefore a crucial characteristic quantity. $\Delta t_{\parallel}$ is also included in the delay Δt_S of the measured ToF distribution, with Δt_h the arbitrary delay of the transfer function. In an experiment, good synchronisation between the mass spectrometer and the position of the rotary shutter is required, so that the shift $\Delta t_{\parallel}$ between transfer function and measured ToF distribution can be determined exactly.

The rotary shutter blocks all particles for a time of $(1 - \alpha/360^\circ) \cdot T_0$. If this time is shorter than the time it takes the individual ToF distribution to fall off completely, frame overlap occurs. This causes an ambiguity in a particle's flight time: It might be a fast particle that was just emitted or a slow particle from the time when the shutter unblocked the path the time before. Note that for non-parallel beams, this reasoning is expanded from varying velocity to different flight distances, which increases the ambiguity further. In the next chapter, it will be shown that the frame overlap mainly stems from a background of scattered particles and that the ambiguity can be tackled by a model that describes this background.

In this section, a method was introduced to obtain the ToF distribution of atoms crossing a tube. Analytical calculation is only possible in an idealised case, which is the individual ToF distribution of particles in a parallel beam. In the previous sections, a realistic beam was found to be divergent and cause scattering inside the ToF setup. Considering this requires simulations of beam propagation. In contrast, it was found to be more beneficial to include a rotary shutter in an analytical way. The shutter is needed to pulse the beam and obtain a ToF distribution as measured. The dependence of pulsing from shutter geometry and its effect on ToF distributions are described in detail.

4.4. Conclusion

This chapter has described the propagation of hydrogen atoms through a ToF system for beam temperature measurements, from production to detection. Throughout particle source, skimmer setup and ToF tube, atoms diverging from the central axis require special consideration. In some cases, this can be handled analytically: The Tschersich model describes the beam shape at the exit of a capillary, an analytically calculated transfer function allows to adapt geometry

faster than for an explicitly modelled rotary shutter and a simple model of atoms in a ToF tube recovers the main features of a ToF distribution qualitatively. However, simulations often yield superior results: Implementing the Tschersich model in Molflow tells about the beam's near-field shape, skimmers in the beam forming section are too complex for an analytical description and simulations of the ToF setup are required to consider diffuse scattering.

The analytical models also help to understand the propagation of particles inside the capillary and the ToF setup. They can also save time of simulations and of manually processing intermediate data. Depending on the component whose influence should be considered, a mostly analytical procedure might be sufficient to find out about its relative impact. For instance, if the focus is on the ToF subsystem, one can capitalise on the modular approach of the framework and skip the computationally expensive skimmer setup. Instead, an angular distribution as emitted from the capillary can be set to enter the ToF setup. This angular distribution is also systematically adjustable in divergence by the parameter l_{eff}.

If most realistic and accurate results are to be generated, the presented procedure using mostly simulations needs to be utilised. As all subsystems build upon each other, a ToF distribution is determined for a system that is described by many parameters. Namely, these are the design parameters l_{eff} of the capillary and the geometries of the skimmer setup, the rotary shutter and the ToF tube, as well as particle mass, surface properties and beam temperature (see a full list of parameters in section A.2). For a system characterised by a specific parameter set, the yielded ToF distribution is the expected result of a measurement. In the following, parameter studies could be conducted to find out about the impact of various parameters on ToF data or to optimise for specific requirements. Instead, the next chapter builds upon the generated data in an inverse sense: The ToF data is taken as given and beam temperature is extracted.

5. Extracting beam temperature from time-of-flight data

In the previous chapter, the propagation of an atomic hydrogen beam in a ToF system was calculated and a ToF distribution was generated. In section 5.1, beam temperature is extracted from the ToF distribution. This requires to consider the distorted shape of the ToF distribution due to pulsing by the rotary shutter and the contribution from atoms scattering inside the ToF tube. In section 5.2, the accuracy of temperature determination is estimated and the impact of system geometry on accuracy is investigated.

5.1. Calculating temperature from a time-of-flight distribution

To determine beam temperature from a measured ToF distribution, the distortion caused by the rotary shutter is reversed by a deconvolution with the transfer function (subsection 5.1.1). The reconstructed individual ToF distribution is phenomenologically described by a model that also considers scattering particles (subsection 5.1.2). The model is used as a fit function and yields beam temperature as one of its fit parameters (subsection 5.1.3. Finally, it is explained how the statistical uncertainty of this method is estimated and how Monte Carlo simulations are used to predict the accuracy of temperature determination for application to real measurement data with limited statistics (subsection 5.1.4).

5.1.1. Reconstructing individual from measured time-of-flight distribution

As stated in subsection 4.3.4, measured ToF distribution has the same periodicity as transfer function. Consequently, all available information is contained in the time span of one revolution T_0 (or respectively less in case of multiple openings). So to improve signal-to-noise ratio, all measurement data can be averaged onto one interval. If in subsection 4.3.4 the individual ToF distribution $P_t(t)$ was reduced to one period, as shown in Figure 5.1 and Equation 5.1, its convolution with one period of the transfer function $h(t)$ would produce an identical measured distribution $S(t)$. Information loss due to frame overlap occurs anyway, either when folding the individual distribution or during periodic convolution.

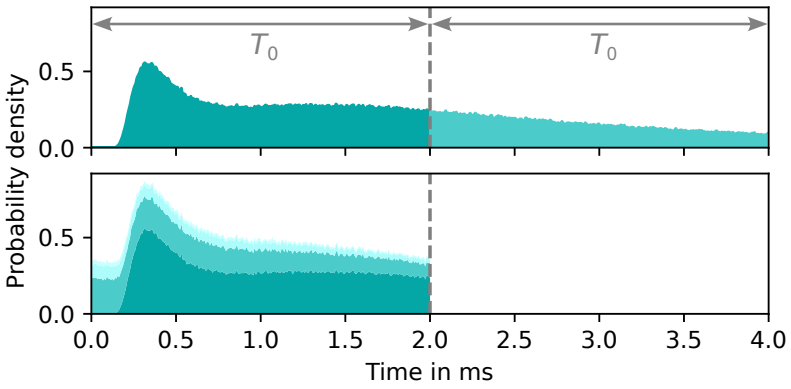

Figure 5.1.: **Reduction of a time-of-flight distribution to one period** The upper plot shows the individual ToF distribution $P_t(t)$ from Figure 4.24. A period of the rotary shutter takes $T_0 = 2\,\mathrm{ms}$. The distribution is folded into this time span, yielding the lower plot.

$$P_t^{\text{Folded}}(t) = \sum_j P_t(t + j \cdot T_0) \tag{5.1}$$

To reconstruct the ToF distribution $P_t(t)$ uninfluenced from the rotary shutter, a deconvolution of measured distribution $S(t)$ with transfer function $h(t)$ is performed. This is the reverse operation as in Equation 4.20, yielding the not directly measurable individual distribution $P_t(t)$. Transfer function is assumed to be known from geometry.

A convolution can be calculated as product of two functions in Fourier space, see Equation 5.2. Accordingly by deconvolution, one of the factors is retrieved by division of the product and the other factor in Fourier space, see Equation 5.3. This is shown here for individual ToF distribution $P_t(t)$, transfer function $h(t)$ and measured ToF distribution $S(t)$.

$$S_{\text{Noiseless}}(t) = h(t) * P_t(t) = \mathcal{F}^{-1}(\,\mathcal{F}(h(t)) \cdot \mathcal{F}(P_t(t))\,) \tag{5.2}$$

$$P_t(t) = \mathcal{F}^{-1}\left(\frac{1}{\mathcal{F}(h(t))}\,\mathcal{F}(S_{\text{Noiseless}}(t))\right) \tag{5.3}$$

In practice, noise $n(t)$ also needs to be taken into account, see Equation 5.4. This makes restoring the individual ToF distribution impossible as the noise term is random and unknown. In fact, applying deconvolution on non-ideal data greatly amplifies noise, often to unusability. This is due to the Fourier transformed transfer function $\mathcal{F}(h(t))$ in the denominator in Equation 5.3. That equation is rewritten with the noisy signal from Equation 5.4, yielding Equation 5.5. Whenever $\mathcal{F}(h(t))$ vanishes, it causes noise $\mathcal{F}(n(t))$ in the numerator to dominate restoration, even if noise was otherwise negligible. [GWE09]

A simple way to suppress this noise amplification is to increase low values of the transfer function in Fourier space $\mathcal{F}(h(t))$ to a threshold value. However, a more powerful method yielding better results is Wiener deconvolution, see Equation 5.6. Effectively, by application of a Wiener

filter, frequencies with lower value or higher noise-to-signal ratio are more suppressed, with NSR $= |\mathcal{F}(n(t))|^2 / |\mathcal{F}(P_t(t))|^2$. Noise could be statistically determined for each frequency but in this work a constant noise-to-signal ratio for all frequencies is manually set. Choosing a lower noise level effectively reduces noise but at the cost of introducing distortions.

$$S(t) = h(t) * P_t(t) + n(t) \tag{5.4}$$

$$P_t(t) \neq \mathcal{F}^{-1}\left(P_t(t) + \frac{\mathcal{F}(n(t))}{\mathcal{F}(h(t))}\right) \tag{5.5}$$

$$P_t^{\text{Wiener}}(t) = \mathcal{F}^{-1}\left(\frac{1}{\mathcal{F}(h(t))} \frac{1}{1 + \frac{\text{NSR}}{|\mathcal{F}(h(t))|^2}} \mathcal{F}(S(t))\right) \qquad \text{based on [GWE09]} \tag{5.6}$$

For implementation of deconvolution methods, it is important to respect periodicity by passing data with an exactly integer number of periods to the implemented function and by imposing periodic boundary conditions. This has been implemented by discrete fast Fourier transform. Also, an exactly integer number of data points should be used for one period. In the view of the author, a helpful resource to start working with deconvolutions is the respective chapter in the freely accessible essay about signal processing by professor emeritus O'Haver [1].

5.1.2. Phenomenological model of a time-of-flight distribution

To extract temperature from the reconstructed individual ToF distribution $P_t(t)$, an analytical description is needed in order to perform a fit. Particles scattering inside the ToF tube don't provide useful information about initial velocity distribution. Their contribution to the ToF distribution needs to be included in the fit function anyway as the fit could otherwise not converge, except for near-parallel beams where scattering is negligible.

Figure 5.2 describes the model of the scattering background as used in this work, with the four parameters weight λ, rise rate κ_r, fall rate κ_f and delay δ. The model is motivated by the conception that particles hitting walls are kept inside the tube scattering for a considerable time. They are quickly brought into the system until all particles of that batch are inside, described by the rising curve. Later, the particles stored scattering steadily leave the tube again, described by the falling curve. The delay takes into account that the signal is always zero at first since no particles reach the detector instantly.

The model is expected to be applicable to a wide range of beam temperatures: At higher temperature, particles will enter the system faster, which will be considered by adapted values of rise rate and delay. The assumption that particles scatter in the ToF tube many times implies that the fall rate will be mostly independent from temperature. Other fit functions have been tested as well, such as setting delay to a constant value or zero or using logistic instead of exponential functions. However, the presented model was found to describe a wide range of differently generated data

[1] Tom O'Haver. *A Pragmatic Introduction to Signal Processing*. Fourier Deconvolution. May 2023. url: `https://www.grace.umd.edu/~toh/spectrum/Deconvolution.html` (visited on 11/15/2023).

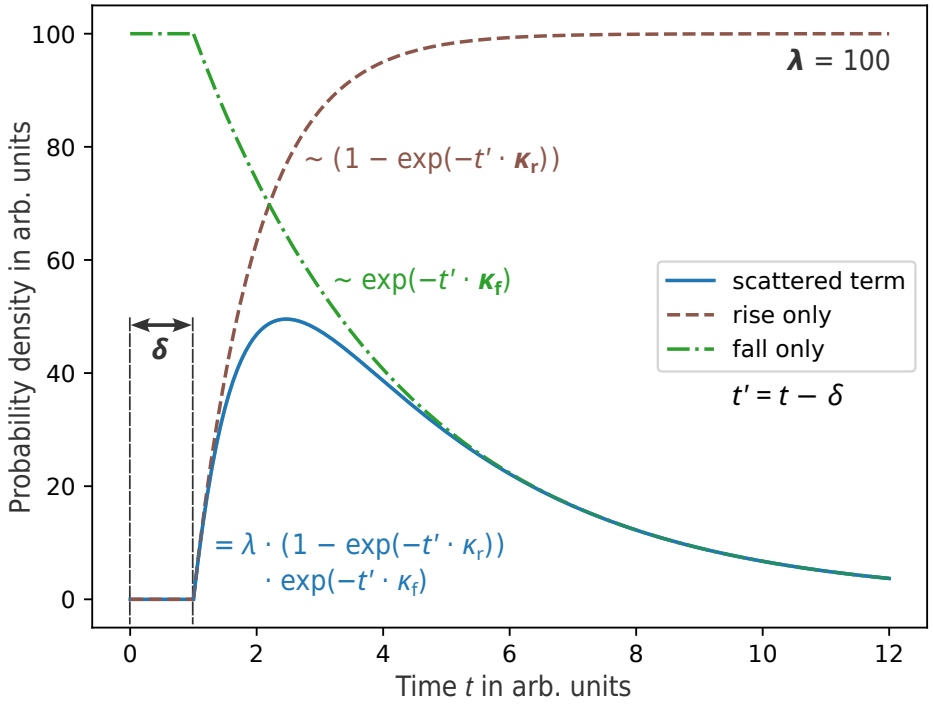

Figure 5.2.: **Model of the time-of-flight distribution of scattered particles** The ToF distribution of scattered particles is modelled by the solid blue line. It is calculated as a product of the green dash-dotted curve decreasing exponentially with κ_f and the brown dashed curve increasing exponentially with κ_r towards a constant value. There is a delay δ of the curves relative to t and the absolute value range λ is adjustable. The curve is fully described by the four mentioned parameters printed in bold.

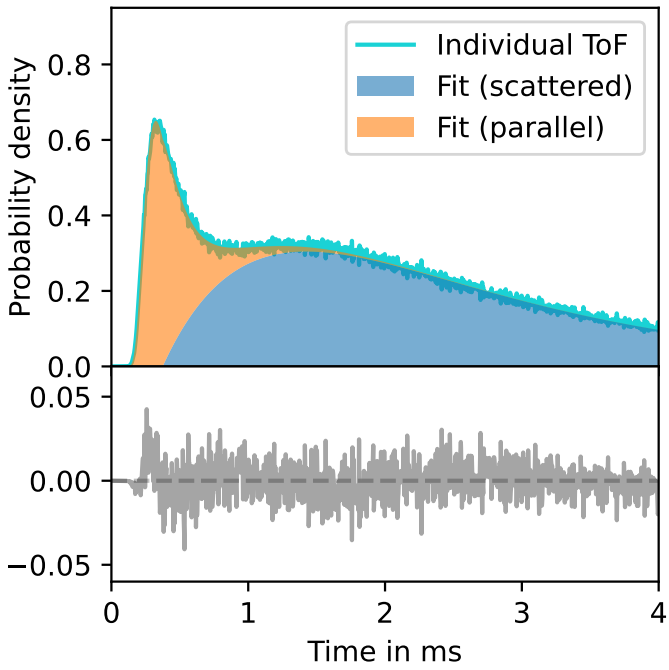

Figure 5.3.: **Fit of a model to an individual time-of-flight distribution** The individual ToF distribution $P_t(t)$ is the same as in Figure 4.24. The model $P_t^{\text{Model, expanded}}(t)$ of Equation 5.9 is fit to the distribution and describes it well. Residuals show only little structure.

sets well. Another fit function, possibly with less parameters, might still prove useful if more stable.

The total fit function consists of two parts: Firstly, the term from subsection 4.3.1, calculated from Maxwell-Boltzmann distribution and describing particles flying in parallel, see Equation 5.7. Secondly, the term derived in this section describing scattering background, see Equation 5.8. Both terms are summed with relative weight according to parameter λ, see Equation 5.9. It is written with a proportionality as the function is normalised afterwards. In Figure 5.3, good agreement of the fit function with the individual ToF distribution is shown.

As shown in subsection 4.3.4, the measured ToF distribution is periodic with rotation time T_0 of the shutter. This needs to also be resembled by the fit function, so it is folded to one period the same way as in Figure 5.1 and Equation 5.1, this yields Equation 5.10.

$$P_t^{\text{Parallel}}(t) = P_v^{\text{MB}}(L/t)\, L/t^2 \tag{5.7}$$

$$P_t^{\text{Scattered}}(t) = (1 - \exp(-\kappa_r t')) \exp(-\kappa_f t') \qquad \text{with } t' = t - \delta \tag{5.8}$$

$$P_t^{\text{Model, expanded}}(t) \sim \left(P_t^{\text{Parallel}}(t) + \lambda\, P_t^{\text{Scattered}}(t)\right) \tag{5.9}$$

$$P_t^{\text{Model}}(t) \sim \sum_j \left(P_t^{\text{Parallel}}(t + j \cdot T_0) + \lambda\, P_t^{\text{Scattered}}(t + j \cdot T_0)\right) \tag{5.10}$$

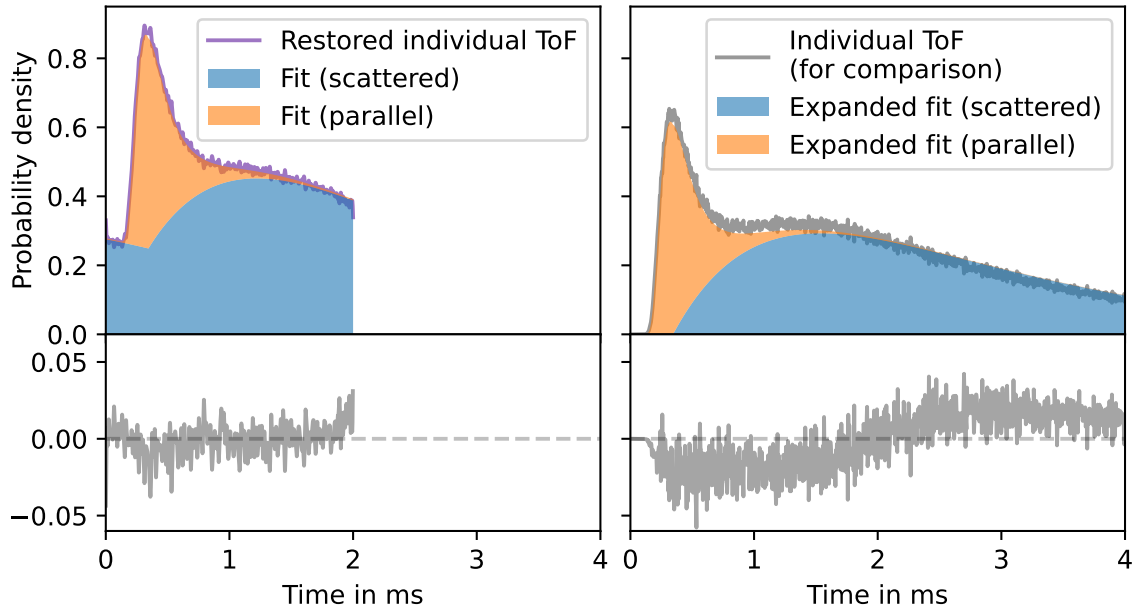

Figure 5.4.: **Fit of a model to a restored individual time-of-flight distribution** The left plot shows a fit of model $P_t^{\text{Model}}(t)$ to the folded restored individual ToF distribution $P_t^{\text{Reconstr}}(t)$. The yielded parameters inserted into non-folded model function $P_t^{\text{Model, expanded}}(t)$ result in the right plot. For comparison, it also shows the non-folded original ToF distribution $P_t(t)$.

5.1.3. Temperature extraction from preprocessed time-of-flight data

To determine temperature of the atomic beam when it entered the ToF setup, the function $P_t^{\text{Model}}(t)$ from Equation 5.10 is fit to the restored individual distribution $P_t^{\text{Reconstr}}(t)$ from subsection 5.1.1, this is shown in the left plot of Figure 5.4. This yields parameters such as temperature T of the beam's Maxwell-Boltzmann distribution. Due to periodicity, the fit is performed on one period of data, so one a folded distribution.

The ToF distribution over a longer time span without frame overlap can approximately be reconstructed by plotting the non-folded model function $P_t^{\text{Model, expanded}}(t)$ of Equation 5.9 with the yielded parameters, see right plot of Figure 5.4. Note the difference to Figure 5.3 where $P_t^{\text{Model, expanded}}(t)$ was fit directly to the individual ToF distribution $P_t(t)$ as demonstration. Deviations of fit from distribution are apparent from residuals in the right plot. They stem from amplified uncertainties by having determined scattering background from only a short time interval, namely one period T_0. As the parameters are often highly correlated, this can turn out inaccurate. Further, since the fit was performed on a restored ToF distribution, deviations occurring as a result of convolution and deconvolution with transfer function $h(t)$ show up here as well.

As the part of ToF distribution characterised by nearly-parallel particles $P_t^{\text{Parallel}}(t)$ (orange area in Figure 5.3) is skewed due to rising scattering background $P_t^{\text{Scattered}}(t)$ (blue area), its peak

is shifted to a later point in time. If a simpler fit function expecting an unskewed Maxwell-Boltzmann distribution was used, this would appear as slower particles. Consequently, beam temperature determined by such fit was expected to be offset to lower values. Considering scattering is thus necessary to estimate skewness.

This offset might be supposed to be amplified by increased path length of particles with a small angle θ which is greater than zero but low enough to not hit walls. However, this effect is neglectable for typical geometries of the ToF pipe. The increase in flight length is at maximum about $0.2\,\%$ for reduced length $l = 8$, the effect surpasses $1\,\%$ only for a rather wide pipe of $l \lesssim 3.5$.

Temperature T determined this way is not necessarily the best guess of beam temperature, it is initially only a parameter yielded from fit. As will be seen in section 5.2, T is usually lower than true value. This offset can either be investigated further to understand and correct it or calibrations might be conducted. Neither is covered in this work but the observation that this offset is a systematic effect will later allow corrections. Here, T is always referred to as beam temperature.

5.1.4. Estimating statistical uncertainty of measurement

Up to this point in the chapter, extraction of beam temperature from a ToF distribution was described. To learn about accuracy of this method, corresponding statistical uncertainties of determined temperature values need to be estimated. Two separate procedures with different aims are presented in the following. Firstly, simulated data is acknowledged to be the data source of this study. It is analysed considering the finite number of simulated particles. Extracted temperature and its uncertainty tell about how good or bad the framework works for various designs and under-the-hood settings, at low computational effort. Secondly, real measured ToF data is imitated by modifying simulated data sets by adding noise according to an assumed number of measured particles. Repeating this many times and statistically analysing the results, accuracy achievable with a specific setup in an experiment is estimated.

Uncertainty from simulated data

In this framework, the temperature measurement is powered by logged data of particles simulated by Molflow. The statistical uncertainty originating from the limited number of these particles is to be considered in order to estimate the required amount of data and the accuracy of extracted temperature or other fit parameters. For this, information about the uncertainty of a fitted ToF distribution needs to be provided to the fit function.

The simulated ToF distribution without normalisation is $P_t^{\text{Surf, raw}}(t)$, the number of particles in the bin of time t_i is called N_i, see Equation 5.11. Following Poisson distribution, uncertainty σ is given by the square root of particle number, see Equation 5.12. The analytical model is fitted onto distribution $P_t^{\text{Vol, folded, reconstr}}(t)$. Its uncertainty $\sigma\left(P_t^{\text{Vol, folded, reconstr}}(t_i)\right)$ at time t_i is to be found.

Thus, the uncertainty from a simulated distribution needs to be propagated to the distribution onto which a fit is applied.

Respecting volume correction, a ToF distribution $P_t^{\text{Vol}}(t)$ is calculated as described in subsection 4.3.2. Particles with flight time t_i are weighted individually according to their velocity but the number of atoms N_i is the same as for non-weighted $P_t^{\text{Surf}}(t)$. Therefore, the absolute uncertainty σ is the same for $P_t^{\text{Vol}}(t)$ when considering normalisation, see Equation 5.13. After correction, the ToF distribution is interpolated, the same is done separately for the corresponding uncertainty.

$$P_t^{\text{Surf, raw}}(t_i) = N_i \tag{5.11}$$

$$\sigma\left(P_t^{\text{Surf, raw}}(t_i)\right) = \sqrt{N_i} \tag{5.12}$$

$$\sigma\left(P_t^{\text{Vol}}(t_i)\right) = \frac{\sigma\left(P_t^{\text{Surf, raw}}(t_i)\right)}{\int P_t^{\text{Surf, raw}}(t')\,\mathrm{d}t'} \tag{5.13}$$

Measured ToF distribution $S(t)$ is calculated by periodic convolution of individual ToF distribution $P_t^{\text{Vol}}(t)$ with transfer function $h(t)$, see Equation 4.20. In the process, $S(t)$ is folded, so probabilities of all time intervals T_0 are summed. Note that $\sigma(S(t)) \neq h(t) * \sigma\left(P_t^{\text{Vol}}(t)\right)$, so it is not possible to analogously calculate uncertainty. This is because uncertainties need to be summed quadratically and not linearly. Thus, a workaround is used that does not require to determine uncertainty $\sigma(S(t))$ of measured ToF distribution.

The individual ToF distribution is folded, see Equation 5.14. Similarly, the corresponding uncertainty is calculated by a quadratic sum, see Equation 5.15. Individual ToF distribution $P_t^{\text{Vol, folded, reconstr}}(t)$ is reconstructed from measured ToF distribution as explained in subsection 5.1.1. In an ideal case, the reconstructed ToF distribution is identical to the original. In practise they are similar, see Equation 5.16. Therefore, the uncertainty of the reconstructed distribution by finite particle number is assumed to be approximately also the same, see Equation 5.17. This is how the uncertainty is propagated.

$$P_t^{\text{Vol, folded}}(t_i) = \sum_j P_t^{\text{Vol}}(t_i + j \cdot T_0) \tag{5.14}$$

$$\sigma\left(P_t^{\text{Vol, folded}}(t_i)\right) = \sqrt{\sum_j \sigma\left(P_t^{\text{Vol}}(t_i + j \cdot T_0)\right)^2} \tag{5.15}$$

$$P_t^{\text{Vol, folded, reconstr}}(t_i) \approx P_t^{\text{Vol, folded}}(t_i) \tag{5.16}$$

$$\sigma\left(P_t^{\text{Vol, folded, reconstr}}(t_i)\right) \approx \sigma\left(P_t^{\text{Vol, folded}}(t_i)\right) \tag{5.17}$$

The estimated statistical uncertainty is given as input to the fitting function [2]. Bounds for fit parameters are set in order to prevent extreme values from being assigned. The allowed ranges are wide enough that optimal values are usually not near bounds. When the fit converges, the found optimal parameter set and the respective uncertainties are output. Due to interpolation of ToF distribution $P_t^{\text{Vol}}(t)$, statistics seems better to the fit function than it is. Therefore, the output uncertainties are too small. This was found to be corrected by multiplication with $\sqrt{r}$, with r the factor by which interpolation increases the number of data points. Possibly, this correction is only approximately correct, it was not checked in the source code.

χ^2_{Reduced} is calculated as a sum over the squared differences of the fit from the reference data, normalised by their uncertainty. This is divided by the number of degrees of freedom, which is the number of data points reduced by the number of fit parameters. No correction is applied due to interpolation. χ^2_{Reduced} estimates how good the fit function $P_t^{\text{Model}}(t)$ agrees with the reconstructed individual ToF distribution $P_t^{\text{Reconstr}}(t)$.

As an additional measure, the agreement between the fit function $P_t^{\text{Model}}(t)$ and the folded individual ToF distribution $P_t^{\text{Folded}}(t)$ is determined. This is only possible for a simulated setup as the individual ToF distribution is not exactly known in a real experiment. Compared to χ^2_{Reduced} of only the fit, this quantity also takes into account deviations caused by convolution (see subsection 4.3.4) and deconvolution (see subsection 5.1.1) of the ToF distribution with the transfer function. Lastly, the expanded fit function $P_t^{\text{Model, expanded}}(t)$ can be compared to the original ToF distribution $P_t(t)$. This is an indicator for an inaccurately detected scattering background despite a potentially good fit, see a demonstration of the effect in Figure 5.4.

Simulated uncertainty of measurement

When analysing data of a real experiment, the starting point is the measured ToF distribution. The signal will be more or less noisy as the mass spectrometer detects only a finite number of particles. The idea of MC simulations described here is to produce a ToF distribution that looks as if a number N_{MC} of particles had been measured. This means manually adding noise according to Poisson distribution. By analysing this data, dependency of measurement accuracy on amount of statistics is tested and accuracy of different setups at same statistics is estimated. It is also possible to apply the same procedure to the original or reconstructed individual ToF distribution $P_t(t)$ instead of measured ToF distribution $S(t)$. This can be used to benchmark different steps of the framework or investigate inaccuracies introduced by systematic effects.

An ideal ToF distribution without noise is needed as base for MC simulations. This is not obtainable since ToF distribution is not analytically known but determined from a number of simulated particles. Therefore, simulated distribution is slightly smoothed to hide noise at the cost of resolution losses and then assumed ideal.

[2] Information about the used implementation in *scipy* (used version: 1.10.0) as well as references at: `https://docs.scipy.org/doc/scipy/reference/generated/scipy.optimize.curve_fit.html`. Information and references about *Trust region reflective* algorithm as minimiser function at: `https://docs.scipy.org/doc/scipy/reference/generated/scipy.optimize.least_squares.html`.

The amount of added noise depends on the assumed number of measured particles N_{MC} that is freely chosen. As an example, statistical uncertainty corresponding to $N_{\mathrm{MC}} = 10^8$ particles is investigated in the simulations shown in section 5.2. ToF distribution is scaled such that its total number was N_{MC} if it was not interpolated. Since it is, its total number is set to rN_{MC}, with r the factor by which interpolation increases the number of data points. For each time t_i, a specific value of deviation is randomly picked according to a Gaussian distribution with expectation value $\sqrt{N_i}$. This exact same deviation is added to all r data points at the same t_i. This is an approximation to the fact that all of these r points were affected if the one value N_i of the non-interpolated ToF distribution was deviating. So this approximation only neglects that the spline would look different. This again is relaxed by smoothing ToF distribution after noise is added.

This way, a noisy version of measured ToF distribution $S(t)$ is produced. It is deconvoluted by transfer function $h(t)$ to yield reconstructed individual ToF distribution $P_t^{\mathrm{Reconstr}}(t)$, this is the distribution onto which the analytical model is fit. Uncertainty of particle number is determined from a slightly modified version of this distribution. In case of low assumed particle number N_{MC}, the Gaussian distribution is no longer a good approximation of the Poisson distribution. Thus, the distribution is very noisy and some points have negative value. To prevent errors from happening and randomly low values from being weighted too strongly, the distribution is smoothed and a lower threshold is introduced. Then, uncertainty is determined as square root. Alternatively, fluctuations could be calculated using the Poisson distribution.

The procedure is repeated several times, for the simulations shown in section 5.2 for instance 1000 times. Optimal values of fit parameters found in each iteration are saved. For each parameter, a histogram can be generated which shows distribution of found values. Best-fit value sets with a parameter near one of its bounds are discarded, except for delay δ near lower bound. From all other parameter sets, mean value and standard deviation are calculated. The respective value for temperature T_0 is the result of the MC simulation. Additionally, one more fit is performed which follows the same procedure except that no noise is added to the ToF distribution. This helps to understand for instance the offset between the two presented procedures compared to the impact of added noise.

5.2. Estimating the accuracy of temperature determination by time-of-flight

The analysis procedure described in the previous section is used to extract beam temperature from ToF distributions of various simulated systems. Guidelines are given on how to design setups for low scattering and a narrow transfer function of the rotary shutter. Parameter studies are conducted to estimate the accuracy of temperature determination for varying amounts of scattering, different geometries of the ToF setup and for hot and cold atomic beams. This way, the dependence of measurement accuracy from design parameters is investigated.

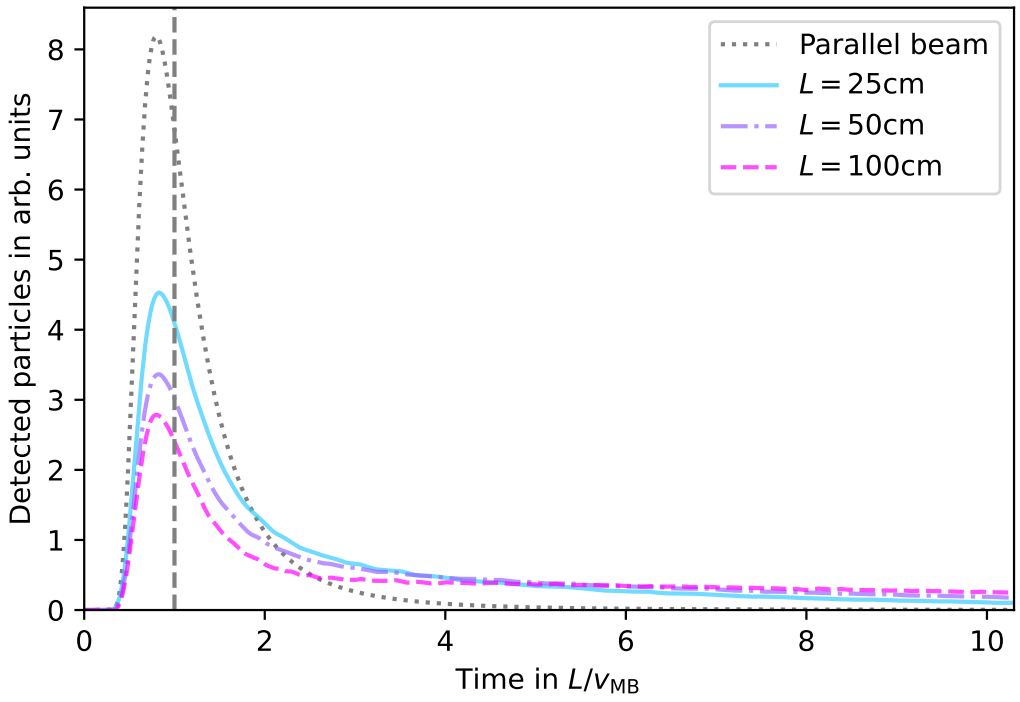

Figure 5.5.: **Normalised time-of-flight distributions for different tube lengths** ToF distribution of a capillary of reduced effective length $l_{\mathrm{eff}} = 8$ and second skimmer diameter $D_{\mathrm{S}} = 6\,\mathrm{mm}$ for different lengths L of the ToF tube. Time is given in multiples of the time it takes a hydrogen atom of temperature $300\,\mathrm{K}$ with mean Maxwell-Boltzmann velocity of $v_{\mathrm{MB}} = 2520\,\mathrm{m\,s^{-1}}$ to cross the respective tube along its axis. For comparison, calculated ToF distribution of a parallel beam is also shown.

5.2.1. Optimisation of setups for accuracy

During the design process of a measurement system, many combinations of parameter values to describe geometry are feasible. Several values can be chosen quite freely when other parameters of the parameter set are appropriately adapted, for instance it might not be apparent whether the preferable way to halve the time between two openings is doubling the rotation frequency or doubling the number of openings of the rotary shutter. In this subsection, advice is given on how to achieve two typical optimisation goals that aid more accurate determination of temperature: reducing scattering in the ToF tube and reducing smearing of a ToF distribution by the transfer function of the rotary shutter.

Reducing scattering

Scattering in a ToF tube is an unwanted effect that should be suppressed as much as possible. Information about temperature is yielded from particles hitting mass spectrometer directly, while scattered particles create a background. This part of ToF distribution $P_t^{\mathrm{Scattered}}(t)$ is the blue area in Figure 5.4, it has longer fall-off time and is the main cause of frame overlap. It is approximately

described by the phenomenological model in Equation 5.10. Orange area $P_t^{\text{Parallel}}(t)$ in the plot is generated from particles flying in parallel, its shape is skewed and position of peak, which is a direct measure of temperature, is shifted by scattering background. Thus, a higher number of scattering particles increases uncertainty of the fit, making temperature extraction more inaccurate.

In an ideal case, entering atomic beam is parallel and no scattering occurs. Coming closer to this situation is a main reason why skimmers are used and investigated in section 4.2. If beam was parallel, choosing a longer ToF tube at otherwise same settings results in proportionally higher flight time t due to constant velocity $v = L/t$. At same shutter settings, this changes distribution of detected particles over time. This can be compensated by accordingly lower rotation frequency $f = 1/T_0$, measured ToF distribution $S(t)$ then stays the same apart from being elongated. This is due to $S(t) = h(t) * P_t(t)$ (Equation 4.20) with transfer function $h(t)$ in Equation 4.16 stretched by increased T_0 and individual ToF distribution $P_t(t)$ in Equation 4.4 stretched by increased length L by the same factor.

For a divergent beam, scattering at walls needs to be considered. Figure 5.5 shows ToF distributions with compensation of different flight times due to different lengths L, so plotted over normalised time. For longer tubes, they deviate more and more from that of the ideal parallel beam. A higher share of particles arrives at later times, intensity near peak of almost parallel atoms is respectively lower. As stated in Equation 4.10 for the approximation of particles entering the tube from centre, atoms emitted under a polar angle θ scatter at walls at least once if $L \tan(\theta) \geq R$. So the longer the tube, the more particles hit walls instead of reaching the outlet directly and the scattered atoms also hit walls more often until they escape. For the exemplary lengths in Figure 5.5 of $L = 25\,\text{cm},\ 50\,\text{cm}$ and $100\,\text{cm}$, particles hit walls on average 10, 36 and 140 times.

Thus, a shorter tube is preferable due to less scattering. However, systematic uncertainties which are not considered in this work will counteract this assessment such that a medium value will be best suited. Dominating deteriorating effects for short tubes might be a uncertainty in flight distance by skewed orientation of the rotary shutter or the finite length of the detection volume of the mass spectrometer, limited time resolution of the mass spectrometer or inaccurate timing between shutter opening and particle detection. It should be noted that a larger diameter of the ToF tube would also prevent scattering as long as the condition was still fulfilled that all particles are absorbed at the outlet or at least do not scatter back into the tube and onto the mass spectrometer. This depends on how particles are pumped at the end of the ToF tube. As no details about this implementation are considered in the simulated setup, no recommendations about the diameter of the ToF tube are given in this work.

Reducing width of transfer function

The atomic beam is pulsed by the rotary shutter when entering the ToF setup. Measured ToF distribution $S(t)$ is calculated as a convolution of individual ToF distribution $P_t(t)$ with transfer function $h(t)$, so $S(t) = h(t) * P_t(t)$ as in Equation 4.20. Depending on the width of $h(t)$, the distribution is smeared which can contribute to frame overlap and conceals structure of the

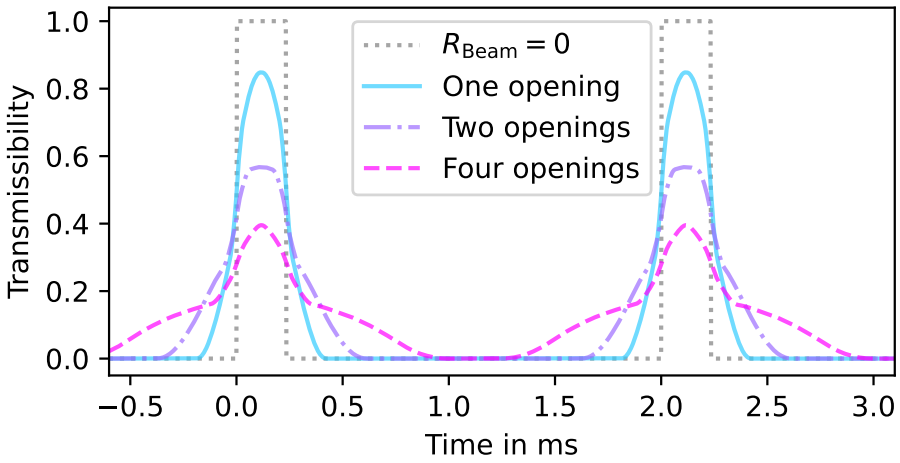

Figure 5.6.: **Transfer function for different numbers of openings** Blue solid curve shows transfer function for rotation frequency $f = 500\,\text{Hz}$ and one opening with opening angle $\alpha = 42°$. In the simulation with two openings, opening angle and rotation frequency are halved, so area under the curve is the same. For four openings, parameters are adapted analogously. For comparison, window function is shown which is identical to transfer function in case of vanishing beam diameter.

curve, see as an example Figure 4.24. Reconstruction of a strongly smeared ToF distribution requires better knowledge of the transfer function and it is also harder to determine, for instance finding orange transfer function in Figure 4.23 requires more information than the more ideal blue window function. Also, reconstruction is more sensitive to noise as the signal intensity is more similar at different points in time. Thus, smearing should be kept small by keeping $h(t)$ narrow.

As the transfer function is a convolution of window function $w(t)$ and beam profile $b_t(t)$ in time domain, $h(t) = w(t) * b_t(t)$ (Equation 4.19), both constituents need to be as temporally short as possible. So an ideal transfer function, a periodically repeating delta function, would not only require negligibly narrow openings in the shutter but also a pointlike beam. As stated in Equation 4.16 or the blue annotation in Figure 4.23, window function $w(t)$ becomes more narrow for smaller opening angle α but this comes with lower duty cycle $\alpha/360°$ and lower total throughput, worsening statistics. Alternatively, this is also achieved for higher rotation frequency $f = 1/T_0$, though time between two openings should better be adapted with regard to potential frame overlap.

Keeping window function $w(t)$ constant, the other variable is beam profile. $b_x(x)$ is adjustable by diameter of skimmers D_S, see profiles in Figure 4.17a. In the context of the ToF setup, $b_x(x)$ is fixed but $b_t(t)$ depends on shape of the rotary shutter, see Equation 4.18 or the green annotation in Figure 4.23. For larger shutter size R_Shutter, beam appears smaller in comparison, but in practice, shutter diameter is constrained by the vacuum system. If the shutter has multiple openings, reducing their number n is a straightforward way to increase rotation frequency f while keeping time $T_1 = T_0/n$ between two openings constant. By increasing opening angle α accordingly, opened time $\alpha/360° \cdot T_0$ stays the same, and so does duty cycle $n\alpha/360°$ of the rotary shutter

and window function $w(t)$. Still, higher rotation frequency $f = 1/T_0$ leads to a temporally compressed beam profile $b_t(t)$ and this causes shorter transfer function $h(t)$. This effect is demonstrated in Figure 5.6.

Effectively, beam size appears like it shrinks for reduced number of openings. For the contrary, imagine a rotary shutter with a huge number of very narrow openings: The beam would always pass through several openings at the same time and barely any structure in the transfer function and measured ToF distribution would occur. In conclusion, shortest transfer function $h(t)$ and least smearing is yielded for a single opening, largest possible rotary shutter and beam passing at maximal distance R_{Shutter} from centre, smallest opening angle α and skimmer diameter D_{S} that statistics allows and highest rotation frequency f that frame overlap and mechanics allow. If either window function $w(t)$ or beam profile $b_t(t)$ is already much shorter than the other, these recommendations can be relaxed since benefit of shortening the more narrow component even further is small.

5.2.2. Dependence of accuracy from beam shape and geometry

Guidelines like those presented in the previous subsection for optimising accuracy of temperature measurements when designing ToF systems can be found from general principles. However, not all design parameters have intuitively clear impact. To learn about their influence on accuracy, parameter studies are conducted. Many individual simulations are run with the parameters of interest sweeping through chosen ranges. Inspecting temperature and other fit parameters over swept parameters, such as beam divergence, rotation frequency and opening angle, tells about their dependency for at least the specific simulated setup. Abstracting observed trends to find general rules often requires further investigation but eventually, gained insights tell about ways to optimise a setup for enhanced accuracy or they disclose flaws in the analysis procedure. Knowing how to handle these or fixing them improves accuracy and stability. The process of gaining insights this way is illustrated in the following.

Parameter study of beam divergence

Particles in a ToF setup are simulated and a ToF distribution is calculated, the fit function $P_t^{\mathrm{Model}}(t)$ from Equation 5.10 yields the parameters shown in Figure 5.7. Temperature T_{MC} from MC simulations is determined as described in subsection 5.1.4. A realistic shape of the beam entering the ToF setup would be yielded from simulating its propagation through a skimmer setup. Here, only the beam profile of such a simulation is used but the beam's angular distribution is that of a capillary which is characterised by the reduced effective length l_{eff}, so it is calculated analytically as described by Tschersich (see subsection 4.1.1). This allows to systematically and analytically vary the degree of beam divergence. Lower l_{eff} increases beam divergence and particle scattering which is expected to impair temperature determination, compare to the discussion in subsection 5.2.1.

Definitions of parameters that describe the scattered share of ToF distributions are found in Figure 5.2. Rise rate κ_{r} and delay δ are measures of how fast particles enter a system, they are

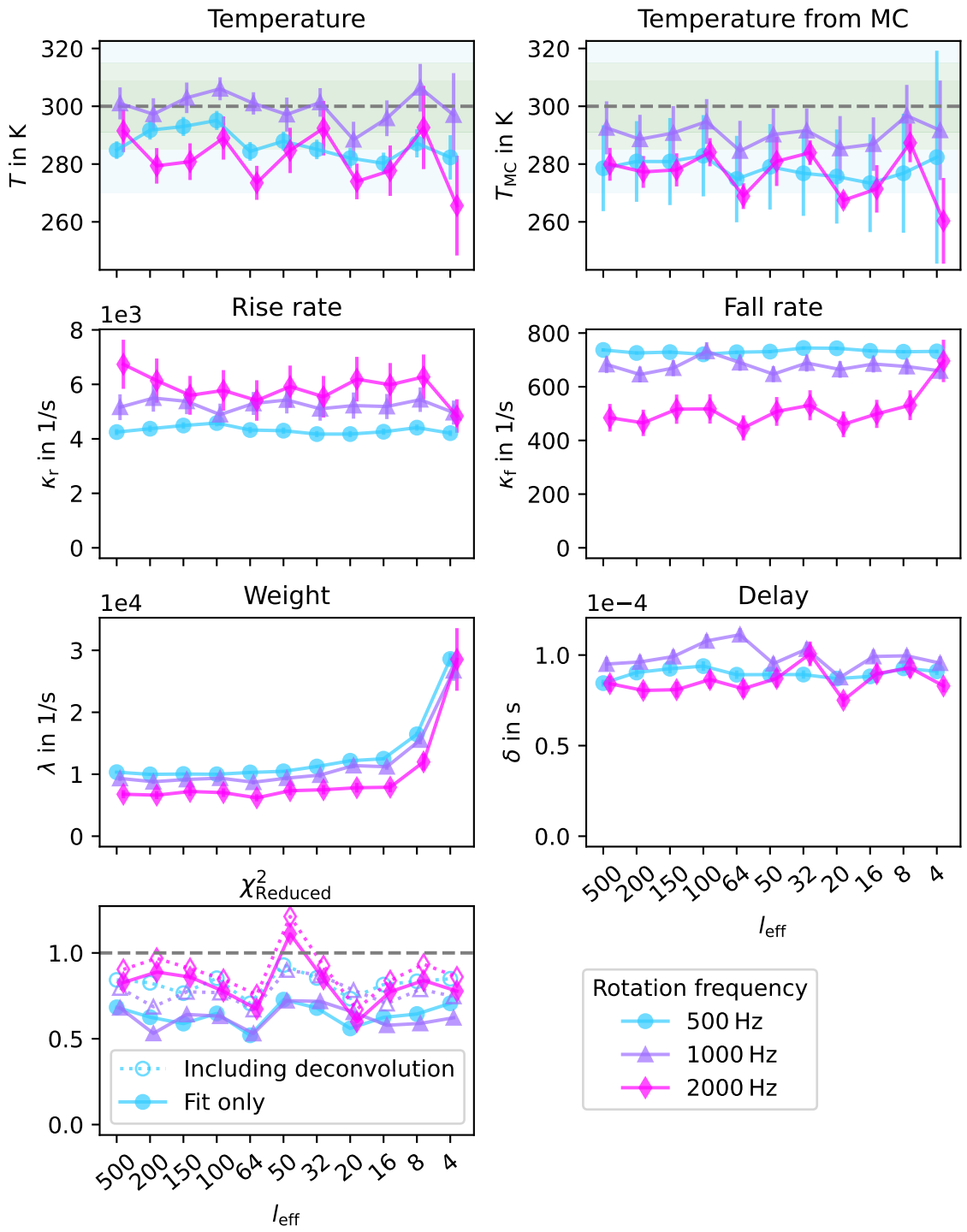

Figure 5.7.: **Dependence of determined temperature from beam divergence** Parameter study of ToF measurements. Monte Carlo (MC) simulations assume 10^8 particles. The entering beam has a temperature of $300\,\mathrm{K}$, a profile as after passing a skimmer setup and the angular distribution of a capillary with reduced effective length l_{eff}. Smaller l_{eff} results in a more divergent beam. Length of the ToF tube is $L = 50\,\mathrm{cm}$, the rotary shutter has one opening with opening angle $\alpha = 21°$. In the temperature-subplots, deviations up to $3\,\%$, $5\,\%$ and $10\,\%$ are coloured.

mostly independent of beam divergence but depend on particle velocity, compare to higher temperature in Figure 5.8, rise rate is higher and delay lower there. Fall rate κ_f describes how fast particles leave a ToF tube. Its independence from beam divergence is expected since the initial angle θ has no more effect after hitting a wall for the first time. It is also constant for different beam temperatures as particles are thermalised after a few hits. Weight λ is the share of scattering background $P_t^{\mathrm{Scattered}}(t)$ as compared to ToF distribution from parallel particles $P_t^{\mathrm{Parallel}}(t)$, see Equation 5.10. For smaller l_eff, more particles scatter and weight λ grows. It is mostly independent of beam temperature.

Correlations between parameters are visible in the plot. Generally appearing and almost full correlations are between weight λ, fall rate κ_f and negatively with rise rate κ_r. This means that these three parameters do not offer much more than only one degree of freedom, this may be considered when designing a new fit function in the future. Other correlations are only partial and have varying sign and degree, depending on the specific simulation. This is in general also true for temperature T which should ideally be uncorrelated from parameters describing scattering background. However, in the parameter studies of this section, T is positively correlated with rise rate κ_r. To make this correlation plausible, imagine a specific ToF distribution with the peak from parallel particles $P_t^{\mathrm{Parallel}}(t)$ at a specific point in time. Peak is shifted to higher times by lower temperature and also by higher rise rate due to steeper increase of scattering background $P_t^{\mathrm{Scattered}}(t)$, compare to Figure 5.3. If rise rate κ_r is overestimated, temperature T is also overestimated to keep position of the peak constant.

Temperature T corresponds to the Maxwell-Boltzmann velocity distribution of atoms in a parallel beam. In Figure 5.7, it is seen to be mostly constant over beam divergence and all determined values are within a maximum deviation to the true value of about $10\,\%$. Only for the most divergent tested beam of $l_\mathrm{eff} = 4$, more significant deviations are seen in various parameters. Uncertainty of temperature is larger for smaller effective length l_eff of capillary, this was mentioned before to be expected due to more dominating background of scattered atoms.

At higher rotation frequencies f of the shutter, fitted temperature fluctuates more strongly and uncertainties are higher. This is supposed to be caused by the temporally short interval $T_0 = 1/f$ on which the fit is performed. Similar to the left plot of Figure 5.4, ToF distribution in this short interval is dominated by the peak from parallel atoms $P_t^{\mathrm{Parallel}}(t)$ and the fit is more likely to inaccurately estimate rise and fall rates of scattered particles $P_t^{\mathrm{Scattered}}(t)$. This results in more inaccurately determined peak skewness and, thus, temperature.

The determined temperature T is lower than the true value of $300\,\mathrm{K}$, except for rotation frequency of $f = 1000\,\mathrm{Hz}$. This offset appears in most simulations using the framework, possibly rise κ_r of scattering background is not well described for small times or scattering is systematically underestimated causing a shift of peak to higher flight times. However, the absence or compensation of this offset for $f = 1000\,\mathrm{Hz}$ is unusual. To find out about its cause, a parameter study of different rotation frequencies could be performed. In combination with analysis of ToF distributions of the individual simulations, it can be tested if this is a systematic effect and which other frequencies are affected.

Temperature T_MC as determined from MC simulations is different from T especially in two respects. Firstly, T_MC is shifted to lower temperatures. Based on testing with some simulations,

the offset seems to be caused by fitting data with changed weight. For MC simulations, weight is based on Poisson statistics of measured ToF distribution $S(t)$, see details in subsection 5.1.4. In contrast, the fit yielding T is based on the actually simulated number of particles. Due to volume correction, see subsection 4.3.2, more particles are simulated in $P_t^{\mathrm{Surf}}(t)$ with higher velocity than corrected distribution $P_t^{\mathrm{Vol}}(t)$ suggests, so higher weight is put on smaller times. Therefore, rising edge of peak is more strongly weighted which might cause a shift of fitted peak to lower times, causing determined temperature T to be higher.

Secondly, temperature T_{MC} from MC simulations also fluctuates most for highest rotation frequency f but corresponding uncertainty is lowest. In contrast, for T it is lowest for low frequencies. Possibly, fit is more resilient to noise in case of higher f since total time span T_0 of reconstructed folded ToF distribution $P_t^{\mathrm{Reconstr}}(t)$ is shorter and therefore the peak from parallel particles is present in a larger percentage of it. It is also seen in the plot that fluctuations of T_{MC} are larger than their estimated uncertainties. Since these variations are most probably no actual features, this hints at a dependency of determined temperature from the particular run of simulation. Thus, assuming the smoothed simulated data to be ideal, see subsection 5.1.4, seems not to be entirely justified.

Most values of $\chi^2_{\mathrm{Reduced}}$ lie between 0.5 and 1 which hints at good agreement of fit function $P_t^{\mathrm{Model}}(t)$ with simulation of reconstructed individual ToF distribution $P_t^{\mathrm{Reconstr}}(t)$. It is noteworthy that this agreement is about constant for all degrees of beam divergence. As an additional measure, deviation of fit function from folded individual ToF distribution $P_t^{\mathrm{Folded}}(t)$ is given by unfilled markers in Figure 5.7, for details see subsection 5.1.4. This quantity also takes into account deviations caused by convolution (see subsection 4.3.4) and deconvolution (see subsection 5.1.1) of the ToF distribution with the transfer function. As its value is only slightly higher, impact of these operations is properly low.

This parameter study demonstrates robustness of the developed framework with respect to beam divergence. The method becomes significantly less accurate only for much more scattering than a reasonable skimmer system achieves. Parameters describing scattering background are also consistent over changing divergence. Temperature fluctuates increasingly for higher rotation frequency so this seems to make determination unstable. However, MC simulations show that precision increases at the same time. If stability can be improved, this hints at higher frequencies being beneficial. Next, a parameter study of rotation frequency is conducted.

Parameter study of rotation frequency

Evaluating ToF data of a hot atomic beam is expected to be more tricky as the peak of parallel particles indicating temperature is temporally much shorter than for room temperature. At the same time, scattering background still extends far, complicating the design balance between high resolution of peak and low frame overlap. To sweep through this balancing quantity, a study of rotation frequency is conducted. Additionally, prediction from subsection 5.2.1 about the impact of changing opening angle is verified by MC simulations. A beam of realistic shape as calculated in section 4.2 is assumed entering ToF setup.

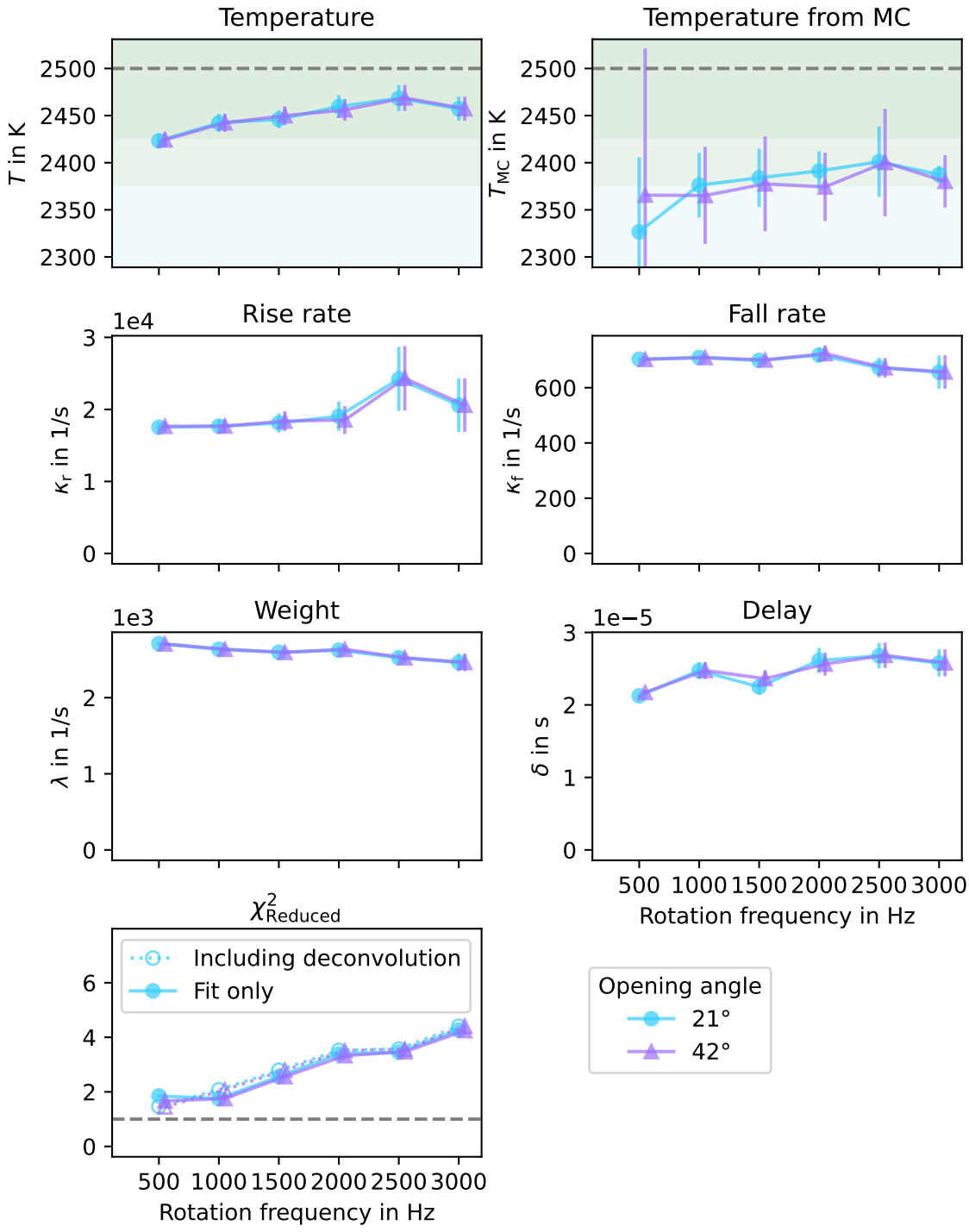

Figure 5.8.: **Dependence of determined temperature from rotation frequency** Parameters of the setup are chosen similarly to Figure 5.7 but beam temperature is $2500\,\mathrm{K}$ and a realistic beam shape is chosen, as calculated for a skimmer diameter of $D_S = 6\,\mathrm{mm}$.

As noted in the discussion of Figure 5.7, higher beam temperature of $2500\,\mathrm{K}$ in Figure 5.8 causes higher rise rate κ_r and lower delay δ due to faster injection of atoms into the ToF system, while fall rate κ_f is about equal. Divergence of the more realistic beam shape in this parameter study is roughly similar to the less divergent beams in the previous study. Amount of scattering is not directly comparable by weight λ since parallel share $P_t^{\mathrm{Parallel}}(t)$ and scattered share $P_t^{\mathrm{Scattered}}(t)$ of ToF distribution are not normalised before combining them, so value of weight λ depends on the rise and fall rates. These four parameters describing scattering change only slightly over rotation frequency but in a similar way as observed from the three different curves in Figure 5.7.

The trend of how uncertainties of temperatures T and T_MC change with frequency is the same for both parameter studies. Determined temperature rises slightly for increased rotation frequency f which might be driven by correlation with rise rate κ_r and the other parameters describing scattering. In the previous study at $300\,\mathrm{K}$, the increase is not observed but a potential maximum for $f = 1000\,\mathrm{Hz}$. Here, a maximum might exist for $f = 2500\,\mathrm{Hz}$ but confirming this requires further investigation, for instance by a study that checks if these are maxima or points of peak trueness and whether their frequencies shift with respect to beam temperature. Such shift seems plausible since best choice of rotation frequency is closely connected with beam temperature. For too low frequency, accuracy can deteriorate. The peak of $P_t^{\mathrm{Parallel}}(t)$ that indicates temperature becomes temporally very short in comparison to the too long time T_1 between openings, so it might not be considered sufficiently by fit.

χ^2_Reduced is significantly greater than 1 and rises with increasing rotation frequency. This hints at unsatisfactory description of generated ToF distribution by fit function and has two main reasons. Firstly, at $f = 500\,\mathrm{Hz}$, deviation of fit is larger from reconstructed $P_t^{\mathrm{Reconstr}}(t)$ (filled markers) than from original $P_t(t)$ (unfilled markers) individual ToF distribution. Since the model is fit to the reconstructed distribution, one would expect better agreement with this distribution. The inversion is often caused by artefacts from deconvolution of measured ToF distribution $S(t)$ with transfer function $h(t)$. During this operation, noise is amplified and ringing might appear which is a periodic fluctuation of the curve. These effects are mostly ignored by the fit but they increase χ^2_Reduced which is calculated from deviations.

Secondly, peak from parallel particles $P_t^{\mathrm{Parallel}}(t)$ is often not described by the fit very accurately. This might be caused by the fit prioritising little deviation at the much larger section of falling flank of $P_t^{\mathrm{Scattered}}(t)$. Also, shape of the curve is modified near peak due to smoothing that is inherent in the Wiener deconvolution algorithm, see subsection 5.1.1. Deviation near peak is the main contribution to χ^2_Reduced and is about equal for all rotation frequencies considered here. However, its relative impact becomes increasingly larger as time interval $T_0 = 1/f$ becomes shorter.

For the two simulated opening angles α, most parameters are nearly identical. This is expected as the agreement between $P_t^{\mathrm{Reconstr}}(t)$ and $P_t(t)$ is barely determined by properties of the rotary shutter. This is because transfer function $h(t)$ in these simulations is assumed to be known exactly and no noise is added to measured ToF distribution $S(t)$. Noise is only added for MC simulations, temperatures T_MC determined from those differ slightly, they tend to be slightly higher for smaller opening angle. Calculated uncertainties are significantly lower for the narrower opening. As discussed in subsection 5.2.1, corresponding transfer function is narrower and, thus, measured

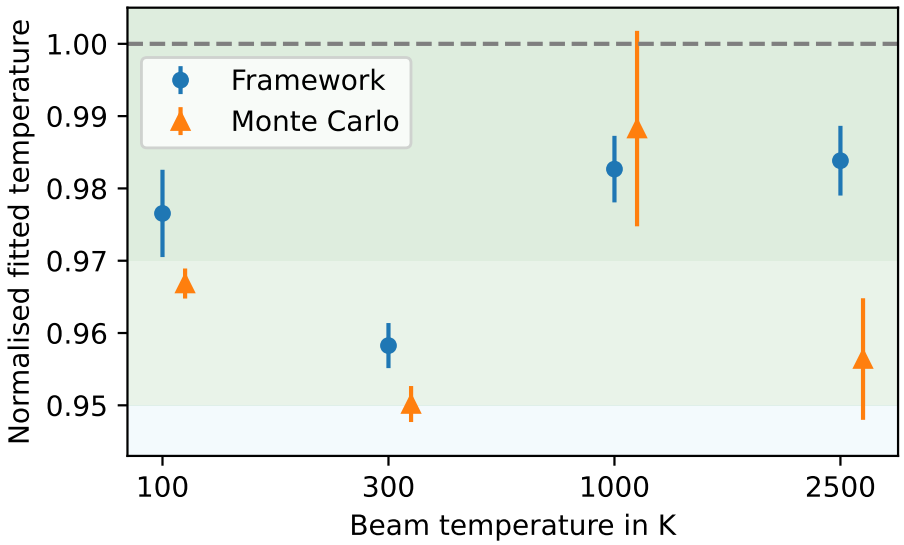

Figure 5.9.: **Accuracy of determined temperature for different beam temperatures** Temperature is calculated from simulated data (Framework) and from modified data mimicking an experimental measurement of 10^8 particles by Monte Carlo simulations. It is determined by the same setup for different beam temperatures and relative deviation is plotted. Incident beam has realistic shape as calculated for a skimmer diameter of $D_S = 6\,\mathrm{mm}$. Length of ToF tube is $L = 50\,\mathrm{cm}$, rotary shutter is spinning at $2000\,\mathrm{Hz}$ and has one opening with opening angle $\alpha = 21°$.

ToF distribution is less smeared. This means a more structured curve with higher dynamics, so it is less affected by noise. Note that this evaluation assumes same statistics in both versions. In two experiments with same measurement time, half opening angle would result in half number of detected particles, so noise would increase by $\sqrt{2}$. This does not necessarily translate into linearly higher uncertainty T_{MC} but this depends on how deconvolution and fit deal with varied statistics, and this again can be adjusted. If, however, scaling was linear, the narrower opening was preferable.

This study proves temperature determination from realistically simulated ToF data with deviation lower than $5\,\%$. It also assists the previous finding that higher rotation frequency improves precision of temperature measurements. Additionally, offset from real value seems to decrease, a temperature-dependent optimal frequency might exist. Further studies and improvements of fitting routine are found to be necessary to optimally assess impact of parameters. MC simulations confirm the prediction from subsection 5.2.1 that narrower openings result in more precise temperature determination. This assumes same number of detected atoms so it requires to compromise. Put another way, statistics translates directly into accuracy. However, this is no longer efficient when size of beam is much larger than opening width and beam profile dominates transfer function.

5.2.3. Estimating accuracy for different beam temperatures

Measuring temperature has been demonstrated in the previous parameter studies for beam temperatures of $300\,\mathrm{K}$ and $2500\,\mathrm{K}$. It is initially not clear that high temperatures can be determined the same way as for room temperature, and same is true for cryogenic temperatures. ToF distributions are not simply scaled in time according to velocity of particles, this is only true for the parallel beam part $P_t^{\text{Parallel}}(t)$ and not only because of longer path of scattered particles as discussed in subsection 5.2.1. Scattering atoms of $P_t^{\text{Scattered}}(t)$ exchange energy with walls and are mostly thermalised after several hits, they then have velocity distribution according to wall temperature of $300\,\mathrm{K}$. If the incident beam is hotter, then flight time of scattered atoms is even longer in comparison. If the incident beam is colder, there is more overlap with the parallel part of ToF distribution, scattered particles can even overtake those with same incident velocity that take the shorter direct path.

It is demonstrated here, that ToF is an appropriate tool to measure temperature of atomic beams ranging from $100\,\mathrm{K}$ to $2500\,\mathrm{K}$. The framework developed in this work can extract temperature from ToF distributions in this entire range. Moreover, a single setup is suggested which can be used for hot as well as cold beams. This is a substantial feature due to the significant effort of rebuilding a vacuum system, especially when it is contaminated with tritium. Geometry of the setup is similar to those considered in the previous studies and measured temperatures T and T_{MC} are shown in Figure 5.9. The procedures that yield these two beam temperatures of different interpretation are described in subsection 5.1.4.

Maximum deviation from real temperature is within $5\,\%$ in this study. Agreement of values with each other is better than that since all values are offset to lower temperatures, as already observed before. The framework extracts temperature T about equally well in the entire considered temperature range as can be seen from the similar uncertainties. Taking statistical noise of measured ToF distribution $S(t)$ into account by MC simulations, precision of T_{MC} is seen to drop for hotter beams. If rotation frequency is low or beam temperature is high, the peak of parallel particles that indicates temperature is temporally shorter in comparison to the time T_1 between two openings. As discussed in subsection 5.2.2, such fit seems to be more prone to noise from finite statistics. Thus, for hot beams, higher number of detected atoms seems to be needed to achieve same accuracy.

Occasionally, determined temperature deviates more than estimated uncertainty suggests and not in a systematic way like generally appearing offsets. These fluctuations, such as the outliers at $300\,\mathrm{K}$ or larger uncertainty of MC simulations at $1000\,\mathrm{K}$ in Figure 5.9, are accounted to artefacts and flaws of the fitting routine. As observed in the first parameter study of subsection 5.2.2, this happens more often for such high rotation frequencies as used here. The other way around, more stability can be achieved by lowering frequency but at the price of lower accuracy. To get both, fitting routine needs to be improved to avoid occasionally occurring problems, such as ringing and noise from deconvolution or extreme values assigned to strongly correlated fit parameters. Handling weighting of the fit better might lead to more accurate description of the peak from parallel particles. This could also eliminate temperature offset of MC simulations and fix $\chi^2_{\mathrm{Reduced}}$ for simulations such as in Figure 5.8.

The setup in Figure 5.9 assumes a rotation frequency of the shutter of $f = 2000\,\mathrm{Hz}$. This is much higher than feasible in a real experiment, similar shutters can be used up to about $f = 100\,\mathrm{Hz}$. A possible set of modifications to the system to respect this threshold is doubling length L of ToF tube, using a shutter with four openings and reducing the opening angle to one fourth. This allows to lower frequency respectively to one eighth, the effect of these changes are analysed in-depth in subsection 5.2.1. Remaining reduction of rotation frequency to about half and its consequences are discussed in the previous parameter studies. These changes will mostly preserve characteristics of the setup such as the degree of frame overlap but adapting to realistic parameters will nevertheless worsen system performance. The accuracy of this version of the setup is shown in Figure A.1.

These constraints may be compensated by no longer fixing rotation frequency for all beam temperatures. This is not necessary since frequency is the only design parameter that is easily adjustable without opening the system. Potentially, this allows a differently designed setup to yield more accurate results when adapting rotation frequency to expected beam temperature. For instance, it might be advantageous to use lower frequency for colder beams to avoid high frame overlap caused by slow particles. Depending on the actual requirements of a specific experiment, the covered range of beam temperatures may also be reduced, allowing more specialised and accurate ToF setups.

5.3. Conclusion

The ToF distribution obtained from chapter 4 contains significant amounts of scattered atoms as the atomic beam is divergent. A model of the ToF distribution was presented which takes this scattering into account. The developed analysis procedure corrects the ToF distribution from distortion by the rotary shutter and determines beam temperature by fitting. Two different uncertainties are estimated: That introduced by the framework and the uncertainty found from Monte Carlo simulations mimicking real measurement data with a limited number of detected atoms.

The influence of system geometry on the accuracy of temperature determination was investigated. Recommendations on the choice of the relevant design parameters are given in the following.

- A shorter length L of the ToF setup is preferable as this reduces scattering background. However, systematic effects are expected to favour higher length but these were not considered. Also, a shorter tube requires a higher rotation frequency which is limited.
- Radius R_{Shutter} of the rotary shutter should be chosen as large as possible, this is limited by the size of the setup.
- Choice of diameter D_{S} of the skimmer is a trade-off between better accuracy by reduced scattering and lower statistics. The optimal value depends on the specific setup and can be estimated by simulations.
- Opening angle α is a trade-off between better accuracy by reduced smearing of the ToF distribution and lower statistics.

- A lower number of openings n is preferable. However, this requires a higher rotation frequency which is limited.
- Rotation frequency f is easily adjustable but mechanically limited. Its influence on accuracy is complex. At higher frequency, determined temperature seems less stable but also more precise in case of limited statistics. A temperature-dependent value of maximum trueness might exist.
- Better statistics from longer measurement time or higher particle rate is always preferable.
- No recommendations about the diameter of the ToF tube are given. Its influence depends on how particles are pumped at the end of the ToF tube and no details about this implementation are considered in the simulated setup.

It was demonstrated that the temperature of beams between $100\,\mathrm{K}$ and $2500\,\mathrm{K}$ can be measured by ToF, this is even possible with a single setup and with an accuracy of $5\,\%$. The developed framework determines temperature usually too low. When correcting for this offset, most setups achieve an accuracy well below $5\,\%$, especially when they do not need to cover a large range of beam temperatures.

Note that all simulations were conducted for protium H_2. The Maxwell-Boltzmann distribution of tritium T_2 at triple the temperature is identical to that of protium. However, results of the presented simulations can not be converted this way as room temperature stays at $300\,\mathrm{K}$. Some conclusions for especially hot and cold tritium are still possible: Requirements for T_2 at $2500\,\mathrm{K}$ are relaxed compared to H_2 as thermalisation is the same but T_2 molecules move slower. T_2 at $100\,\mathrm{K}$ at one-third of the rotation frequency is similar to a measurement of H_2 but might suffer from a more smeared ToF distribution. Strictly speaking, the applicability of ToF for tritium is thus only shown for temperatures from $300\,\mathrm{K}$ to $2500\,\mathrm{K}$ yet.

6. Conclusion and outlook

In the effort to measure the neutrino mass directly, the currently most sensitive experiment, KATRIN, will reach its limits. To meet the level of sensitivity that is given by measurements of neutrino oscillations, KATRIN's source of β-electrons needs to be upgraded to a cold atomic tritium beam. To develop the required beam cooling system, suitable diagnostics of beam temperature is essential. In this work, the application of the time-of-flight (ToF) technique for beam temperature measurements was investigated.

A framework was developed which is split in two parts: First, an experimental setup for beam temperature measurements is simulated and a ToF distribution is extracted from its ToF subsystem, imitating measurement data. Then, beam temperature and its accuracy are determined from the ToF distribution. These tools were used in conjunction with analytical models to better understand beam forming in the particle source and to find out how measurement accuracy depends on geometry. The tools can also be used to design and optimise the geometry of a ToF system for a specific setup, such as for the atomic hydrogen source at the Tritium Laboratory Karlsruhe. It was found that ToF is suited for measurements in the entire considered range of beam temperatures from $100\,\mathrm{K}$ to $2500\,\mathrm{K}$. This range can be covered by a single setup with fixed rotation frequency, though more flexible or specialised setups are preferable and achieve an accuracy better than $5\,\%$.

So far, only uncertainty from statistical fluctuations was taken into account. Determination of temperature from real measured ToF distributions introduces additional challenges: It requires beam profile and geometry of the rotary shutter to be well-known and good synchronisation between shutter and mass spectrometer is needed. Any deviation impairs temperature measurement. Simulating the impact of these deviations is already supported by the developed framework but such systematic effects were not considered yet. Further, in this work only ToF setups using a single rotary shutter were discussed. Other versions allow to slice parts of the atomic beam using a second shutter or a cylinder with a spiralled through-hole. This way, the velocity range of passing atoms is limited, potentially facilitating further improvement of accuracy.

Acknowledgements

I would like to thank Prof. Kathrin Valerius and Prof. Ralph Engel for the chance of working and writing my master's thesis at the IAP.

Special thanks to my supervisors Marco Röllig and Robin Größle who guided me through the entire project, provided me with theoretical background and practical tips and gave high-quality feedback on talks and this thesis.

I am particularly grateful for the help of Leonard Haßelmann and Caroline Rodenbeck who always took the time to explain everything I didn't understand and helped me with calculations and in the laboratory.

Many thanks to my office colleagues James Braun and Johannes Wörner for useful tips, great discussions and speculating about difficulties together. I am also grateful to Tim Sandmann for working together at the atomic hydrogen source.

Lastly, I would like to extend my thanks to all other members of the institute who provided valuable advice, helped me in the laboratory, organised helpful meetings or interesting guided tours. I enjoyed the pleasant atmosphere at the Tritium Laboratory and all chances of visiting experiments at Campus North and elsewhere.

Bibliography

[AAB05] J. Angrik, T. Armbrust, and A. Beglarian. *KATRIN design report 2004*. 2005.

[Ake+22] M. Aker et al. “Direct neutrino-mass measurement with sub-electronvolt sensitivity”. In: *Nature Physics* 18.2 (Feb. 2022). DOI: 10.1038/s41567-021-01463-1.

[Ala+21] Shadab Alam et al. “Completed SDSS-IV extended Baryon Oscillation Spectroscopic Survey: Cosmological implications from two decades of spectroscopic surveys at the Apache Point Observatory”. In: *Physical Review D* 103.8 (Apr. 28, 2021). DOI: 10.1103/PhysRevD.103.083533.

[AM86] S Adamson and J. F. McGilp. “Measurement of gas flux distributions from single capillaries using a modified, uhv-compatible ion gauge, and comparison with theory”. In: *Vacuum* 36.4 (Apr. 1, 1986). DOI: 10.1016/0042-207X(86)90005-9.

[Aue+77] D. Auerbach et al. “Energy accommodation and reactivity of O2 on tungsten”. In: *Applied physics* 14.2 (Oct. 1, 1977). DOI: 10.1007/BF00883081.

[Bag07] V. Baglin. “Cold/sticky systems”. In: *CAS - CERN Accelerator School: Vacuum in Accelerators. Platja d’Aro, Spain 16 - 24 May 2006.* Ed. by Daniel Brandt. Geneva: CERN, 2007.

[BB93] U. Bischler and E. Bertel. “Simple source of atomic hydrogen for ultrahigh vacuum applications”. In: *Journal of Vacuum Science & Technology A* 11.2 (Mar. 1993). DOI: 10.1116/1.578754.

[Ben99] Cristoforo Benvenuti. “Molecular surface pumping: the getter pumps”. In: *CAS - CERN Accelerator School: Vacuum Technology. Snekersten, Denmark 28 May - 3 Jun 1999.* Ed. by Stuart Turner. Geneva: CERN, 1999.

[Chr88] K. Christmann. “Interaction of hydrogen with solid surfaces”. In: *Surface Science Reports* 9.1 (July 1, 1988). DOI: 10.1016/0167-5729(88)90009-X.

[Cla30] P. Clausing. “Über die Strahlformung bei der Molekularströmung”. In: *Zeitschrift für Physik* 66.7 (July 1, 1930). DOI: 10.1007/BF01402029.

[Cla32] P. Clausing. “Über die Strömung sehr verdünnter Gase durch Röhren von beliebiger Länge”. In: *Annalen der Physik* 404.8 (1932). DOI: 10.1002/andp.19324040804.

[col+21] The KATRIN collaboration et al. “The design, construction, and commissioning of the KATRIN experiment”. In: *Journal of Instrumentation* 16.8 (Aug. 2021). DOI: 10.1088/1748-0221/16/08/T08015.

[Col+22] Project 8 Collaboration et al. *The Project 8 Neutrino Mass Experiment*. Mar. 14, 2022. DOI: 10.48550/arXiv.2203.07349.

[Coo+20] S. F. Cooper et al. “Cryogenic atomic hydrogen beam apparatus with velocity characterization”. In: *Review of Scientific Instruments* 91.1 (Jan. 1, 2020). DOI: 10.1063/1.5129156.

[Cow+56] C. L. Cowan et al. “Detection of the Free Neutrino: a Confirmation”. In: *Science* 124.3212 (July 20, 1956). DOI: 10.1126/science.124.3212.103.

[Day58] B. B. Dayton. “Strömungsbilder von Gasen am Ein- und Ausgang zylindrischer Rohre”. In: *Vakuum-Technik* 7 (1958).

[DP18] Alessandro De Angelis and Mário Pimenta. *Introduction to Particle and Astroparticle Physics*. Undergraduate Lecture Notes in Physics. Cham: Springer International Publishing, 2018. DOI: 10.1007/978-3-319-78181-5.

[ELW98] C. Eibl, G. Lackner, and A. Winkler. “Quantitative characterization of a highly effective atomic hydrogen doser”. In: *Journal of Vacuum Science & Technology A: Vacuum, Surfaces, and Films* 16.5 (Sept. 1998). DOI: 10.1116/1.581449.

[FGR21] Joseph A. Formaggio, André Luiz C. de Gouvêa, and R. G. Hamish Robertson. “Direct measurements of neutrino mass”. In: *Physics Reports*. Direct measurements of neutrino mass 914 (June 3, 2021). DOI: 10.1016/j.physrep.2021.02.002.

[FY04] R. Feres and G. Yablonsky. “Knudsen’s cosine law and random billiards”. In: *Chemical Engineering Science* 59.7 (Apr. 1, 2004). DOI: 10.1016/j.ces.2004.01.016.

[GWE09] Rafael C. Gonzalez, Richard E. Woods, and Steven L. Eddins. *Digital image processing using MATLAB®*. 2. ed. s.l.: Gatesmark Publishing, 2009. 826 pp.

[Han60] G. R. Hanes. “Multiple Tube Collimator for Gas Beams”. In: *Journal of Applied Physics* 31.12 (Dec. 1, 1960). DOI: 10.1063/1.1735519.

[Hel67] John C. Helmer. “Applications of an Approximation to Molecular Flow in Cylindrical Tubes”. In: *Journal of Vacuum Science and Technology* 4.4 (July 1, 1967). DOI: 10.1116/1.1492543.

[Jou18] Karl Jousten, ed. *Handbuch Vakuumtechnik*. 12th ed. Springer Reference Technik. Wiesbaden: Springer Fachmedien Wiesbaden, 2018. DOI: 10.1007/978-3-658-13386-3.

[KA19] Roberto Kersevan and Marton Ady. “Recent Developments of Monte-Carlo Codes Molflow+ and Synrad+”. In: *Proceedings of the 10th Int. Particle Accelerator Conf.* IPAC2019 (2019). In collab. with Boland Mark (Ed.) et al. DOI: 10.18429/JACoW-IPAC2019-TUPMP037.

[Kam+16] KamLAND-Zen Collaboration et al. “Search for Majorana Neutrinos Near the Inverted Mass Hierarchy Region with KamLAND-Zen”. In: *Physical Review Letters* 117.8 (Aug. 16, 2016). DOI: 10.1103/PhysRevLett.117.082503.

[Kle+19] M. Kleesiek et al. “β-Decay spectrum, response function and statistical model for neutrino mass measurements with the KATRIN experiment”. In: *The European Physical Journal C* 79.3 (Mar. 7, 2019). DOI: 10.1140/epjc/s10052-019-6686-7.

[Knu16] Martin Knudsen. “Das Cosinusgesetz in der kinetischen Gastheorie”. In: *Annalen der Physik* 353.24 (Jan. 1, 1916). DOI: 10.1002/andp.19163532409.

[KY11] V. L. Kovalev and A. N. Yakunchikov. “Accommodation Coefficients for Hydrogen Molecules on Graphite Surface”. In: *AIP Conference Proceedings* 1333.1 (May 20, 2011). DOI: 10.1063/1.3562694.

[Lan57] L. Landau. “On the conservation laws for weak interactions”. In: *Nuclear Physics* 3.1 (Mar. 1, 1957). DOI: 10.1016/0029-5582(57)90061-5.

[Ler+97] Olivier Leroy et al. “Thermal accommodation of a gas on a surface and heat transfer in CVD and PECVD experiments”. In: *Journal of Physics D: Applied Physics* 30.4 (Feb. 1997). DOI: 10.1088/0022-3727/30/4/001.

[OK70] Donald R. Olander and Valerie Kruger. “Molecular Beam Sources Fabricated from Multichannel Arrays. III. The Exit Density Problem”. In: *Journal of Applied Physics* 41.7 (June 1970). DOI: 10.1063/1.1659313.

[OW08] E. W. Otten and C. Weinheimer. “Neutrino mass limit from tritium β-decay”. In: *Reports on Progress in Physics* 71.8 (July 2008). DOI: 10.1088/0034-4885/71/8/086201.

[Par+22] Particle Data Group et al. “Review of Particle Physics”. In: *Progress of Theoretical and Experimental Physics* 2022.8 (Aug. 8, 2022). DOI: 10.1093/ptep/ptac097.

[Pau30] Wolfgang Pauli. *Offener Brief an die Gruppe der Radioaktiven*. Dec. 4, 1930.

[Pet13] S. T. Petcov. “The Nature of Massive Neutrinos”. In: *Advances in High Energy Physics* 2013 (Apr. 14, 2013). DOI: 10.1155/2013/852987.

[QWW23] JianHao Qian, HengAn Wu, and FengChao Wang. “A generalized Knudsen theory for gas transport with specular and diffuse reflections”. In: *Nature Communications* 14.1 (Nov. 15, 2023). DOI: 10.1038/s41467-023-43104-6.

[SNO+02] SNO Collaboration et al. “Direct Evidence for Neutrino Flavor Transformation from Neutral-Current Interactions in the Sudbury Neutrino Observatory”. In: *Physical Review Letters* 89.1 (June 13, 2002). DOI: 10.1103/PhysRevLett.89.011301.

[Sou86] P. C. Souers. *Hydrogen properties for fusion energy*. Berkeley: University of California Press, 1986. 391 pp.

[Sup+98] Super-Kamiokande Collaboration et al. “Evidence for Oscillation of Atmospheric Neutrinos”. In: *Physical Review Letters* 81.8 (Aug. 24, 1998). DOI: 10.1103/PhysRevLett.81.1562.

[TB98] K. G. Tschersich and V. von Bonin. “Formation of an atomic hydrogen beam by a hot capillary”. In: *Journal of Applied Physics* 84.8 (Oct. 15, 1998). DOI: 10.1063/1.368619.

[TFS08] K. G. Tschersich, J. P. Fleischhauer, and H. Schuler. “Design and characterization of a thermal hydrogen atom source”. In: *Journal of Applied Physics* 104.3 (Aug. 2008). DOI: 10.1063/1.2963956.

[TM19] Paul A. Tipler and Gene Mosca. *Physik: für Studierende der Naturwissenschaften und Technik*. Ed. by Peter Kersten and Jenny Wagner. Berlin, Heidelberg: Springer, 2019. DOI: 10.1007/978-3-662-58281-7.

[Tsc00] K. G. Tschersich. “Intensity of a source of atomic hydrogen based on a hot capillary”. In: *Journal of Applied Physics* 87.5 (Mar. 2000). DOI: 10.1063/1.372220.

A. Appendix

A.1. Accuracy of determined temperature for different beam temperatures at lower rotation frequency

Figure A.1 is a version of the setup presented in Figure 5.9. It is adapted as suggested in subsection 5.2.3 to reduce rotation frequency from $f = 2000\,\mathrm{Hz}$ to a feasible value of $100\,\mathrm{Hz}$, so ToF length is doubled to $L = 1\,\mathrm{m}$, the number of openings is increased from 1 to 4 and their opening angles are respectively reduced from $\alpha = 21°$ to $5.25°$. The accuracy of the determined temperatures is lower but still well below $10\,\%$, for most temperatures within $5\,\%$.

A.2. Parameters of the framework

A list of parameters used in the developed framework is given in Table A.1. In addition, the generated ToF distribution and the determined temperature depend on the following factors, which are not all explicit parameters. Different parameters can be assigned for the deconvolution of the transfer function $h(t)$ from the measured ToF distribution $S(t)$ to test the impact of not exactly known geometry of the shutter $w(t)$ or beam $b_x(x)$.

- Molflow simulation of the capillary
  - $l_{\mathrm{eff}} = 8$
  - Resolution of the segmented capillary
- Molflow simulation of the skimmer setup
  - Diameter D_{S} of the opening of the second skimmer
  - Sticking factor or pumping speed of the TMPs and particle mass of $2\,\mathrm{g\,mol^{-1}}$
  - Resolution of the segmented detector
  - Entire CAD design

Table A.1.: **Parameters of the framework** Values are given for the setup in Figure 5.9.

Category	Parameter	Value	Comment
Molflow	Beam temperature	100 ... 2500	in K
simulation	Wall temperature	300	in K
of ToF pipe	accommodation coefficient	0.09	
	Particle mass	1	in u
	Length of pipe	0.5	in m, also an explicit parameter
	Diameter of pipe	0.1	in m
Rotary shutter	rotation_freq	2000	in Hz
	R_shutter	0.1	in m
	opening_angle	21	in °
	R_beam	0.077	in m
	openings	1	Number of openings
	profile	(filepath)	Circle or profile
	profile_integral	0	Can normalise profile
	delay	't0'	Delay of transfer function
	delay_Rfactor	1	Multiplier of delay
Rotary shutter	R_shutter_deconv	'same'	
(deconvolution)	opening_angle_deconv	'same'	
	R_beam_deconv	'same'	
	openings_deconv	'same'	
	profile_deconv	'same'	
	profile_integral_deconv	'same'	
	delay_deconv	'same'	
	delay_Rfactor_deconv	'same'	
Statistics	iteration_length	1e6	Splits data into batches
	res	6000	Spline resolution
	tmax	0.002	in s, simulated time span
	number_bins	500	Resolution of ToF distribution
Noise and	noise_sigma	0	Noise in absolute values
background	noise_relToMax	False	Noise in relative values
	noise_type	'gauss'	
	bg_value	0	Constant background (abs.)
	bg_relToMax	False	Constant background (rel.)
Analysis	fitmodel	'expDelay'	Explained in subsection 5.1.2
	filtering	0.1	Smoothing before fit
	wiener_noise	1e-3	Setting for Wiener deconvolution
	shift_bins	True	Correction for histogram fit
	spline_method	'PCHIP'	See subsection 4.3.2
	cutleft	0.01	Lower temporal limit of fit
	cutright	0.95	Upper temporal limit of fit
Monte-Carlo	MC_wiener_noise	0.1	
	MC_wiener_noise_idealised	1e-3	No added fluctuations
	MC_filter_after_noise	0.04	Smoothing for idealising data
	MC_assumed_particles	1e8	Assumed MC number of particles
	MC_iterations	1000	Number of MC iterations
	MC_filtering_for_err	0.01	Uncertainty estimated from this

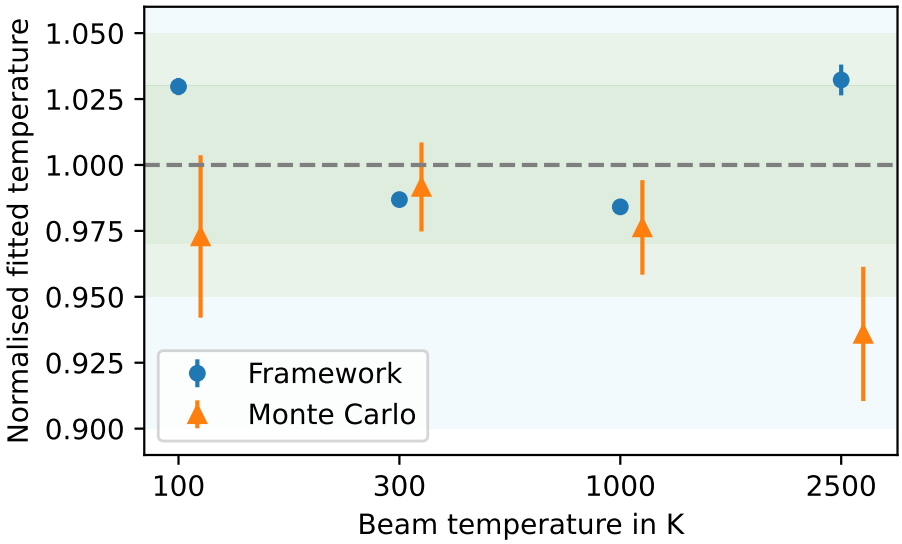

Figure A.1.: **Accuracy of determined temperature for different beam temperatures at lower rotation frequency** This is a version of the setup presented in Figure 5.9 with lower rotation frequency.